Université de Montréal

CARACTÉRISATION SPATIO- TEMPORELLE DE PLASMAS INDUITS PAR LASER POUR DES APPLICATIONS À LA CHIMIE ANALYTIQUE ET AU DÉPÔT DE COUCHES MINCES

par
Mahmoud Dawood

Département de physique
Faculté des arts et des sciences

Thèse présentée à la Faculté des études supérieures
en vue de l'obtention du grade de

Philosophiæ Doctor (Ph.D.)
en physique

Décembre 2014

© Mahmoud Dawood, 2014

Université de Montréal

SPACE AND TIME CHARACTERIZATION OF LASER-INDUCED PLASMAS FOR APPLICATIONS IN CHEMICAL ANALYSIS AND THIN FILM DEPOSITION

by

Mahmoud Dawood

Department of physics

Faculty of Arts and Science

A dissertation presented to the Faculty of Graduate Studies

in partial fulfillment of the requirements for the degree of

Doctor of philosophy (ph.D.)

in Physics

December 2014

© Mahmoud Dawood, 2014

Université de Montréal
Faculté des Études Supérieures

Cette thèse intitulée:

CARACTÉRISATION SPATIO- TEMPORELLE DE PLASMAS INDUITS PAR LASER POUR DES APPLICATIONS À LA CHIMIE ANALYTIQUE ET AU DÉPÔT DE COUCHES MINCES

Présentée par :
Mahmoud Dawood

a été évaluée par le jury composé des personnes suivantes :

Prof. Luc Stafford	President du jury
Prof. Joëlle Margot	Directrice de recherche
Prof. Michael Wertheimer	Member du jury
Prof. Steven Rehse	Examinateur externe
Prof. Yvan Saint-Aubin	Représentant du doyen

Thése acceptée le : 8 mai 2015

RÉSUMÉ

Après des décennies de développement, l'ablation laser est devenue une technique importante pour un grand nombre d'applications telles que le dépôt de couches minces, la synthèse de nanoparticules, le micro-usinage, l'analyse chimique, etc. Des études expérimentales ainsi que théoriques ont été menées pour comprendre les mécanismes physiques fondamentaux mis en jeu pendant l'ablation et pour déterminer l'effet de la longueur d'onde, de la durée d'impulsion, de la nature de gaz ambiant et du matériau de la cible.

La présente thèse décrit et examine l'importance relative des mécanismes physiques qui influencent les caractéristiques des plasmas d'aluminium induits par laser. Le cadre général de cette recherche forme une étude approfondie de l'interaction entre la dynamique de la plume-plasma et l'atmosphère gazeuse dans laquelle elle se développe. Ceci a été réalisé par imagerie résolue temporellement et spatialement de la plume du plasma en termes d'intensité spectrale, de densité électronique et de température d'excitation dans différentes atmosphères de gaz inertes tel que l'Ar et l'He et réactifs tel que le N_2 et ce à des pressions s'étendant de 10^{-7} Torr (vide) jusqu'à 760 Torr (pression atmosphérique).

Nos résultats montrent que l'intensité d'émission de plasma dépend généralement de la nature de gaz et qu'elle est fortement affectée par sa pression. En outre, pour un délai temporel donné par rapport à l'impulsion laser, la densité électronique ainsi que la température augmentent avec la pression de gaz, ce qui peut être attribué au confinement inertiel du plasma. De plus, on observe que la densité électronique est maximale à proximité de la surface de la cible où le laser est focalisé et qu'elle diminue en s'éloignant (axialement et radialement) de cette position. Malgré la variation axiale importante de la température le long du plasma, on trouve que sa variation radiale est négligeable. La densité électronique et la température ont été trouvées maximales lorsque le gaz est de l'argon et minimales pour l'hélium, tandis que les valeurs sont intermédiaires dans le cas de l'azote. Ceci tient surtout aux propriétés physiques et chimiques du gaz telles que la masse des espèces, leur énergie d'excitation et d'ionisation, la conductivité thermique et la réactivité chimique.

L'expansion de la plume du plasma a été étudiée par imagerie résolue spatio-temporellement. Les résultats montrent que la nature de gaz n'affecte pas la dynamique de la plume pour des pressions inférieures à 20 Torr et pour un délai temporel inférieur à 200 ns. Cependant, pour des pressions supérieures à 20 Torr, l'effet de la nature du gaz devient important et la plume la plus courte est obtenue lorsque la masse des espèces du gaz est élevée et lorsque sa conductivité thermique est relativement faible. Ces résultats sont confirmés par la mesure de temps de vol de l'ion Al^+ émettant à 281,6 nm. D'autre part, on trouve que la vitesse de propagation des ions d'aluminium est bien définie juste après l'ablation et près de la surface de la cible. Toutefois, pour un délai temporel important, les ions, en traversant la plume, se thermalisent grâce aux collisions avec les espèces du plasma et du gaz.

Mots-clés: plasmas induits par laser, ablation de l'aluminium, dynamique de la plume du plasma, ablation dans différentes atmosphères gazeuses, spectroscopie d'émission optique, temps de vol, densité électronique, température d'excitation, diagramme de Boltzmann.

ABSTRACT

After decades of development, laser ablation has become an important technique for a large number of applications such as thin film deposition, nanoparticle synthesis, micromachining, chemical analysis, etc. Experimental and theoretical studies have been conducted to understand the physical mechanisms of the laser ablation processes and their dependence on the laser wavelength, pulse duration, ambient gas and target material.

The present dissertation describes and investigates the relative importance of the physical mechanisms influencing the characteristics of aluminum laser-induced plasmas. The general scope of this research encompasses a thorough study of the interplay between the plasma plume dynamics and the ambient gas in which they expand. This is achieved by imaging and analyzing the temporal and spatial evolution the plume in terms of spectral intensity, electron density and excitation temperature within various environments extending from vacuum (10^{-7} Torr) to atmospheric pressure (760 Torr), in an inert gas like Ar and He, as well as in a chemically active gas like N_2.

Our results show that the plasma emission intensity generally differs with the nature of the ambient gas and it is strongly affected by its pressure. In addition, for a given time delay after the laser pulse, both electron density and plasma temperature increase with the ambient gas pressure, which is attributed to plasma confinement. Moreover, the highest electron density is observed close to the target surface, where the laser is focused and it decreases by moving away (radially and axially) from this position. In contrast with the significant axial variation of plasma temperature, there is no large variation in the radial direction. Furthermore, argon was found to produce the highest plasma density and temperature, and helium the lowest, while nitrogen yields intermediate values. This is mainly due to their physical and chemical properties such as the mass, the excitation and ionization levels, the thermal conductivity and the chemical reactivity.

The expansion of the plasma plume is studied by time- and space-resolved imaging. The results show that the ambient gas does not appreciably affect plume dynamics as long as the gas pressure remains below 20 Torr and the time delay below 200 ns. However, for pressures higher than 20 Torr, the effect of the ambient gas becomes important and the shorter plasma plume length corresponds to the highest gas mass species and the lowest thermal conductivity. These results are confirmed by Time-Of-Flight (TOF) measurements of Al^+ line emitted at 281.6 nm. Moreover, the velocity of aluminum ions is well defined at the earliest time and close to the target surface. However, at later times, the ions travel through the plume and become thermalized through collisions with plasma species and with surrounding ambient gas.

Key words: laser-induced plasmas, ablation of aluminum, plasma plume dynamics, ablation in different ambient gas, optical emission spectroscopy, time of flight, electron density, excitation temperature, Boltzmann plot.

TABLE OF CONTENTS

LIST OF FIGURES

CHAPTER 1

CHAPTER 2

CHAPTER 3

CHAPTER 4

CHAPTER 5

APPENDIX

LIST OF TABLES

ACKNOWLEDGMENTS

First and foremost, I would like to express my deepest gratitude to my research adviser, Professor Dr. Joëlle Margot for all the continuous support, scientific guidance and advice she has given me all these years. Her vast knowledge, calm nature and positive criticism motivated me to finish this research. Indeed, I appreciate all her contributions of time, ideas, and funding to make my Ph.D. experience productive and stimulating.

All my gratitude is also going to the members of the Jury committee for having accepted to evaluate this research work:

- I would like to express my sincere thanks to Assoc. Prof. Dr. Luc Stafford, of the Physique des Plasmas group at University of Montréal, for having accepted to preside over the jury committee.
- I would like to express my special thanks to Prof. Dr. Michael Wertheimer, of the Department of Engineering Physics at Ecole Polytechnique Montréal, for having accepted to review this work and for being part of the jury committee.
- I would like to express my deep thanks to Assoc. Prof. Dr. Steven Rehse, of the Department of Physics at the University of Windsor for having accepted to examine this work and for being part of the jury committee.

I am indebted to all the previous and current members of the physics department at the University of Montreal for providing me the opportunity to perform my research in a remarkable human and scientific environment. In particular, special and remarkable thanks to

the Physique des Plasmas group at University of Montréal. I consider myself very fortunate and I am incredibly proud to have been a part of this amazing group.

I thank Mr. Richard Piché and Dr. Danielle Kéroack for their kind help and assistance in purchasing equipment needed for the research and setting up the initial stages of the experiment.

Exceptional thanks to Dr. Ahmad Hamdan, who as a good friend was always willing to help and give his best suggestions and contribution in writing the articles.

Lastly, but most importantly, I would like to extend my sincerest gratitude and appreciation to all members of my family and friends for their unwavering support and encouragement during my entire life.

To my parents, my wife and my lovely kids
Aesha & Maryam for their endless love,
support and encouragement.

INTRODUCTION

Introduction

In recent years, there has been a growing interest in characterizing plasmas produced by laser-matter interaction. This stems from the need for developing and improving several applications of laser-induced plasma. This includes elemental analysis by laser-induced breakdown spectroscopy (LIBS) performed at atmospheric pressure [1, 2], as well as thin film [3] and nanoparticles and cluster synthesis by pulsed-laser deposition (PLD) in background gas with residual or low pressure [4], in addition to materials machining (welding and cutting) [5], or even for propulsion technology when the target used is adapted for this purpose [6]. The wealth of the physical phenomena allows the development of hybrid laser-based techniques. For instance, the ablation of a solid target immersed in a liquid medium was used for the synthesis of new materials. Indeed, the ablated species are highly confined to a small region in the vicinity of the solid-liquid interface due to the inertia of liquid [7, 8]. It is expected that this region will have an instantaneous high density of energetic species, high pressure and high temperature, forming a suitable medium for the growth of some crystallographic phases [9]. Actually, it has been reported that small crystallites of diamond are formed by the irradiation of a solid target immersed in water [10] or in organic liquids [11]. This has led to significant research progress in the characterization of laser-produced plasma to obtain exhaustive information on the different physical processes governing these plasmas.

In laser-induced plasmas, an intense laser beam with an irradiance exceeding a certain threshold value, typically in the order of 10^8 W/cm^2, is focused on the surface of a target which, during or by the end of the pulse, may dissociate, excite, and/or ionize the constituent atomic species of the solid and produce the plasma.

As reported by Raizer [12], when a pulsed laser beam is directed to a small spatial region of target atoms, the laser-material interaction begins, producing a very rapid temperature rise at the focal spot. This produces breakdown in the region of the focal spot of the target atoms and results in the ionization of the atoms. Subsequently, the plasma becomes absorbing at the laser beam wavelength after a certain delay, and it expands out of the focal volume due to the drastic increase of the plasma density in a very short period of time. This extremely high density of plasma energy sustains the plasma plume for a relatively long time after the end of the laser pulse.

The expansion of the plasma begins to slow down via collisions with the ambient gas species or within the plasma plume. Then, electrons and ions recombine, forming a large population of neutral atoms, and the plasma continues to cool down. Depending on the pressure, mass density and thermal conductivity of the ambient gas, the plasma lifetime may vary from a few hundreds of ns to a few tens of μs.

It is worth mentioning that the plasma plume characteristics are extremely dependent on the laser beam parameters such as wavelength, intensity, pulse duration and irradiation spot size, as well as the ambient pressure and gas composition. In particular, the interaction of the plume plasma with an ambient gas is a far more complex gas dynamic process (in contrast with the situation in vacuum, where there is a free expansion), attributed to the occurrence of several physical processes, such as deceleration, attenuation, thermalization of the ablated

species, diffusion, recombination, formation of shock waves, and clustering [13]. Moreover, the physical, chemical and mechanical properties of the target material also play an important role in laser ablation [14, 15, and 16].

The plasma emission spectrum is basically a fingerprint of the plasma's physical state and it can be used to determine several characteristics, including the number densities and temperatures of the different plasma species (i.e. ions, electrons and neutral atoms). Among the aforementioned characteristics, the magnitude and the temporal evolution of both the temperature T_e and the electron density n_e are two major properties to be investigated and optimized by carefully choosing suitable diagnostic techniques. The most useful technique is emission spectroscopy, which can provide, in-situ, spatially and temporally precise measurements of plasma species characteristics. Moreover, emission spectroscopy is non-intrusive and it is also often flexible, while enabling investigation of high temperature or high/low pressure systems.

Objectives of the thesis

In literature, there are contradictory published results. On the one hand, Freeman *et al.* [17] have shown that the ablation of a brass (70% copper and 30% zinc) target in vacuum and in air (at atmospheric pressure) leads to plasma with high n_e and T_e when the experiments were performed at atmospheric pressure. The variation as a function of pressure has an identical trend, whatever the laser pulse duration, 8 ns (at 1064 nm) or 40 fs (at 800 nm). Moreover, several experimental studies [18 - 21] have shown that generating laser plasmas in an argon atmosphere yields higher emission intensity as compared to other gases like He, N_2 and air. This can be understood by a higher plasma confinement in Ar due to its higher mass density,

lower ionization energy, and more efficient heating by inverse Bremsstrahlung. On the other hand, Bashir *et al.* [22] used a 10 ns pulsed laser at 1064 nm to ablate a cadmium target in argon, air and helium background gases at pressure in the ranges of 5-760 Torr. They found that the T_e as well as the n_e decreases with increasing gas pressure. Farid *et al.* [23] used the same laser characteristic as Bashir *et al.* (10 ns at 1064 nm) to ablate a copper target also in the same environments of argon, air and helium in pressure ranges of 5-760 Torr. The authors found that the T_e increases with rising pressure, reaching a maximum at ~100 Torr, and decreases to reach an identical value (that obtained at low pressure) at 760 Torr. The same variation was also observed in the n_e, but it was more pronounced in argon gas compared to air and helium. Furthermore, other research groups [24-26] confirmed that for each ambient gas there existed an optimum pressure range at which the emission intensity and the plasma parameters were maximized. They attributed these results to the interaction between the plasma plume and the ambient gas. It has been also reported that at high pressures, instabilities can appear at the plasma-gas interface, especially Rayleigh-Taylor (RT) instability (RT instability occurs when there are two fluids of different densities adjacent to each other and the lighter fluid is accelerated towards the denser fluid) [13, 27]. The physical processes occurring at this interface, again, were very complex and far from being completely understood at this date.

It can therefore be concluded from these various observations and comparisons of the contradictory published results, that the physics occurring during ablation is not only complicated, but also very sensitive to the experimental conditions. They indicate that there is no clear consensus on how laser-induced plasmas are influenced by their environment.

In this context, the primary objective of the present work is to conduct a thorough study of the interplay between the ablated plasma plume and the ambient gas. We present a deep study of analyzing the temporal and spatial evolution of an aluminum plasma in terms of spectral intensity, n_e and T_e within various environments, extending from vacuum (10^{-7} Torr) to atmospheric pressure (760 Torr), while using an inert gas like Ar and He, as well as a chemically active gas, N_2. Moreover, we present in detail the effect of the background gas composition on the plasma plume dynamics. Al was chosen as a typical target, on one hand, for which a remarkable amount of spectral characteristics and atomic data are known, which facilitates the interpretation of emission spectra from a wide variety of analytical techniques. On the other hand, Al is used in the applications of laser propulsion, where the plasma produced from an Al target is found to have a significant potential to be used as explosives and propellants. In addition, Al is used as an explosive to augment air blast, raise reaction temperatures, and create incendiary effects [28]. Moreover, Al is found to be a promising metal in the field of nanotechnology; in particular in nanoparticle synthesis for biomedical applications [29-31].

Finally, our experimental results are compared to previous studies in order to provide a comprehensive study of the correlation between the surrounding ambient conditions and the plasma plume dynamics.

This thesis is organized as follows: Chapter 1 contains a review of laser-matter interaction and the steps leading to plasma formation. Then, the temporal and spatial evolution of laser-induced plasma will be reviewed, followed by a description of various methods used for determining plasma n_e and T_e. A brief review of recent experimental works on laser-induced plasma is also presented.

Chapter 2 is devoted to a detailed description of the experimental setup and of the data acquisition system. In addition, we present several parameters that were optimized and calibrated to enhance the accuracy and precision of the collected data for both temporal and spatial evolution. At the end of the chapter, the methods used to determine the n_e and T_e are described.

Chapter 3 provides a comprehensive analysis of the temporal evolution of an Al plasma in terms of spectral intensity, n_e and T_e within various environments, extending from vacuum to atmosphere, and using different ambient gases like Ar, N_2 and He. Our experimental results are compared to those available in the literature to establish some correlation between the surrounding ambient conditions and the plasma plume dynamics.

Chapter 4 presents the axial and radial spatial distribution of different plasma parameters as a function of time after the laser shot. Moreover, the effect of ambient gas pressure and composition is examined and compared to previous studies. Finally, the plasma expansion geometry is examined to provide a comprehensive understanding of the whole plasma evolution.

In chapter 5 we present an exhaustive study of the plasma plume dynamics under the effect of the ambient gas composition and pressure. Space- and time- resolved emission spectroscopic studies for Al ions at 281.6 nm were used to determine the Time-Of-Flight profiles (TOF). The effect of the ambient gases on the TOF profiles and therefore on the propagation velocity of Al ions is discussed. Furthermore, a correlation between the plasma plume expansion velocities, deduced from iCCD images and TOF profiles, is presented.

Finally, brief interpretations of the main results will be presented in the conclusion section. A few perspectives for future works will also be discussed.

References

[01] B. Sallé, D.A. Cremers, S. Maurice, R.C. Wiens and P. Fichet, Spectrochim. Acta B, 60(6), 805–815, 2005.

[02] J.L. Gottfried, F.C. De Lucia Jr, C.A. Munson and A.W. Miziolek, Anal. Bioanal. Chem., 395(2), 283–300, 2009.

[03] D.B. Chrisey and G.K. Hubler, Pulsed Laser Deposition of Thin Films, pp. 648. ISBN 0-471-59218-8. Wiley-VCH, 2003.

[04] R.S. Lee, H.J. Kim, J.E. Fischer, A. Thess, and R.E. Smalley, Nature, 388(6639), 255–257, 1997.

[05] Z. Szymanski, J. Kurzyna and W. Kalita, J. Phys. D Appl. Phys., 30(22), 3153, 1997.

[06] S. Yuasa, Y. Zhu and S. Sogo, Combust. Flame, 108, 387, 1997.

[07] L. Berthe, R. Fabbro, P. Peyre, L. Tollier and E. Bartnicki, J. Appl. Phys. 82, 2826, 1997.

[08] S. Zhu, Y.F. Lu, M.H. Hong and X.Y. Chen, J. Appl. Phys., 89, 2400, 2001.

[09] K. Saito, T. Sakka and Y.H. Ogata, J. Appl. Phys., 94(9), 5530–5536, 2003.

[10] J.B. Wang and G.W. Yang, Journal of Physics: Condensed Matter, 11(37), 7089, 1999.

[11] Y.F. Lu, S.M. Huang, X.B. Wang and Z.X. Shen, Appl. Phys. A Mater. Sci., 66(5), 543–547, 1998.

[12] Y.P Raizer, Gas Discharge Physics., (Berlin: Springer- Verlag), 1991.

[13] S.S. Harilal, C.V. Bindhu, M.S. Tillack, F. Najmabadi and A.C. Gaeris, J. Appl. Phys., 93(5), 2380–2388, 2003.

[14] L.J. Radziemski, T.R. Loree, D.A. Cremers, N.M. Hoffman, Anal. Chem., 55, 1246–1252, 1983.

[15] K.J. Grant, G.L. Paul, Appl. Spectrosc., 44, 1349–1354, 1990.

[16] J.B. Simeonsson, A.W. Miziolek, Appl. Opt., 32, 939–947, 1993.

[17] J.R. Freeman, S.S. Harilal, P.K. Diwakar, B. Verhoff and A. Hassanein, Spectrochim. Acta B, 87, 43–50, 2013.

[18] Y. Lee, K. Song, and J. Sneddon, "Laser induced plasmas for analytical atomic spectroscopy" ch. 5 in Lasers Analytical Atomic Spectroscopy, J. Sneddon et al. (Eds.), New York: VCH, 197–235, 1997.

[19] W. Sdorra and K. Niemax, Mikrochim. Acta, 107, 319, 1992.

[20] X. L. Mao, W. T. Chan, M. A. Shannon, and R. E. Russo, J. Appl. Phys., 74, 4915, 1993.

[21] H. Lindnera, K. H. Loperb, D. W. Hahnb and K. Niemax, Spectrochim. Acta B, 66, 179, 2011.

[22] S. Bashir, N. Farid, K. Mahmood and M.S. Rafique, Appl. Phys. A Mater. Sci., 107(1), 203–212, 2012.

[23] N. Farid, S. Bashir and K. Mahmood, Physica Scripta, 85(1), 015702, 2012.

[24] Y. Iida, Spectrochim. Acta B, 45, 1353, 1990.

[25] G. Asimellis, S. Hamilton, A. Giannoudakos, and M. Kompitsas, Spectrochim. Acta B, 60, 1132, 2005.

[26] A. K. Knight, N. L. Scharbarth, D. A. Cremers, and M. J. Ferris, Appl. Spectrosc., 54, 331, 2000.

[27] A.K. Sharma and R.K. Thareja, Appl. Surf. Sci., 243(1), 68–75, 2005.

[28] S. Yuasa, Y. Zhu and S. Sogo, Combust. Flame 108, 387, 1997.

[29] LG Gutwein, TJ Webster, *American Ceramic Society 26 th Annual Meeting Conference Proceedings,* 2003, in press.

[30] M. H. Chowdhury, K.Ray, S. K. Gray, J. Pond, & J. R. Lakowicz, Anal. Chem.,81(4), 1397-1403, 2009.

[31] I. M. Sadiq, B. Chowdhury, N. Chandrasekaran, & A. Mukherjee, Nanotechnology, Biology and Medicine, 5(3), 282-286, 2009.

CHAPTER 1:

Theoretical background

Chapter 1:
Theoretical Background

1.1 Introduction

Understanding the processes, which occur in laser-matter interaction, is the key to control and improve the laser-induced plasma properties in view of their applications. The process of removing material from a solid surface by focusing a short-pulse laser beam (~10^8 W/cm^2) on a small volume of the target is known as laser ablation. Such interaction results in melting and evaporation of this focal volume, which will further interact with the laser beam to form a highly energetic plasma plume that consists of free electrons, excited atoms and ions. Wen *et al*. [1] pointed out that the rate of vaporization of the material is mainly dependent on the ambient gas pressure and not on the composition of the gas. Chan and Russo [2] showed that the ablation process is stoichiometric in this regime, owing to the more uniform non-thermal heating and the more explosive release of the ejected material. This suggests that the composition of the plasma plume is representative of the composition of the target material. Moreover, the produced plasma plume characteristics are extremely dependent on the laser beam parameters such as wavelength, intensity and pulse duration, irradiation spot size as well as on ambient pressure and gas composition. In addition, the physical, chemical and mechanical properties of the target material also play an important role in laser-induced ablation [3-5].

Many analyses and experiments have been conducted since the 1960's in order to understand the physical mechanisms, the dynamics and the important factors that affect the plasma generated by laser ablation [6-9]. Herein and after, it is important to acquire detailed

information on the characteristics (n_e and T_e, atom and ion density, expansion rate, species distribution, etc.) and the physical chemistry of the laser-induced plasmas.

The present chapter provides a basic framework for several concepts involved in laser plasmas starting with the definition of plasma and its parameters. Short notes about laser matter interaction and stages of plasma formation and explanation of temporal and spatial evolution of laser-induced plasma will be reviewed, followed by a description of various methods used for the measurements of n_e and T_e. Finally, we introduce a brief review of recent experimental works on laser induced plasma. Throughout this review, plasma modeling approaches are also listed to enhance our knowledge of laser-induced plasma processes and dynamics.

1.2 What is Plasma?

Plasma is a quasineutral gas of charged and neutral particles, which exhibits a collective behavior [10].

Quasineutrality means that the negative and the positive charge densities are (almost) equal, which is the requirement for the plasma to resist against external potentials. Creating a plasma produces a cloud of electrons and positively charged ions, where electrons are more mobile than ions. Hence, we can visualize this charge cloud as stationary heavy ions surrounded by moving light electrons. If every ion is surrounded by enough electrons, a sphere with a zero net charge will be formed. The minimum radius of this sphere is known as the Debye length. Plasma is said to be quasineutral if the Debye length "λ_D" is significantly less than the plasma's characteristic length "L". Moreover, the Debye sphere is statistically valid when it contains a large number of particles "N_D".

To define the "collective behavior", assume that we have an ordinary molecule, such as air molecules, which are generally neutral and so light that they are not affected by gravity. Consequently, they move undisturbed until they collide with another particle. Thus, in a neutral gas, the movements of the molecules are controlled by collisions. In contrast, plasma contains charged particles, so the motions of these particles create magnetic fields and regions of space with net positive or negative charges. These space charges create electric fields. The

Coulomb force that describes the electrostatic interaction decays only slowly as r^{-2}, which resulting in a long-range force. At this moment, the motions of individual particles can no longer be described by local collisions, but each particle influences many nearby charged particles, which provide a collective behavior of the plasma.

One last difference that distinguishes a plasma from a neutral gas is that the plasma frequency is much larger than the electron-ion collision frequency. Assume plasma contains mobile electrons which are slightly displaced from the nearby ions, resulting for example from the random movements of electrons. Then the Coulomb restoring force will cause these electrons to oscillate about their equilibrium position. The periodic motion of the electrons is called the plasma frequency (f_p, $\omega_p=2\pi f_p$). If the frequency of this motion is greater than the collision frequency of the individual particles υ, then the individual particle collisions can be ignored.

To summarize, a plasma must meet three requirements:

1. The Debye length is much less than the characteristic length of the plasma $\lambda_D << L$.

2. The number of charged particles within the Debye sphere is very large $N_D >> 1$.

3. The oscillation frequency of the plasma is large compared to the collision frequency of individual particles $\omega_p >> \upsilon$.

1.3 Basics of Laser-Matter Interaction and Processes in Laser-Induced Plasma

In this section, the laser ablation process will be presented according to three steps: plasma ignition, plasma expansion and plasma cooling. Figure (1-1) summarizes these steps and the various mechanisms that they involve.

When a ns laser pulse impacts a solid target material (metals, semiconductors or dielectrics), within the first few nanoseconds, the surface electrons acquire an electromagnetic energy and hence gain enough kinetic energy to leave the target surface [11]. As a consequence, a thermal ablation is the dominant mechanism during plasma ignition (i.e. the temperature of the solid surface increases and direct sublimation or melting occurs followed

by evaporation, boiling or phase explosion) as electrons and ions will be in thermal equilibrium and heating [12].

Target breakdown is not a well-defined processes but it consists of complex body of processes such as multi-photon ionization, coulomb explosion, cascade ion ionization, electrostatic ablation and thermal ablation, which are dependent on both the irradiated target and the ablation laser. In case of ns laser, the process of target breakdown is initiated by multi-photon ionization process which creates the seed electrons. These electrons produce ionizing collisions with the neutral atoms which yield to a cascade of electrons by an electron-ion inverse Bremsstrahlung (avalanche ionization). These processes can be described respectively as follow:

$$A + mh\nu \xrightarrow{yields} A^+ + e^-$$

$$A + e^- \xrightarrow{yields} A^+ + 2e^-$$

where A and A^+ are the atoms or molecules of the target and the singly charged ion of the species and m is an integer number.

Accordingly, the plasma grows rapidly, producing an extremely energized cloud of electrons and ions, a plasma plume. During this stage of plasma ignition, laser irradiance and pulse duration controls the type of mechanisms and plasma properties. A detailed discussion of these complex processes and gas-dynamic aspects of laser-induced plasma propagation can be found in [13-15].

At that time, the emission is dominant by the background continuum (Bremsstrahlung radiation) resulting from electron–ion collision and recombination from the plasma free electrons. When sufficient number of electrons is generated, the dominant laser absorption mechanisms make a transition to electron-ion inverse Bremsstrahlung. Photo-ionization of excited states can also contribute in the case of interactions with short wavelength radiation. Although continuum background is very intense, the ion lines can rapidly be detected. The fast spatial growth in this step lasts for about hundreds of nanoseconds.

The preceding process leads to the next stage, where the plasma continues to grow for a few microseconds, but at a reduced rate. The various ion transitions present at early times are

detected and distinguished from the plasma plume background continuum emission. In this stage, the expansion strongly depends on the initial plasma properties (e.g. n_e, T_e and energy of plume). Furthermore, the ambient gas begins to play an important role in the shape, size and speed of propagation of the plasma plume. The interaction of the plasma plume with the ambient gas can be described by two mechanisms, depending on the gas pressure and nature: (i) the expansion of the high pressure plasma compresses the surrounding gas and drives a shock wave; and (ii) the plume energy is transferred to the ambient gas by thermal conduction, by radiative transfer or by both of them.

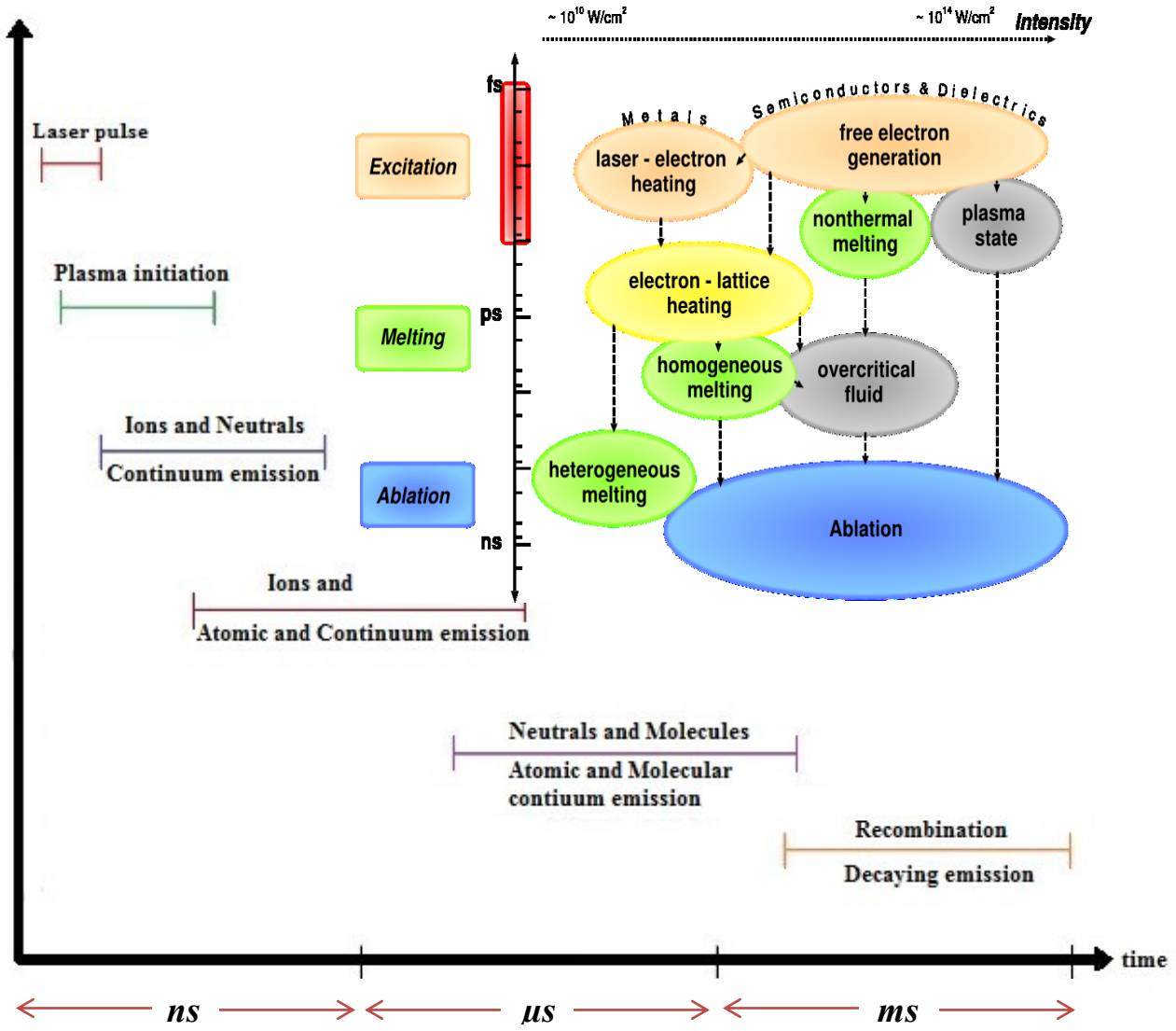

***Figure (1-1)**: Temporal development of laser-induced plasma processes and emission radiation. Inset Figure is taken from reference [16].*

Plasma cooling takes place after about 1μs when the plume vapor temperature reaches the boiling temperature of the target material and stops at the condensation temperature of the material. At this step, the plasma begins to decay due to electron and ion recombination yielding neutral atoms and both T_e and n_e decrease. This recombination process lasts for tens of microseconds. Consequently, the number of neutral atoms increases in the focal volume and the spectral lines associated with these neutral atoms are clearly observed during this period.

As the plasma cools drastically through radiative transfer and quenching processes, emission in the visible spectrum increases, continuum emission decreases, and distinct spectral lines become prominent. This time period lasts from approximately 1-40 μs following the laser pulse. It is ideal for capturing and analyzing atomic spectra that can be used for example in laser induced breakdown spectroscopy applications.

n_e and T_e further decays beyond 40 μs as atoms combine to form molecules. Molecular spectral bands thus appear and are detected along with fading atomic lines. The plasma continues to emit out to hundreds of microseconds following the initial laser pulse, but the useful signal is strongly diminishes with time. The plasma completely ends when no more emission is detectable and the volume is almost fully occupied by neutral constituents at or near ambient conditions.

As discussed above, laser ablation involves complex non-linear physical and chemical mechanisms that span several orders of magnitude in time with respect to the different predominant emitting species under ambient conditions and to the different physical phenomena observed during the plasma expansion.

As a closing remark for this section, there are many challenges in obtaining quantitative and qualitative data about the spatial and temporal conditions. In order to overcome these challenges, most researchers have utilized the visible, near ultraviolet or near infrared spectral regions, due to the ease of using conventional spectrometers and also to the higher availability of atomic data for these spectral regions. However, VUV spectroscopy has been used to characterize the early phase of plasma generated in vacuum and for detecting the UV line emission from light elements in high ionization degree [17].

1.4 Laser plasma diagnostics

Laser plasma diagnostics are designed to provide information about microscopic and macroscopic parameters such as the number densities and temperatures of the different plasma species, i.e. ions, electrons and neutral atoms, as a function of space and time. Among the aforementioned, of prime importance are the magnitude and the temporal and spatial evolution of n_e and T_e, which are the key parameters of laser ablated plumes.

There are several diagnostic techniques employed for the determination of these parameters, which include plasma emission spectroscopy, laser-induced fluorescence, Langmuir probe, magnetic B-dot probe, self-excited electron plasma resonance spectroscopy, microwave and laser interferometry, and Thomson scattering. Thomson scattering is a direct and less theory-dependent diagnostic, but unfortunately, the very low cross-section of the underlying process makes the experimental technique very difficult in practice. In the other side, plasma spectroscopy diagnostic techniques, which will be described in details in the following section, can be divided into two categories: (1) optical emission diagnostic techniques, analyzing plasma emission spectra, and (2) diagnostics based on radiation introduced into the plasma such as laser-induced fluorescence or absorption spectroscopy. Plasma emission spectroscopy is the simplest and for many parameters the most appropriate diagnostic technique, though several approximations are required to interpret the emission spectra.

1.4.1 Emission spectroscopy techniques

Emission spectroscopy is an in-situ, non-intrusive method, selective to species and quantum level. It can provide an excellent spatial and temporal resolution. The most useful methods for determining the plasma parameters are based on the optically thin emission of spectral lines.

In the optical emission spectroscopic techniques, we have two main contributions to the spectrum, (1) emission from the plasma itself, including continuum and line radiation; (2) emission due to scattering of the incident laser light by different modes in plasma. In our

study, we will only consider the spontaneous emission, which provides information about the plasma temperature and the electron and ion densities.

Plasma emission consists of continuum radiation (Bremsstrahlung and recombination radiation) and line radiation. The Bremsstrahlung radiation is caused by free-free transitions and occurs when a free electron is accelerated by a scattering interaction with an ion. The electron is free before and after the acceleration process, hence the designation as free-free transition. This process takes place during the initial plasma expansion.

The recombination radiation or free-bound radiation occurs when an initially free electron is captured by an ion. The spectrum of recombination radiation will therefore show sudden jumps representing recombination in different energy levels. This process takes place when the plasma cools down during the relaxation process and it strongly depends on the n_e, the ion charge and T_e.

Line radiation or bound-bound radiation occurs when transitions are made between bound states of an atom. The emission may come either from resonance transitions (transitions to ground state) or from transitions between different excited states. The intensity of the ion and atomic lines depends on the position in the plasma and reflects the local temperature of the plasma.

In laser plasmas, the spatial behavior of plasma emission shows that the Bremsstrahlung radiation is emitted close to the target surface. As the plasma plume expands away from the target, the line emission becomes dominated by radiation, the highly ionized lines being emitted close to the surface and the atomic lines farther from the plasma. The temporal behavior of the plasma emission is schematized in Figure (1-1) and it lasts for 10s to 100s of microseconds after plasma ignition until it cools down.

Measuring line intensity, broadening and shift can yield valuable information on electron and ion densities, temperatures and plasma motion. Several factors determine the line shape; these are the natural line broadening (quantum effect), the thermal motion of atoms (Doppler broadening), the interaction of the radiation system with plasma (pressure broadening), perturbation of the energy levels by the electric fields (Stark broadening and

shift) and by the magnetic fields (Zeeman Effect). Zehang *et al*. [18], came up with criteria to selecthe appropriate lineses for a better estimation of different plasma parameters:

(1) The lines must have reasonable line-to-background intensity ratio.

(2) The spectral efficiency should be measured accurately.

(3) The greater the gap between the upper energy levels of selected lines, the better the accuracy of temperature measurement.

(4) The accuracy of spontaneous transition probability is relatively high.

(5) Special care should be taken to avoid the lines of self-absorption resonance or having low-lying energy levels.

Indeed, the determinations of the n_e by the Stark broadening effect, as well as the measurement of T_e using the Boltzmann and Saha–Boltzmann equations require that the spectral lines are optically thin. If this condition is not satisfied, that is, if the lines used for characterization suffer from self-absorption, their line profiles show distorted widths and areas that lead to wrong values of n_e and T_e. Optically thin plasma should satisfy the following criteria [18] ;

(1) For the multiple lines of a species whose lower/upper terms have a single level, the intensity ratio of them is in accordance with the statistical weight ratio.

(2) The intensity ratio of two atomic lines having the same upper level energy should be within the limit defined by a branching ratio

(3) The optical depth of the plasma should be much lower than 1.

(4) The value of self-absorption coefficient should be close to 1.

(5) The curve of growth of the line should be a straight line.

In the experiments, a lens collected plasma emission from the ablation plume and the image is focused on the narrow entrance slit of the spectrometer. This slit spatially limits the plume image to its shape. This new image is focused via a series of mirrors onto an optical grating dispersing the emission into its many optical wavelengths. The resulting rectangle image is then imaged onto a rectangular CCD matrix. The CCD matrix is composed of a

rectangular array of pixels, which are individual photon detectors. Therefore, each column of the matrix corresponds to a particular wavelength. Plots of photon counts (corresponding to light intensity) as a function of wavelength are then produced by adding the total photon counts from all the pixels in a column and associating that count with the wavelength corresponding to that column. It's worth to note that the statistical error is reduced by repetitive sampling of the emission, which is generated in successive laser shots during wavelength scanning of the spectrometer.

It is obvious that, due to their transient nature, laser-induced plasmas are spectroscopic sources that display fast spatial and temporal evolution of their characteristic parameters such as the populations and temperatures of the various species present in the plume. For this reason, in plasma plume spectroscopy, measurements are usually carried out using time-resolved detection. In this way, it is possible to identify the line spectrum and its evolution as plasma expands and decays, and to isolate the strong continuum emission present at early times.

Depending on the required information and experimental conditions, a 100 ns resolution time is often sufficient to measure the evolution of the spectral line emission. However, for early continuum emission a shorter time resolution of nanosecond can be achieved by using a solid-state multichannel detector or a gated intensified charge-coupled device (ICCD) detector [17]. Radziemski *et al.* [13] used a linear diode array to gecharacterizeime resolution to characterise laser plasmas generated at atmospheric pressure. On the other hand, Sony George *et al.* [19] described the effect of ambient gas on the growth dynamics of plasma plume of multi-layered LiF-C thin film using an ICCD camera with 4 ns gate opening (integration time). Hermann *et al.*[20] used a fast ICCD to diagnose laser-induced plasmas generated with a femtosecond laser in air, He or Ar at pressures ranging from 10^{-2} to 10^{5} Pa with an observation gate of 10 ns. Finally, Hermann *et al.*[21] used a fast photomultiplier to characterize the early continuum emission of laser-induced plasmas generated from a Ti target at a low pressure N_2 atmosphere with a time resolution of 2 ns.

On the other side, laser-induced plasma parameters have significant gradients in the spatial distributions in both axial and radial directions. In the experimental point of view, the spatially-resolved characterization of laser-induced plasma depends on the selection of the

light collection system, the spectrometer and the detector [17]. The preferred setup system was carried out based on a fiber-optic cable, which prevents problems related to the dependence of focusing on wavelength in a very large spectral range and avoids the effects of chromatic aberration of focusing lenses. The emission of plasma plume was collected along the line-of-sight, the plasma parameters are population-averaged on the entrance of the fibre-optic by varying the position of the optical fibre in the image plane for axial measurements [21-23] and in the transverse plane for radial measurements [24]. Using the same procedure a two-dimensional grid of measurements of the plasma emission was also obtained [25].

1.4.2 Measurement of electron density

The electron density can be calculated from Stark broadening of lines, for densities typically $\geq 10^{14}$cm^{-3}. Besides natural broadening and instrumental broadening, other causes such as Doppler broadening, pressure broadening and Stark broadening may also contribute to the line shape. Stark broadening is extracted from the line shape by removing the other types of non-Lorentzian broadening. Once other broadening components have been removed, a Lorentzian curve can be fitted to the Stark component. n_e can be obtained from the full-width at half maximum (FWHM) from the relation [26]

$$n_e \approx \frac{1}{2\omega}(\Delta\lambda_{1/2}10^{16}), \qquad (1\text{-}1)$$

where $\Delta\lambda_{1/2}$ is the FWHM of the peak (in Å); ω is the electron impact parameter, which can be found in the comprehensive text by Griem [27]. The Stark width is a function of the T_e, but this dependence is weak and it is most often neglected. Stark widths have been calculated for numerous transitions of the neutral and singly-ionized states of about twenty elements [27], with additional work currently underway [28, 29].

Experimental evidence indicates that the electron densities determined using the calculated width parameters are subject to 20% error. These errors are mainly due to the uncertainty on Stark width measurements and on the theoretical calculations of the Stark broadening parameter ω. On the other hand, the calculations of Stark width for ion lines have a lower accuracy than those of neutral lines [27].

Although Stark broadening cannot be easily distinguished from other competing broadenings, such as Doppler and instrumental broadening, the spectra could be corrected for these second-order effects, in order to prevent them from exaggerating the extent of Stark broadening [30]. Instrumental broadening was reduced as much as possible by minimizing the entrance slit width of a high-resolution spectrograph. The effects of Doppler broadening, $\Delta\nu_D$, can be found through the relation:

$$\Delta\nu_D = \frac{\lambda v_z}{c} \qquad (1\text{-}2)$$

where v_z is the velocity of the emitting particle, c is the speed of light in a vacuum, and λ is the transition wavelength. In laser-induced plasma, n_e is large, so the effects of Doppler broadening are expected to be small, and Stark broadening is the dominant broadening mechanism [30].

Other methods can be used to determine the n_e, such as Stark shift and the Saha-Boltzmann equation. In the Stark shift method, n_e is determined from the wavelength shift of the line profiles. The shift value is compared with those predicted by the approximated formula in Griem's book [27] that gives the total Stark shift d_{total} as a function of the n_e.

$$d_{total} \approx \left[\frac{d}{w} \pm 2A(1 - 0.75R)\right] w \frac{n_e}{n_e^{ref}} \qquad (1\text{-}3)$$

where d is the electron-impact shift parameter, A is the ion broadening parameter, which is a measure of the relative importance of the collisions with ions in the broadening, and n_e^{ref} is a reference n_e, usually of the order of 10^{16} or 10^{17} cm^{-3}, at which the parameters ω and A are measured or calculated. The parameters ω and A are weak functions of temperature. R is the ratio of the mean distance between ions and the Debye radius.

The determination of n_e by the Saha–Boltzmann equation described in equation (1-5) consists in using the Boltzmann plot method to obtain the plasma temperature, discussed in the next section. Then, one can introduce the temperature values in the Saha–Boltzmann equation to deduce n_e. The calculated values of n_e are within a factor of about 2 from that calculated from Stark broadening method [17].

Due to the uncertainties related to the shift parameters calculations, as well as those on the transition probabilities and temperatures, these last two methods only provide an approximate measurement of n_e [31].

1.4.3 Thermodynamic Equilibrium and Temperature determination

Several processes generate spectral emission in plasmas. These include collisional excitation, radiative excitation, de-excitation, ionization, and recombination, which involve numerous energy levels and stages of ionization. The rate at which these processes occur, the relative populations of the energy levels and the velocity distributions of the particles can be described through the concept of temperature. If all forms of energy distributions are described by the same temperature, a complete thermodynamic equilibrium exists. In reality, this complete thermodynamic equilibrium is rarely achieved, so a useful approximation of Local Thermodynamic Equilibrium (LTE) can be introduced.

The (LTE) model assumes that the collision rates surpass the radiative ones, so that the non-equilibrium of radiative energy can be neglected. This is usually verified beyond a certain critical electron density, n_c. The system can be described by a single temperature, if the plasma parameters, the population density and plasma ionization are locally governed by the Boltzmann and Saha equilibrium relations and the population of the excited levels for each species follows a Boltzmann distribution.

The Boltzmann equation, which defines the population densities N_j^z of excited energy levels as a function of temperature T is given by [32]:

$$\frac{N_j^z}{N^z} = \frac{g_j e^{-\frac{E_j^z}{KT}}}{U^z(T)} \qquad (1\text{-}4)$$

Where the superscript z refers to the ionization degree ($z = 0$ for neutral atoms, $z = 1$ for singly-charged ions), N^z is the number density, E_j^z and g_j are the energy and degeneracy of the j-th level, $U^z(T)$ is the partition function and k is the Boltzmann constant.

The Saha equation relates the densities of subsequent ionization species for a temperature *T*. It is given by [32]:

$$\frac{n_e N^z}{N^{z-1}} = \frac{2U^z(T)}{U^{z-1}(T)}\left(\frac{2\pi mkT}{h^2}\right)^{3/2} e^{-\frac{E_\infty^{z-1}-\Delta E_\infty^{z-1}}{kT}} \qquad (1\text{-}5)$$

where E_∞^{z-1} is the ionization energy of species $z-1$ for isolated systems, ΔE_∞^{z-1} is the correction of this quantity for interactions in the plasma, *h* is Planck's constant and *m* is the electron mass.

Let us assume that the electrons have a Maxwellian distribution with a temperature, T_e. The corresponding number of electrons with velocities between *v* and *v*+*dv* is given by [33]:

$$dn_e(v) = 4\pi n_e \left(\frac{m}{2\pi KT_e}\right)^{3/2} exp\left(\frac{-m_e v^2}{2KT_e}\right) v^2 dv \qquad (1\text{-}6)$$

Under the assumption of local thermodynamic equilibrium, T_e and n_e describe the plasma, provided the $n_e > n_c$. The latter is determined by the necessary, but not sufficient, condition known as the McWhirter criterion, which states that the LTE model is valid for [34]:

$$n_c \geq C\sqrt{T_e}E_{max}^3\ cm^{-3} \qquad (1\text{-}7)$$

where *C* is a numerical constant, E_{max} is the highest ionization energy of a given atom/ion species within the plasma (in eV).

In addition, there are two more criteria to confirm the existence of LTE in the plasma. One of them is the agreement between the excitation and ionization temperature measurements deduced from the Boltzmann and Saha–Boltzmann equations, respectively. The other criterion is an agreement between the Boltzmann distribution and the experimentally measured line intensities, which is reflected in the linearity of the Boltzmann plot [17].

In laser-induced plasmas, the temperature usually refers to the excitation temperature, which is a measure of the distribution of excited atomic or ionic populations within the plasma. In order to equalize this temperature to the electron temperature, the assumption of (LTE) has to be satisfied in each small volume element of the plasma being examined.

Among the various methods for determining the T_e, thermal Doppler broadening is the most direct. This method is used for light elements and high central wavelengths. However, it is hardly useful at high pressure, because of pressure broadening that usually dominates the line width, and at high temperature, due to lack of resolution for the lines which are at short wavelengths [17, 35].

The Boltzmann plot is the most widely used method for the determination of the excitation temperature, hence electron temperature if LTE is assumed. This method can be easily implemented as it consists in plotting the spectral line intensities of the plasma as a function of the level energy [17, 35, 36]. The time-integrated, spatially resolved T_e is directly determined from the spectral lines of given species through the relation [26, 32]

$$\ln\left(\frac{I_{mn}\lambda_{mn}}{hc\, g_m A_{mn}}\right) = -\frac{E_m}{kT_e} + \ln\left(\frac{N(T)}{U(T)}\right) \qquad (1\text{-}8)$$

where λ_{mn} , A_{mn} and g_m are the transition wavelength, the transition probability and the statistical weight of the upper level, respectively. E_m is the upper level energy, $U(T)$ the partition function, and $N(T)$ the total number density of neutrals.

For a more accurate T_e determination, many transitions must be used. The temperature is then calculated by applying the following relation to each of the n fully resolvable transitions [17, 26, 32]

$$kT_e = \frac{-E_n}{\ln\left(\frac{I_n\lambda_n}{g_n A_n}\right)} \qquad (1\text{-}9)$$

T_e is thus expressed as the linear slope of a

$$\ln\left(\frac{I_n\lambda_n}{g_n A_n}\right) \text{ vs } E_n \text{ plot.} \qquad (1\text{-}10)$$

Boltzmann plot is a very interesting method frequently used to determine the temperature of laser-induced plasmas produced in various experimental conditions. For example, very high temperatures can be measured at the early phase after plasma creation using the Boltzmann distribution of emission lines in the visible, near ultraviolet and near infrared regions. At this stage, it has been reported that the uncertainties on the measured T_e values are large at small time delays due to the extreme broadening and partial overlap of the spectral lines resulting from the very high electron densities of the plasma at initial times [17].

In order to overcome this problem, the emitted lines used for the calculation of Boltzmann plot method should be at least 7 to 10 lines, distributed over a large energy range and has a well-defined line profile (no self-absorption).

On the other hand, one of the best methods used to determine the T_e during the early phase of laser-induced plasma is line to continuum intensity ratio, provided the line and continuum emission are of comparable magnitude [37]. The ratio of the line emissivity ε_l of a neutral atom line to continuum emissivity $\varepsilon_{\lambda,c}$ is given by [38]:

$$\frac{\varepsilon_l}{\varepsilon_{\lambda,c}} = \frac{3^{3/2}h^4c^3\varepsilon_0^3}{4e^6k}\frac{A_{mn}g_m}{U_i(T)}\frac{\lambda_c^2}{\lambda_l}\frac{\exp(\frac{E_\infty - E_m - \Delta E_\infty}{kT_e})}{\xi\left(1-exp\frac{-hc}{\lambda kT_e}\right)+Gexp\frac{-hc}{\lambda kT_e}} \qquad (1\text{-}11)$$

where $U_i(T)$ is the partition function for the ion, λ_c and λ_l are the continuum wavelength and central wavelength of the neutral atom line, respectively, ε_0 is the permittivity of free space, e is the elementary charge, G is the free-free Gaunt factor and ξ is the free-bound correction factor.

Equation (1-11) contains all the physical dependence of the ratio of the (integrated) line emission intensity to the (non-integrated) continuum intensity on T_e. Provided that its constants can be easily calculated, this relationship is used for the determination of T_e assuming LTE. It is worth noting that this method does not depend on the spectral resolution since: (a) the continuum level is automatically integrated over its own bandwidth by the apparatus and (b) the integration of the emission intensity yields the bandwidth of the apparatus, this bandwidth being much larger than the line width [17, 39].

1.5 Literature Review of Laser-plasma Diagnostics under the effect of ambient gas

The temporal and spatial characteristics of laser-induced plasmas are highly dependent on the ambient atmosphere and on the target material [28, 29]. This directly impacts the optimization of the applications ranging from elemental analysis to nanoparticles and thin film synthesis. In addition, the plasma morphology and emission intensity are affected by the ambient gas pressure and composition due to the plume confinement in an extremely complex process [40].

The effect of ambient gas pressure on the plasma dynamics is characterized by three different pressure regimes. At low pressure < 1Torr, the plasma plume expands without collisions with the ambient gas molecules. As a consequence, no sharp boundary is formed and a high emission intensity of the plasma plume is obtained [41, 42]. This is the most proper regime for the synthesis of nanoparticles and thin films.

At intermediate pressure 1 < P < 20 Torr, the plasma becomes more collisional and consequently, the plume is narrower with a dense region formed between the expanding plasma plume and the ambient gas.

At high gas pressure > 20 Torr, the transition to a hydrodynamic regime takes place, with the plume acting as a piston on the surrounding ambient environment. This compressed region successfully shields the diffusion of ambient gas species to the plasma, which increases the plasma time life [43-45]. This regime is suitable for elemental analysis and other LIBS applications.

The experiments described in the following sections of this chapter use emission spectroscopy as the major diagnostic technique for the determination of plasma characteristics. It is worth to note that no single technique can provide all the information for the plasma characteristics. Therefore, each example in the following literature review refers to a particular technique.

1.5.1 Influence of pressure on emission intensity

Plasma parameters such as n_e and T_e, particle transport properties and ion distributions can be obtained from the emission spectrum. Therefore, the spectrum intrinsically contains the fingerprint of the plasma's physical state. As a consequence, many research groups utilize emission spectroscopy to establish the relationships between the plume's line and continuum emissions and the plasma characteristics.

Performing laser-induced plasma diagnostics at reduced pressure by utilizing femtosecond or nanosecond lasers shows a great enhancement of spectral intensity, signal-to-noise ratio (S/N), spectral resolution, ablated material quantity and ablation craters, which are suitable for synthesis of thin films and nanoparticles [46]. In the published data which study the effect of both gas pressure and composition on the plume emission, there exist contradictions in the results. Some of them reported an increase of the line emission intensity with pressure, where others reported a decrease with pressure. Furthermore, other research groups assume the existence of a favoured region, which varies with the gas type.

For instance, Figure (1-2) shows an example of Si spectra collected in vacuum conditions as compared to atmospheric pressure [47]. Cowpe *et al.* reported an improvement of the S/N ratio at lower pressure due to the decrease of n_e and continuum radiation. This result agrees with the work performed by Dreyer *et al.* [48] who examined a geological sample at reduced pressure using a Nd:YLF; Neodymium-doped yttrium lithium fluoride, laser with a 10 ns pulse duration. The obtained results, Figure (1-3), show the variation of the spectra with pressure.

On the other side, Yalcin *et al.* [49] studied the pressure dependence of emission intensity in femtosecond laser plasma for Al, Mg, Si and Cu. They reported a significant enhancement of the signal intensity at a selected reduced pressures varying with the type of the material. For example, at 4 Torr the emission spectrum of Al I line shows a great enhancement in the S/N ratio as compared to both high pressure and pressure down to 10^{-3} Torr, as shown in Figure (1-4). In addition, Bashir *et al.* [50], studied the influence of ambient gas and its pressure on laser-induced plasma of Cd. They reported that the emission spectrum shows an enhancement of the emission intensity in a preferred region of gas pressure, which

agrees with the Yalcin's results. Furthermore, this region depends on the type of the gas. For example in the case of Ar atmosphere, the intensity of all lines increases with pressure rising up to attain its maximum at 10 Torr, after that it decreases with pressure rising to reach a minimum at atmospheric pressure. A similar trend is observed for other gases like air and helium, but at different optimum pressures.

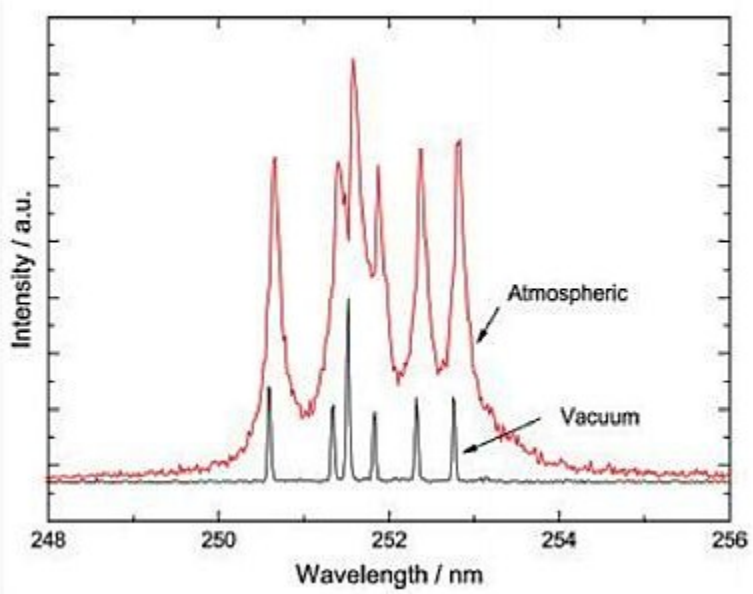

***Figure (1-2)**: Comparison of LIBS spectra of Si at atmospheric pressure and vacuum* [47].

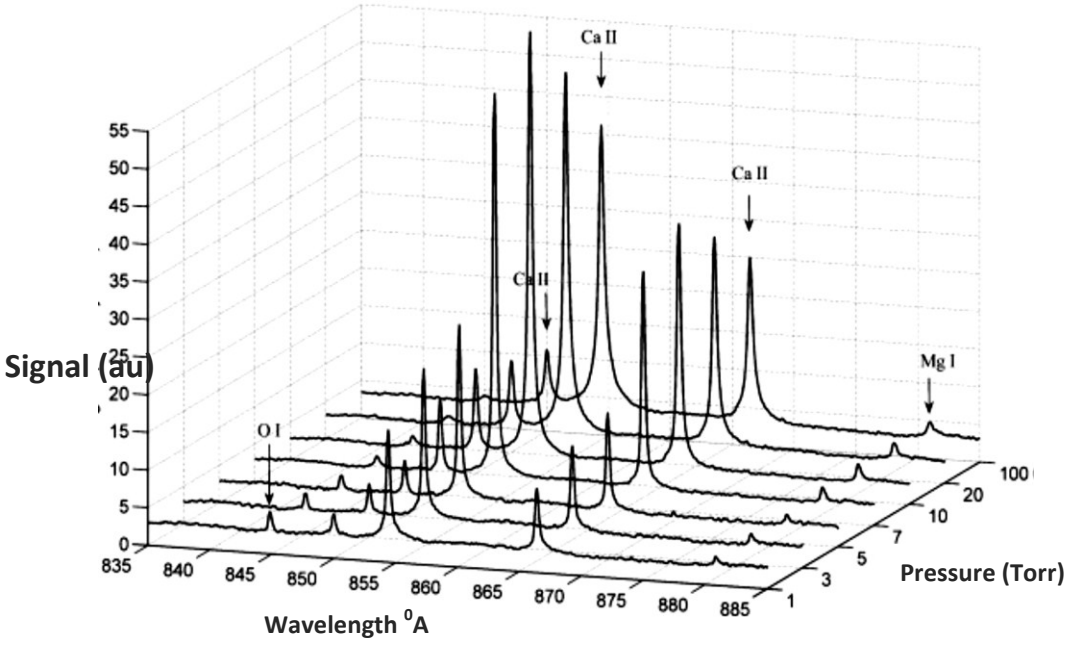

***Figure (1-3)**: LIBS spectra of a geological sample (oolitic hematite) at various pressures* [48].

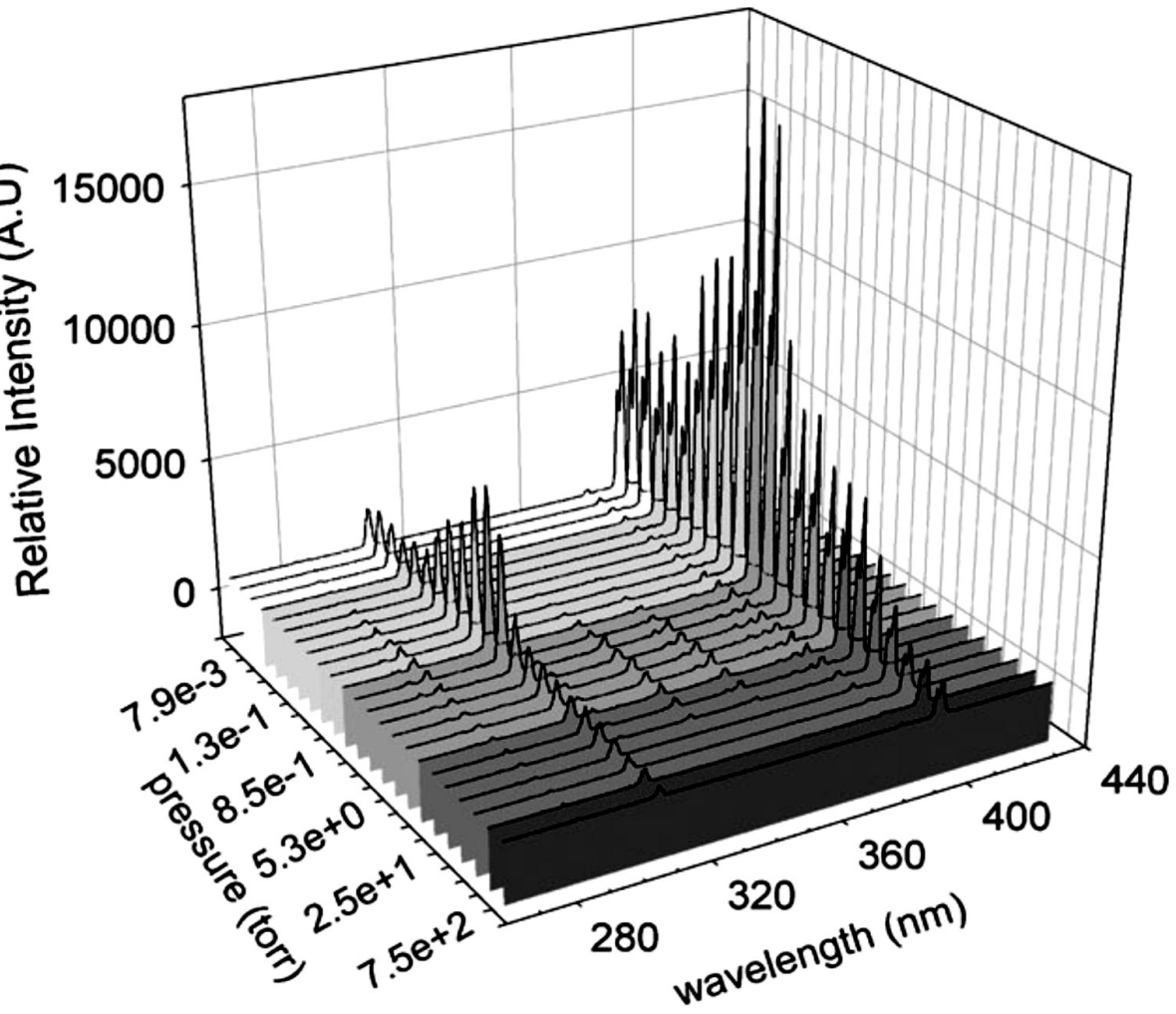

***Figure (1-4)**: Effect of air pressure on aluminium line emission intensities from Al-6061 alloy. Each spectrum has been obtained from a single laser pulse of 10 mJ energy, 10 ns delay time and 100 ns gate width. Neutral Al I lines at 308.2, 309.2, 394.6 and 396.1 nm show significant enhancement with rising pressure. Low concentration of Mg (383.8 nm), Fe (360 nm) and Cu (324.7 nm) lines present in the Al-6061 alloy are enhanced under low-pressure conditions* [49].

Cremers and Radziemski [41], and Amoruso *et al*. [36] shows that the emission intensity may be increased at low pressure owing to reduced plasma shielding; the later portion of the laser pulse is absorbed or reflected by the formed plume. Similar results are also reported by Lee and Sneddon [51] in their study of laser-induced plasma generated by ArF

excimer laser from a lead target. They find that gas breakdown in air and argon atmosphere, and the shielding effect of the laser beam seriously affect the ablation process and metal ion formation. Hence the atom and ion lines emission is strongly dependent on both gas pressure and composition. Furthermore, they reported that the ion emission decays more rapidly than the atom line emission. Figure (1-5) illustrates the ratio between the ionic and atomic lead emission spectra under pressure 760 to 10 Torr with different gas composition (air, argon, and helium).

As a closing remark of this section, it is clear that there exist contradictions in the published data which study the effect of both gas pressure and composition on the plasma emission.

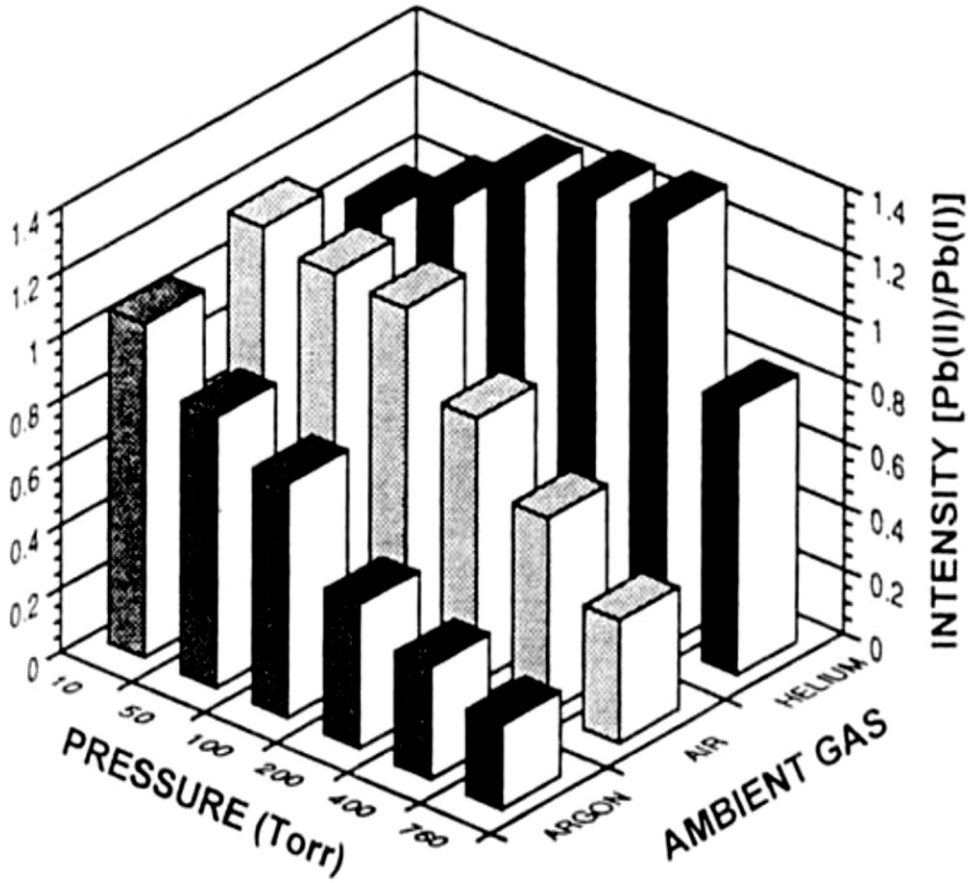

***Figure (1-5)**: 3-D plot of the intensity ratio for Pb(II)/Pb(I) at the pressure of 760 – 10 Torr under various atmospheric gases (air, argon, and helium)* [51].

1.5.2 Effect of ambient gas pressure on plasma density

Cowpe *et al.* [52] have investigated the effect of pressure on the temporal behavior of n_e of a Si plasma using Stark broadening from 10 to 1410 ns. Figure (1-6) shows that the n_e decreases with increasing pressure from 10^{-4} mbar to atmosphere, with a steep change between 1 mbar and 10 mbar. Furthermore, n_e follows a second order exponential decay with time.

n_e is in the range 10^{16}-10^{19}cm^{-3}, which in a good agreement with the values reported by Milan and Laserna [53] and Liu *et al.* [54] for Si and comparable to those achieved for other solid materials like zinc and Al as reported by Shaikh *et al.* [55] and Le Drogoff *et al.* [56], respectively.

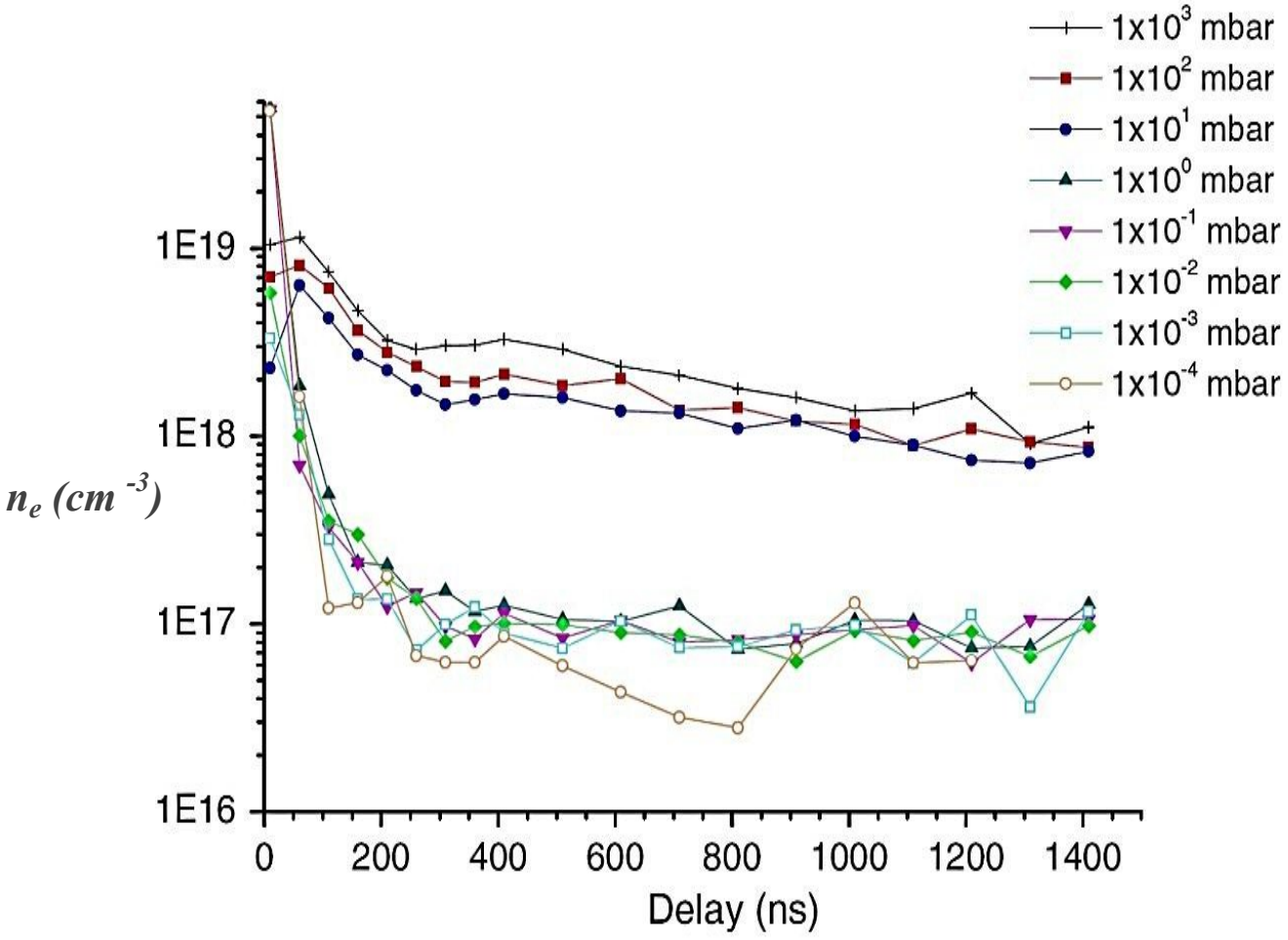

***Figure (1-6)**: Plasma n_e versus capture delay time, for ambient pressures in the range 10^3 to 10^{-4} mbar* [52].

On the other hand, Shaikh *et al.* [57] evaluated the pressure effect on the spatial behavior of n_e of a laser ablation brass plasma at 1000, 500, and 100 mbar argon pressures. They reported that in the initial stage, (0-2 mm), n_e decays rapidly as a result of the fast thermalization and recombination processes, followed by a slow variation at longer distances as shown in Figure (1-7).

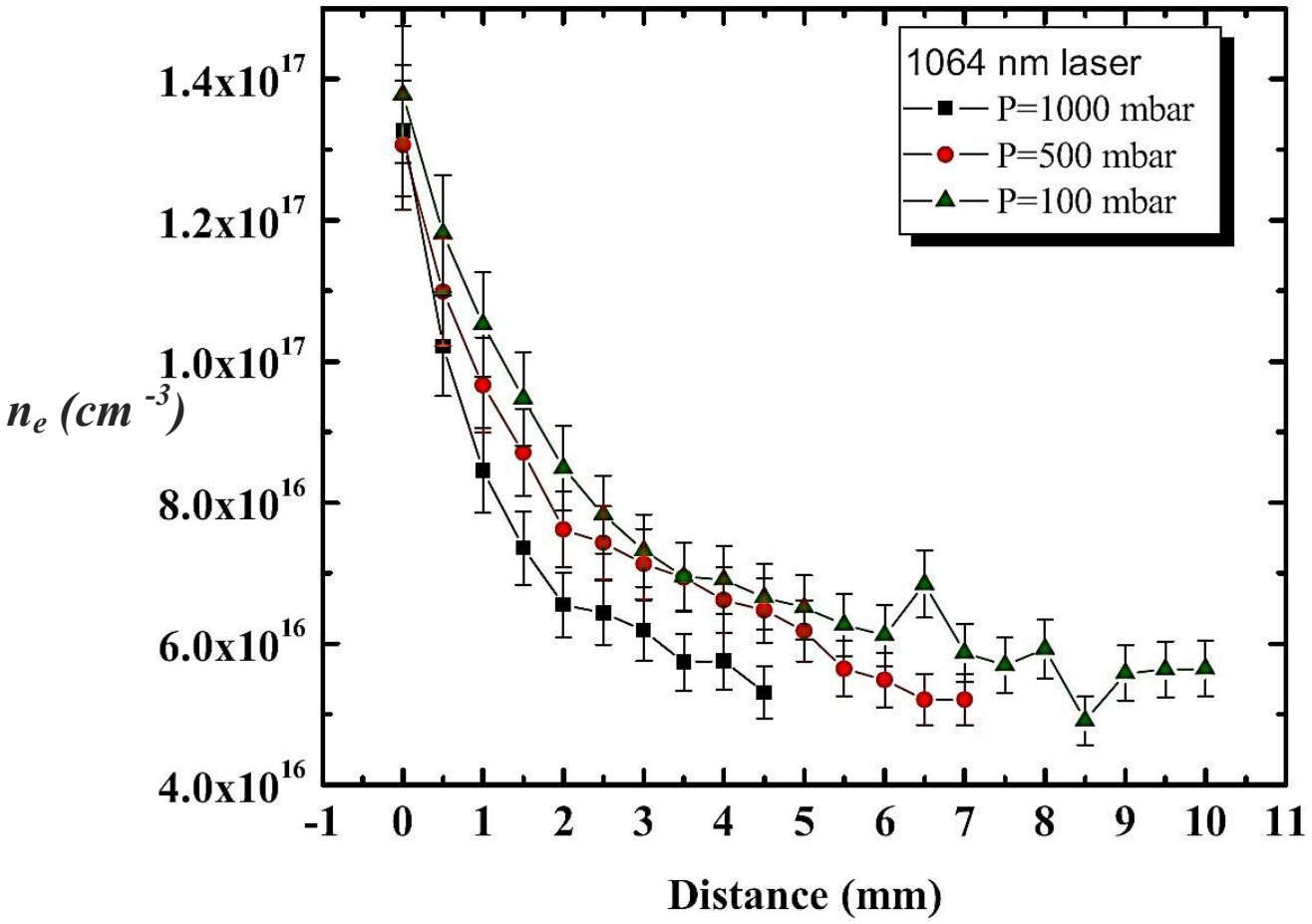

***Figure (1-7)**: Spatial variation of n_e at 1000, 500, and 100 mbar of the ambient gas* [57].

Aragon and Aguilera [8] studied the two-dimensional spatial resolution of the n_e distribution of iron laser-induced plasmas at different pressures of air, for pressure ranging from 1000 to 10 mbar. They reported that n_e distribution strongly varies with axial distance from the target, the plasma density being of about $1.6 \times 10^{17} cm^{-3}$ at the target surface and 10^{15} cm^{-3} at 15 mm with only a slight decrease when pressure varies from 10 mbar to 1000 mbar. They attribute such behavior to the fact that as the pressure increases, the plasma emission is

confined to a region of decreasing size and distance to the sample as shown in Figure (1-8). Similar results were obtained by Galila *et al.* [58] in their studies on Al plasma (Nd:YAG, 532 nm, 100mJ, 8 ns) under the influence of both vacuum and air at atmospheric pressure. The highest value of n_e was found at the beginning of plasma formation near the target surface, while the lowest values were found at both longer times and distances. Comparing these results with those calculated by Grant and Paul [4], shown in Figure (1-9), there is a good agreement within the uncertainties related to the parameters entering Stark broadening and Saha equations.

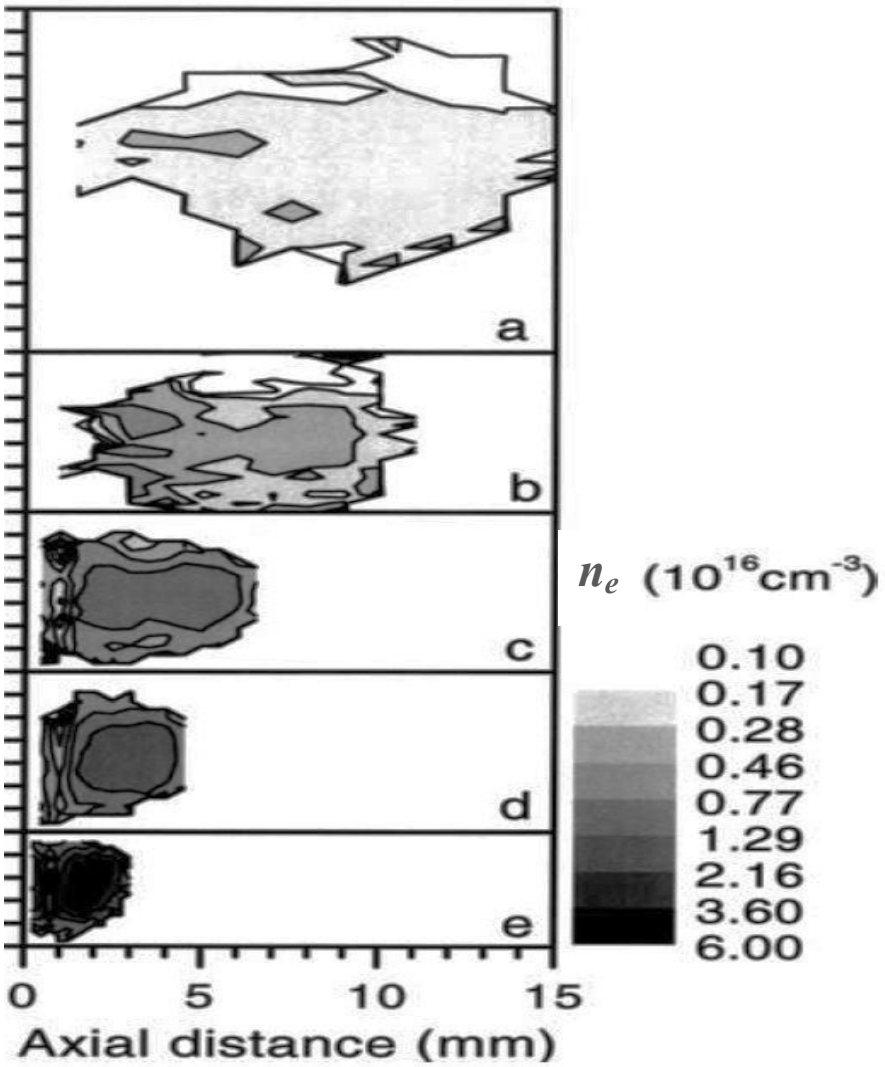

***Figure (1-8)**: n_e distributions of Fe plasma in the time windows 5-6 μs of the laser-induced plasmas generated at various pressures of air: (a) 10mbar, (b) 25 mbar, (c) 100 mbar, (d) 250 mbar, and (e) 1000 mbar* [57].

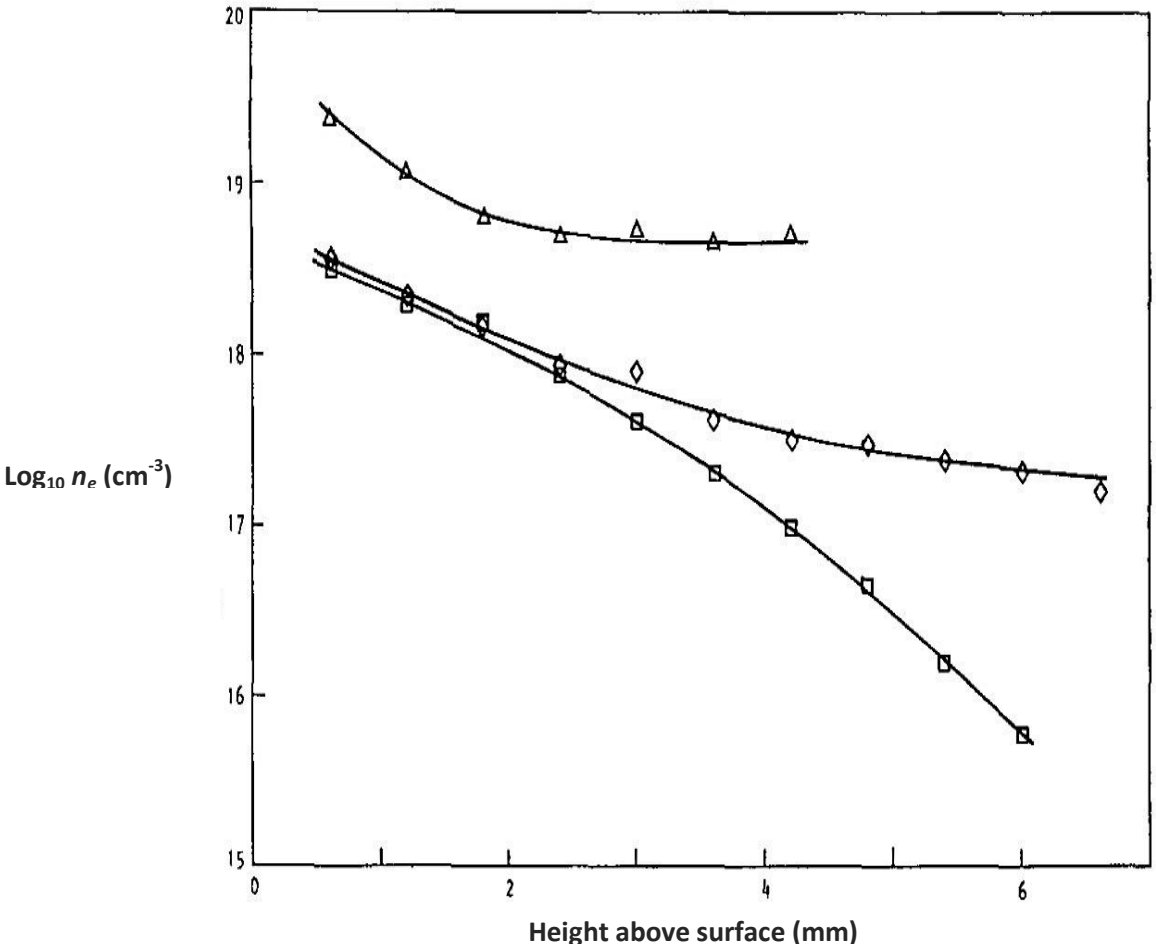

***Figure (1-9)**: Spatial evolution of n_e of Fe plasma formed by a Xecl excimer laser (308 nm, 10 ns) in air at pressures of 760 (Δ), 50 (◊) and 0.5 (□) Torr vs. the vertical heights* [4].

1.5.3 Effect of ambient gas pressure on plasma temperature

Cristoforetti *et al.* [59] used the Boltzmann plot of six Cu I lines from a brass target to calculate the T_e as a function of pressure as shown in Figure (1-10). For both laser single and double-pulses, they found that T_e increases with the ambient gas pressure up to 200 Torr. Then, a slight decrease T_e is observed, which is attributed to the collisions with the ambient gas.

On the other hand, Grant and Paul [4] used the Boltzmann plot of eleven Fe(I) lines to determine T_e in air at pressures of 760, 50 and 0.5 Torr.

Figure (1-11) shows the obtained spatial T_e profile with a maximum T_e of 22,000 K at 760 Torr and at 0.6 mm from the target, and a minimum of 9000 K at 0.5 Torr and 6.6 mm from the surface. Overall, T_e decreases with the decrease of pressure due to the less efficient confinement of plasma. Indeed, the plasma energy is distributed over a large volume that increases the cooling effect of the gas atmosphere depending on its thermal conductivity [60, 61].

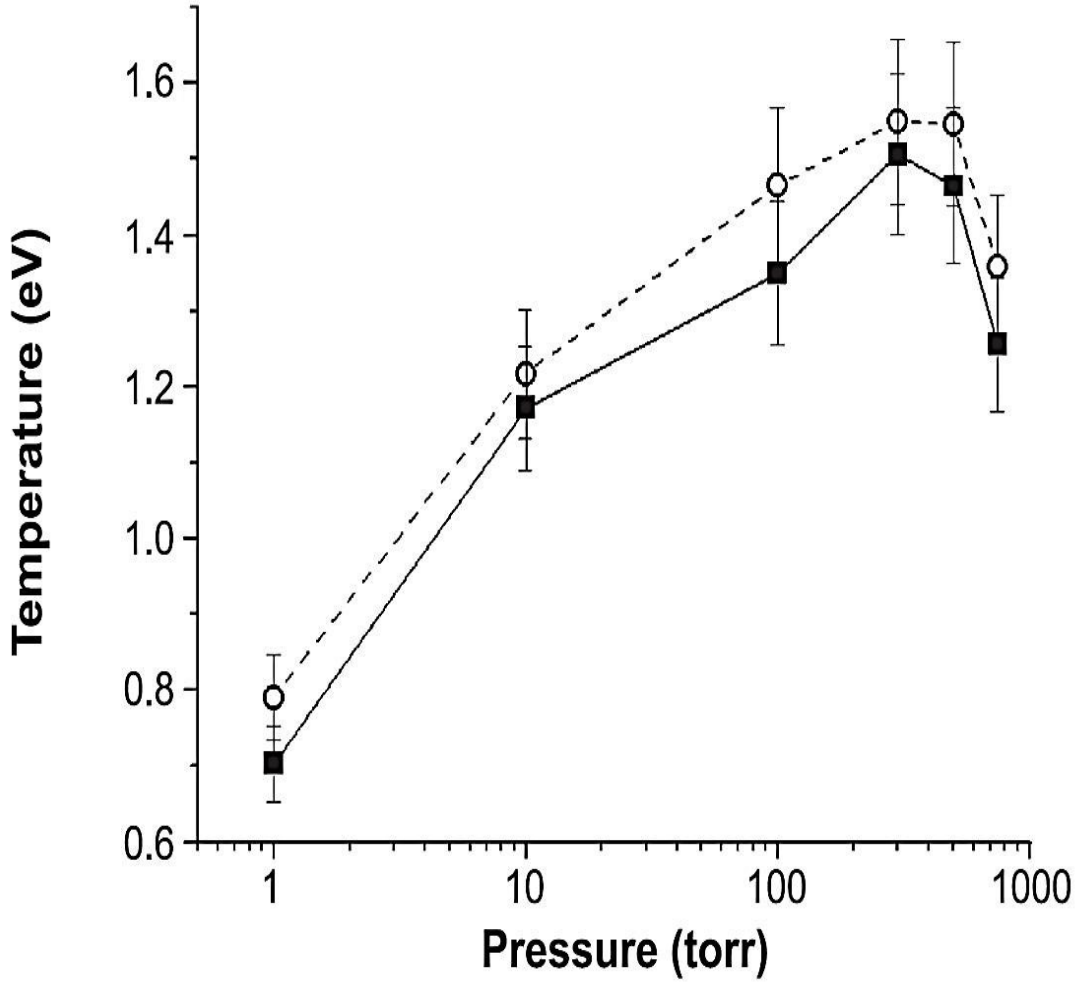

***Figure (1-10)**: Influence of the ambient gas pressure on T_e of Cu plasma produced by Nd:YAG single laser pulse of 80 mJ (squares) and by two simultaneous laser pulses with total energy of 160 mJ (circles)* [59].

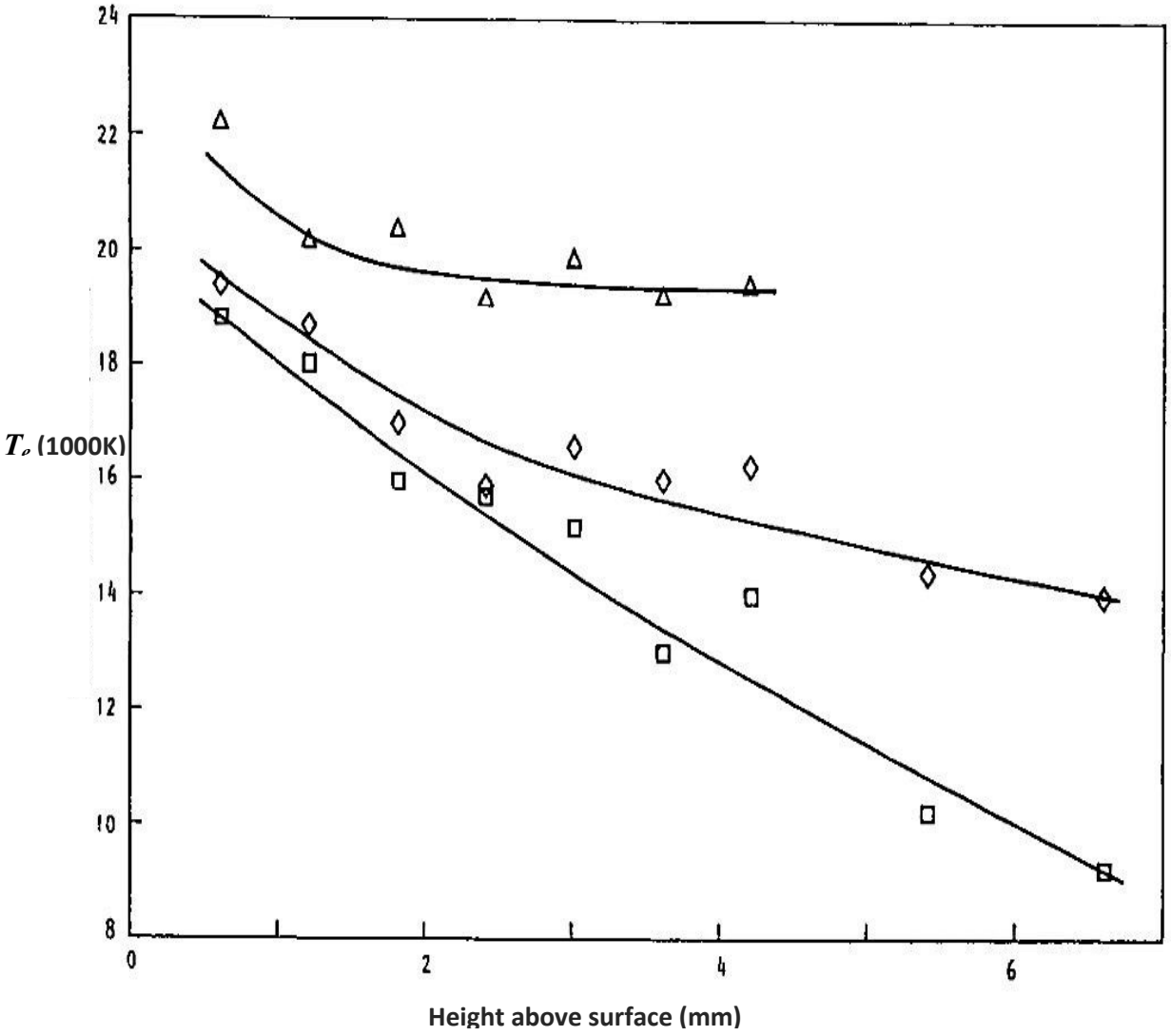

***Figure (1-11)**: Spatial T_e profile of Fe target formed by a XeCl excimer laser (308nm, 10 ns) in air at 760 (Δ) , 50 (◊) and 0.5(□) Torr* [4].

The influence of pressure on the temporal behavior of T_e of laser-induced plasma in air was reported by Glumac and Elliott [62]. The obtained profile, as seen in Figure (1-12), shows a slight increase in T_e with pressure at the time interval 50 to 150 ns that is attributed by the authors to the effect of optical depth as discussed in [63]. Moreover, the temporal T_e profile

observed at 0.1 atm is significantly different from that obtained at other pressures, likely because the N II lines were too weak to be correctly fitted.

In the other hand, Cowpe *et al.* [52] used the line-to-continuum ratio method to determine the temporal evolution of the Si T_e at air pressures varying from 10^3 to 10^{-4} mbar. They found a second order exponential decay as shown in Figure (1-13). The result shows a rapid decrease of T_e followed by a slow decay, in agreement with the previous results of Glumac and Elliott [62].

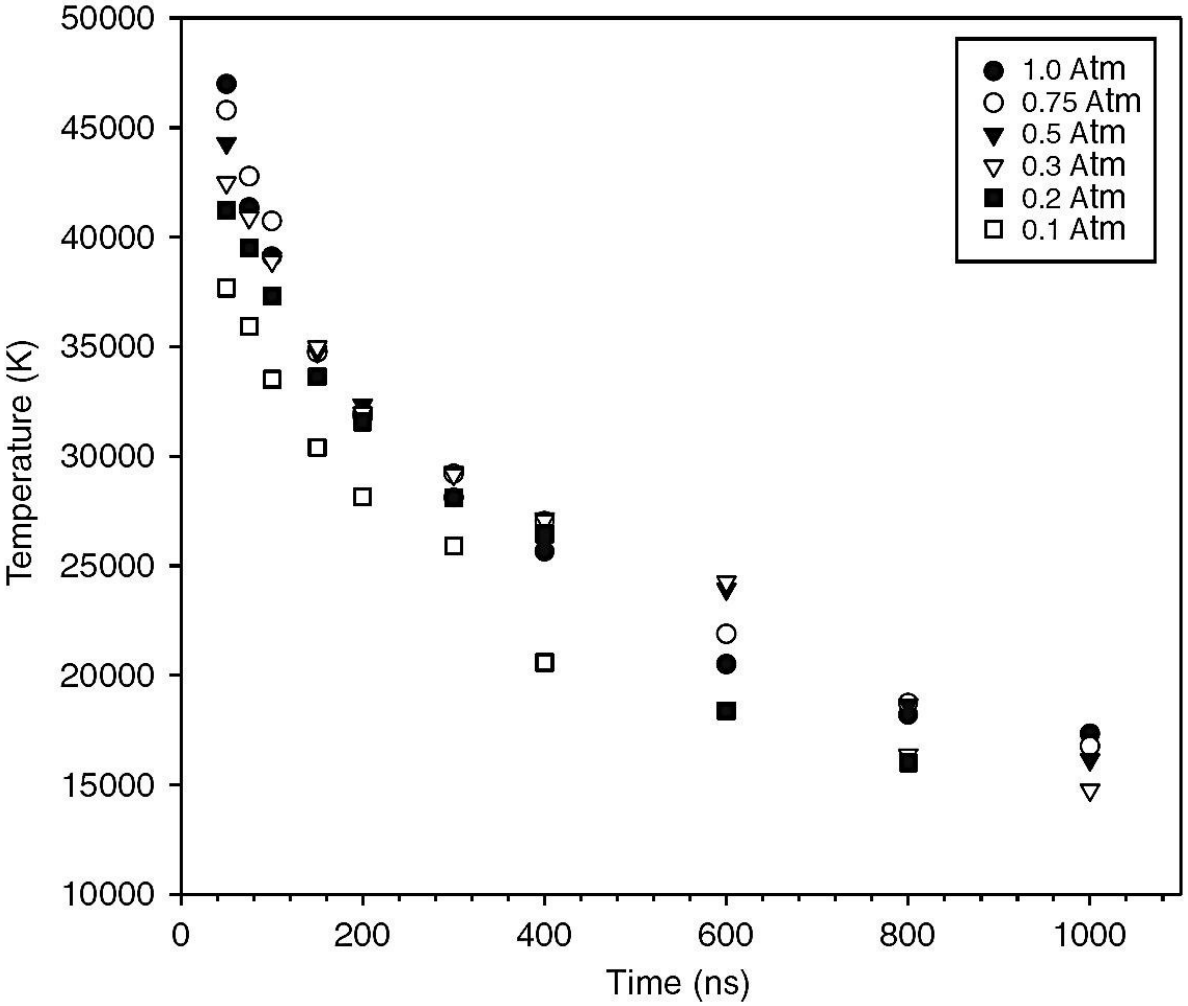

***Figure (1-12)**: Spectral fit T_e versus time after the laser pulse for six pressure cases at a fixed laser energy of 180 mJ/pulse* [62].

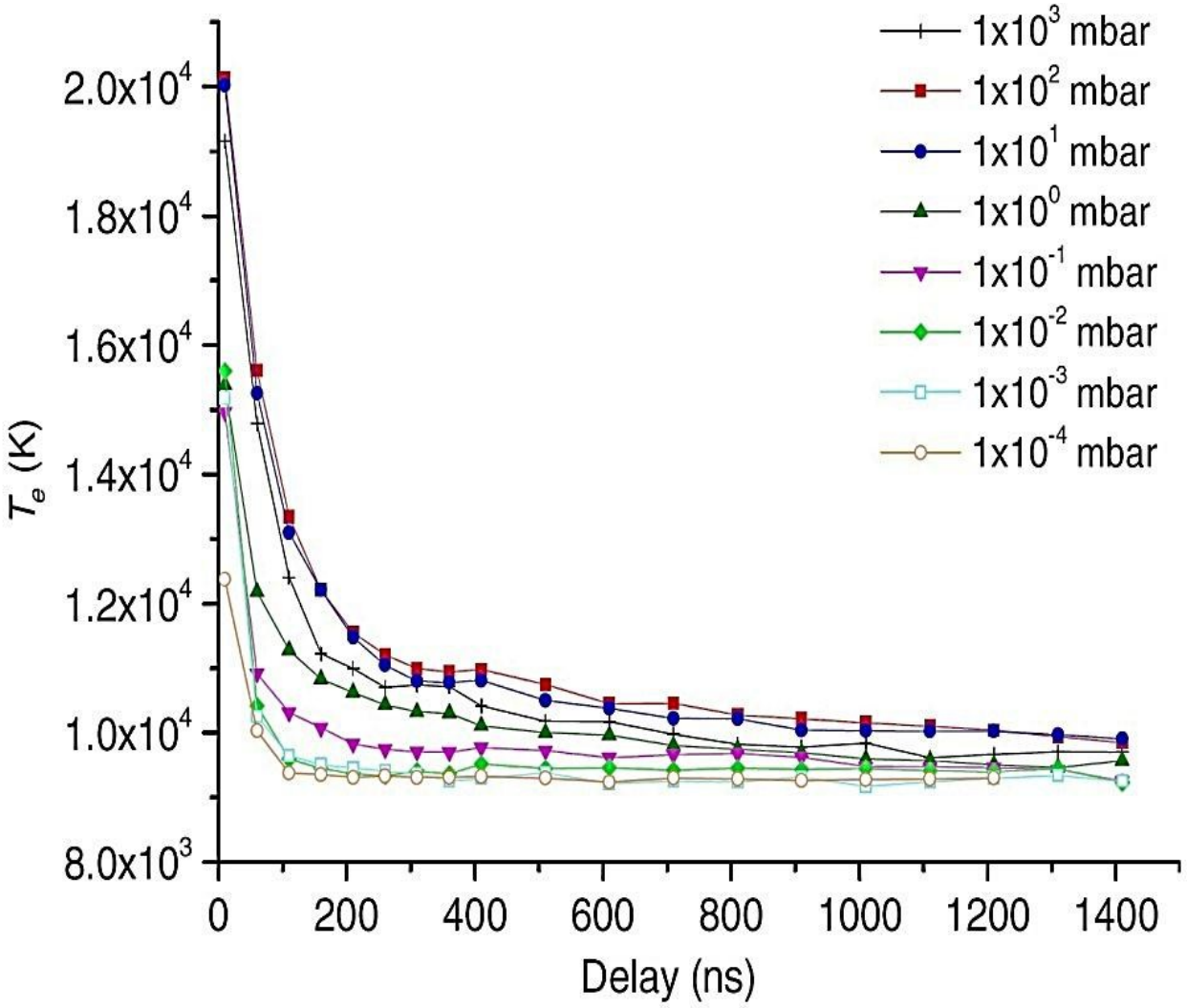

***Figure (1-13)**: Temporal evolution of T_e of Si plasma produced by Nd:YAG (532 nm) laser at ambient pressures of air varying from 10^3 to 10^{-4} mbar* [52].

Freeman *et al.* [64] have shown that the ablation of a brass target in air at atmospheric pressure leads to plasma with high n_e and T_e. The variation as a function of the pressure has identical trend whatever the laser pulse, 8 ns (at 1064 nm) or 40 fs (at 800 nm). On the other hand, Bashir *et al.* [50] used a 10 ns pulsed laser at 1064 nm to ablate cadmium in argon, air and helium of pressures ranging from 5 to 760 Torr. They found that T_e, as well as the n_e decreases with the gas pressure increase. Farid *et al.* [65] used the same laser characteristics as Bashir *et al.* [50] (10 ns at 1064 nm) to ablate a copper target in argon, air and helium at pressures ranging from 5 to 760 Torr. The authors found that T_e increases with the pressure to

reach a maximum at ~100 Torr, and then decreases to recover the low pressure value at 760 Torr. The same trends were also observed for n_e, but they were more pronounced in argon than in air and helium. Furthermore, some experimental studies reported the existence of optimum pressure range at which the plasma parameters are maximal. That range depends on the ambient gas composition and they referred these results to plasma-gas interaction [50, 66, 67]. It has been also reported that at high pressures, instabilities can appear at the plasma-gas interface especially, Rayleigh-Taylor (RT) instability (RT instability occurs when there are two fluids of different densities adjacent to each other and the lighter fluid is accelerated towards the denser fluid) [68, 69].

1.5.4 Effect of ambient gas composition

The dependence of the plasma n_e and T_e on the ambient gas composition was explored in various studies. Aguilera and Aragon [70] compared the effect of the gas composition namely, Ar, He, and air on T_e and n_e at atmospheric pressure. They found that Ar resulted in the highest T_e and n_e, He resulting in the lowest. As for the temporal evolution, as shown in Figure (1-14), Ar yields the slowest decay of both n_e and T_e, while He results in the fastest. Iida [66], as shown in Figure (1-15), reported a similar behavior. This behaviour can be explained by the properties of these gases, in particular their mass M ($M_{Ar} > M_{N_2} > M_{He}$) and their thermal conductivities $k_{thermal}$ ($k_{Ar} < k_{N_2} < k_{He}$), see Table (A-1) in appendix I. For instance, Ar produces a plasma confinement where the gas species exert a force (which depends on their mass) on the plasma species leading to more collisions and heating in the plume. In case of He, its large thermal conductivity compared to Ar and N_2 causes the plasma to cool faster through heat exchange with the He atoms and then the excitation of the plasma atoms decreases rapidly with rising pressure.

Sdorra and Niemax [71] have compared the effect of argon, neon, helium, nitrogen, and air on copper plasma at pressures below atmosphere. Figure (1-16) shows that argon produces the highest T_e and He the lowest. Plasmas produced in air and nitrogen follows the same trend, which can be due to the uncertainties in the calculation of the parameters in the methods used to determine both n_e and T_e.

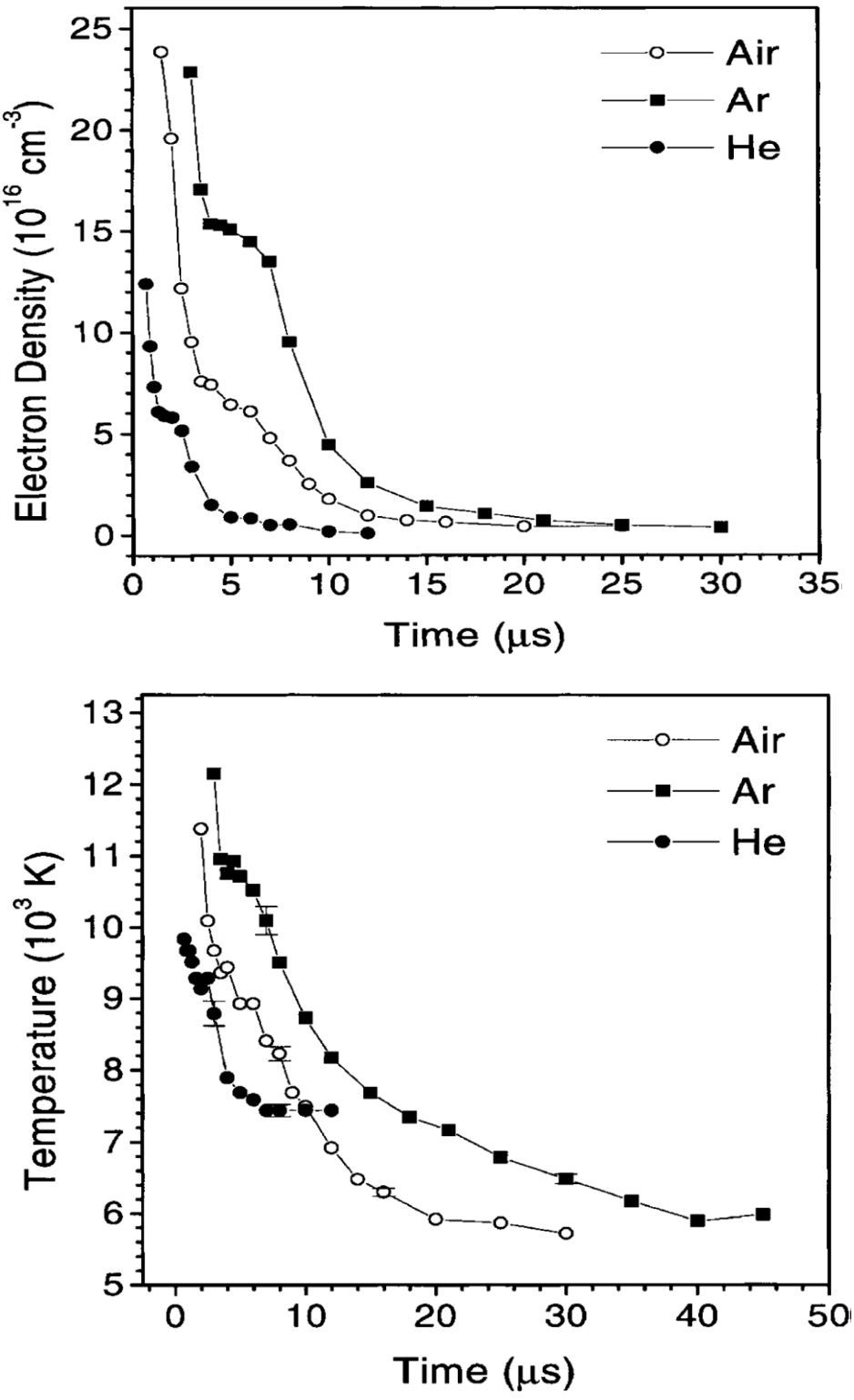

***Figure (1-14)**: Temporal evolution of T_e and n_e of laser-produced Fe plasmas generated in air, argon, and helium at atmospheric pressure* [70].

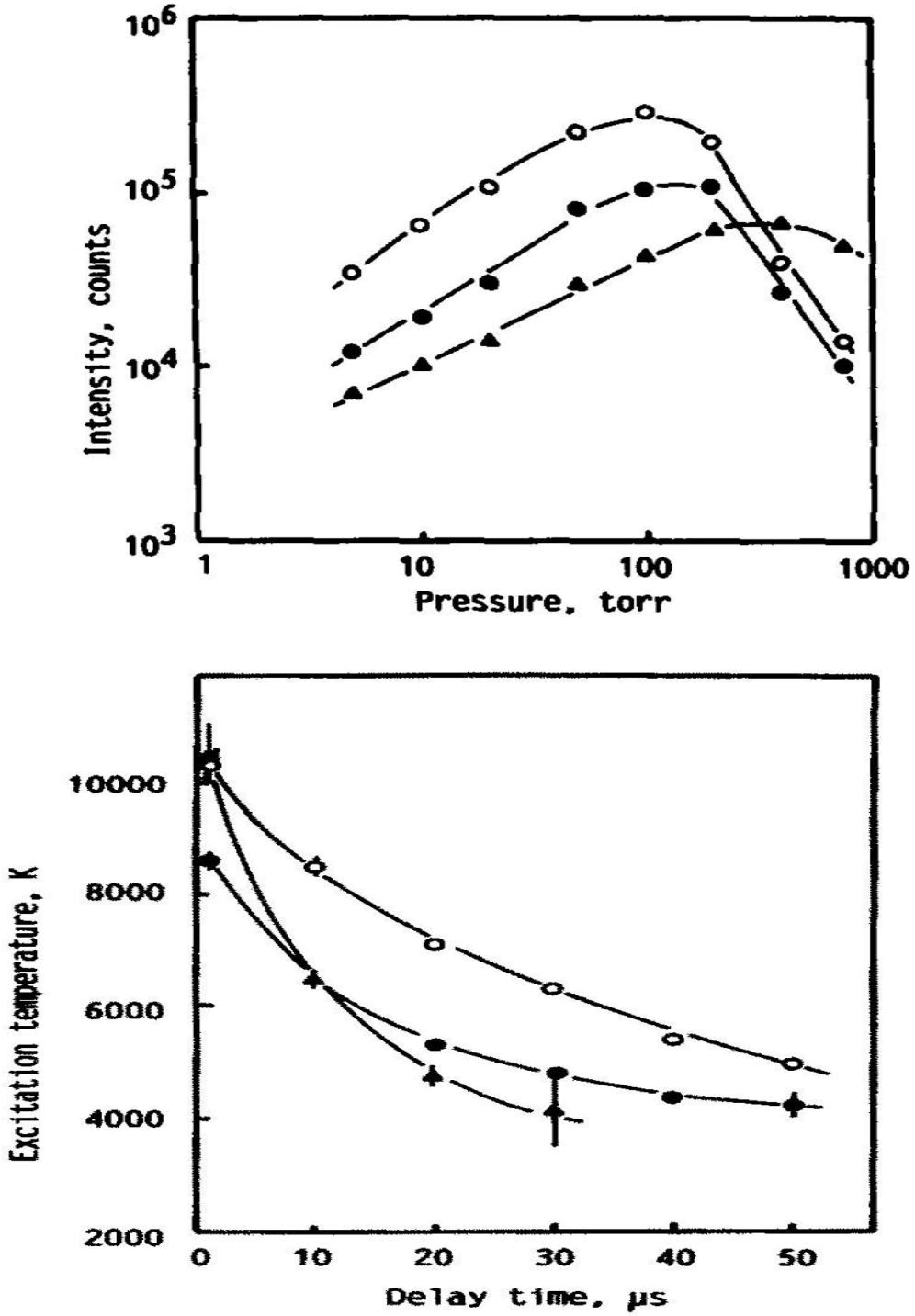

***Figure (1-15)**: Emission intensities and Time resolved T_e in the various atmospheres Ar (0), air (●) and He (Δ). The sample was a standard aluminum alloy which containing 0.97 % iron* [66].

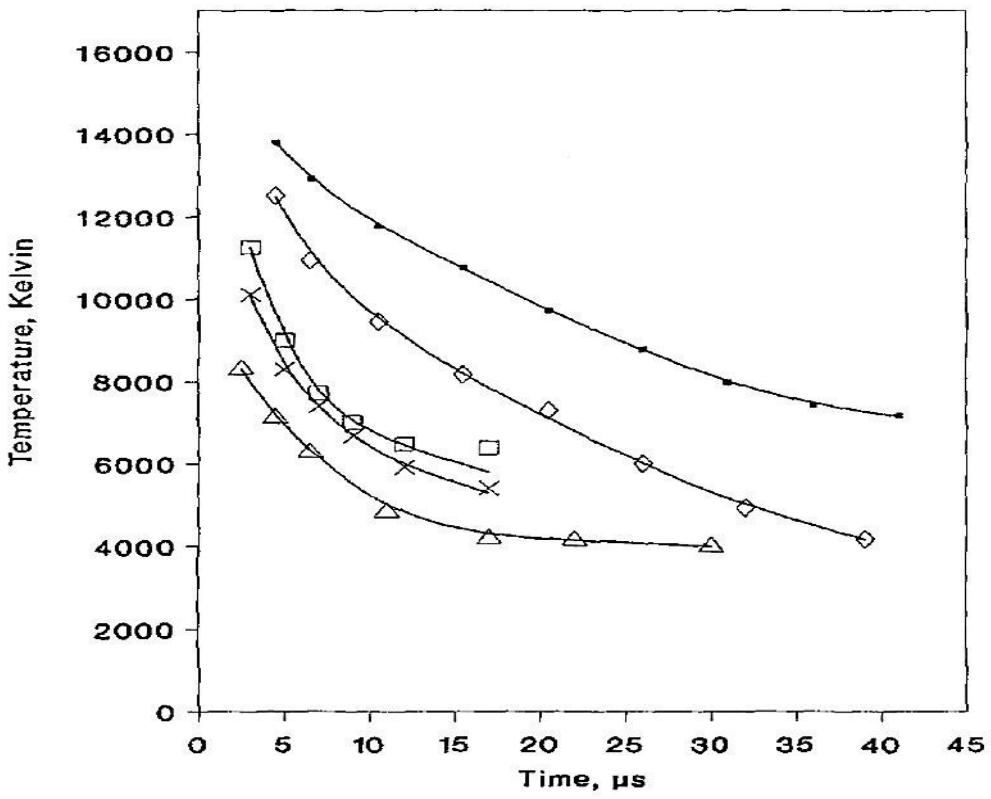

***Figure (1-16)**: T_e dependence on time measured with a copper sample in argon (●), neon (◊), air (□), nitrogen (x) and helium (Δ)* [71].

As a closing remark of this chapter, despite the enormous number of theoretical and experimental studies on laser-induced plasma, it is clear that there is a contradiction in the published results which indicates the complexity of the physical process involved in ablation and plasma formation and the sensitivity of these mechanisms on the experimental conditions. It can therefore be concluded from these various observations that there is no clear consensus on the dependence of ablation plasmas on their environment and it is still a great challenge to study its basic mechanisms and characteristics. In this context, the primary objective of the present work is to conduct a thorough investigation of the interplay between the ablated plasma plume and the ambient gas. This will be achieved by analyzing the spatial-temporal evolution as well as nanosecond characterizations of an aluminum plasma plume produced by a XeCl excimer laser (308 nm) in terms of spectral intensity, n_e, T_e and two-dimensional ICCD imaging. The experiments will be performed in various environments, extending from vacuum

(10^{-7}) to atmosphere (760 Torr), and using an ambient inert gas like Ar and He as well as chemically reactive gas like N_2. Finally, our experimental results will be compared to previous studies in order to provide a comprehensive study of the correlation between the surrounding ambient conditions and the plasma plume dynamics.

1.6 References

[1] S. B. Wen, X. L. Mao, R. Greif and R. E. Russo, *J. Appl. Phys.*, vol. 101, no. 2, p. 023115, 2007.

[2] G. C. Y. Chan, W. T. Chan, X. L. Mao and R. E. Russo, Spectrochim. Acta, Part B, vol. 56, p. 77, 2001.

[3] M. Sabsabi and P. Cielo, *Appl. Spectrosc.*, vol. 49, pp. 499-507, 1995.

[4] K.J. Grant and G.L. Paul, *Appl. Spectrosc.*, vol. 44, pp. 1349–1354, 1990.

[5] J.B. Simeonsson and A.W. Miziolek, *Appl. Opt.*, vol. 32, pp. 939–947, 1993.

[6] T. Mościcki, J. Hoffman and Z. Szymański, *Arch. Mech.*, vol. 63, no. 2, pp. 99-116, 2011.

[7] C. A. Gonzalez, J. A. Arteaga, Y. H. Gomez, J. Osorio, J. A. Jaramillo, H. Riascos, *J. Phys.: Conf. Ser.*, vol. 370, pp. 012033-1−012033-7, 2012.

[8] J. K. Antony, G. S. Jatana, N. J. Vasa, V. L. N. Sridhar Raja, A. S. Laxmiprasad, *Appl. Phys. A: Mater. Sci. Process.*, vol. 101, pp. 161-165, 2010.

[9] Y. P. Raizer, *Gas Discharge Physics*. Berlin: Springer-Verlag, 1991.

[10] F. F. Chen, *Plasma Physics*. NY: Plenum Press, 1974.

[11] J. Hermann, M. Benfarah, G. Coustillier, E. Axente, J.F. Guillemoles, M. Sentis, P.Alloncle, T. Itina, *Appl. Surf. Sci.*, vol. 252, pp. 4814–4818, 2006.

[12] A. De Giacomo, M. Dell'Aglio, R. Gaudiuso, S. Amoruso, O. De Pascale, *Spectrochimica Acta Part B*, vol. 78, pp. 1-19, 2012.

[13] L.J. Radziemski, T.R. Loree, D.A. Cremers, N.M. Hoffman, *Anal. Chem.*, vol. 55, pp. 1246–1252, 1983.

[14] Y.P. Raizer, *Laser-Induced Discharge Phenomena*. New York: Consultants Bureau, 1977.

[15] J.F.Y. Gravel and D. Boudreau, *Spectrochim. Acta, Part B*, vol. 64, pp. 56-66, 2009.

[16] B. Rethfeld, K. Sokolowski-Tinten, D. von der Linde and S. I. Anisimov, *Applied Physics A* , vol. 79, pp. 767-769, 2004.

[17] C. Aragón and J.A. Aguilera, *Spectrochimica Acta Part B*, vol. 63, pp. 893–916, 2008.

[18] S. Zhang, X. Wang,M. He, Y.Jiang, B. Zhang, W. Hang, B. Huang, *Spectrochim. Acta, Part B*, vol. 97, pp. 13-33, 2014.

[19] S. George, A. Kumar, R. K. Singh, V. P. N. Nampoori, *Appl. Phys. A*, vol. 98, pp. 901-908, 2009.

[20] J. Hermann and S. Bruneau, *Thin Solid Films*, vol. 453-454, pp. 377–382, 2004.

[21] J. Hermann, C. Boulmer-Leborgne, D. Hong, J. Appl. Phys., vol. 83, pp. 691–696, 1998.

[22] O. Samek, D.C.S. Beddows, J. Kaiser, S.V. Kukhlevsky, M. Liška, H.H. Telle, J. Young, *Opt. Eng.*, vol. 39, pp. 2248–2262, 2000.

[23] K. Kagawa, M. Ohtani, S. Yokoi, S. Nakajima, *Spectrochim. Acta Part B*, vol. 39, pp. 525–536, 1984.

[24] F.S. Ferrero, J. Manrique, M. Zwegers, J. Campos, *J. Phys. B: At. Mol. Opt. Phys.*, vol. 30, pp. 893–903, 1997.

[25] M. Corsi, G. Cristoforetti, M. Giuffrida, M. Hidalgo, S. Legnaioli, V. Palleschi, A.Salvetti, E. Tognoni, C. Vallebona, *Spectrochim. Acta Part B*, vol. 59, pp. 723–735, 2004.

[26] S. S. Harilal, B. O'Shay, M. S. Tillack, and M. V. Mathew, *J. Appl. Phys.*, vol. 98, p. 013306, 2005.

[27] H. R. Griem, *Spectral Line Broadening by Plasmas*. New York: Academic Press, 1974.

[28] N. Ben Nessib, *New Astronomy Reviews*, vol. 53, pp. 255-258, 2009.

[29] Z. Simic, M. S. Dimitrijevic, and A. Kovacevic, *New Astronomy Reviews*, vol. 53, pp. 246-251, 2009.

[30] W. L. Wiese, *in Plasma Diagnostic Techniques*, R. H. Huddlestone and S. T. Leonard, Ed. New York: Academic Press, 1965.

[31] X.Z. Zhao, L.J. Shen, T.X. Lu, K. Niemax, *Appl. Phys. B*, vol. 55, pp. 327–330, 1992.

[32] H. R. Griem, *Plasma Spectroscopy*. New York: McGraw-Hill, 1964.

[33] W. Lochte-Holtgreven, *Plasma Diagnostics*.: North Holland Publishing Company , 1968.

[34] G. Cristoforetti, A. De Giacomo, M. Dell'Aglio, S. Legnaioli, E. Tognoni, V. Palleschi, & N. Omenetto, *Spectrochim. Acta, Part B*, vol. 65, no. 1, pp. 86-95, 2010.

[35] Q.L. Ma, V. Motto-Ros, W.Q. Lei, M. Boueri, X.S. Bai, L.J. Zheng, H.P. Zeng and J. Yu, *Spectrochim. Acta, Part B*, vol. 65, pp. 896-907, 2010.

[36] S. Amoruso, R. Bruzzese, N. Spinelli and R. Velotta, *J. Phys. B: At. Mol. Opt. Phys.*, vol. 32, pp. R131–R172, 1999.

[37] H.C. Liu, X.L.Mao, J.H. Yoo and R.E. Russo, *Spectrochim. Acta, Part B*, vol. 54, pp. 1607–24, 1999.

[38] G. J. Bastiaans and R.A. Mangold, *Spectrochim. Acta, Part B*, vol. 40, pp. 885-92, 1985.

[39] A. Sola, M. D. Calzada, & A. Gamero, *Journal of Physics D: Applied Physics*, vol. 28, no. 6, p. 1099, 1995.

[40] E. Tognoni, V. Palleschi , M. Corsi and G. Cristoforetti, *Spectrochim. Acta, Part B*, vol. 57, pp. 1115–30, 2002.

[41] D. A. Cremers and L. J. Radziemski, *Handbook of Laser-Induced Breakdown Spectroscopy*. Chichester: Wiley, 2006.

[42] Y. Lee, K. Song and J. Sneddon, *Laser induced plasmas for analytical spectroscopy Lasers Analytical Atomic Spectroscopy*, J. Sneddon *et al*, Ed. New York: VCH, 1997.

[43] J.M. Vadillo, C.C. Garcia, S. Palanco , J. Ruiz and J.J. Laserna, *Spectrochim. Acta, Part B*, vol. 56, pp. 923–31, 2001.

[44] J.S. Cowpe, J.S. Astin, R.D. Pilkington and A.E. Hill, *Spectrochim. Acta, Part B*, vol. 62, pp. 1335–42, 2007.

[45] F. Garrelie and A. Catherinot, *Appl. Surf. Sci.*, vol. 139, pp. 97-101, 1999.

[46] J. Andrew, J. R. Effenberger, and Jill R. Scott, *sensors*, vol. 10, pp. 4907-4925, 2010.

[47] J.S. Cowpe, J.S. Astin, R.D. Pilkington, A.E. Hill, in *4th Euro Mediterranean Symposium on Laser Induced Breakdown Spectroscopy*, Paris, France, September 11-13, 2007, pp. 1066-1071.

[48] C.B. Dreyer, G.S. Mungas, P. Thanh, J.G. Radziszewski, *Spectrochim. Acta, Part B*, vol. 62, pp. 1448-1459, 2007.

[49] S. Yalcın, Y. Y. Tsui and R. Fedosejevs, *J. Anal. At. Spectrom.*, vol. 19, pp. 1295 – 1301, 2004.

[50] S. Bashir, N. Farid, K. Mahmood and M.S. Rafique, *Applied Physics A*, vol. 107, no. 1, pp. 203–212, 2012.

[51] Yong-III Lee and J. Sneddon, *Spectroscopy Letters*, vol. 29, no. 6, pp. 1157-71, 1996.

[52] J.S. Cowpe, R.D. Pilkington, J.S. Astin and A.E. Hill, *J. Phys. D: Appl. Phys.*, vol. 42, p. 165202, 2009.

[53] M. Milan and J.J. Laserna, *Spectrochim. Acta, Part B*, vol. 56, pp. 275–88, 2001.

[54] H.C. Liu, X.L. Mao, J.H. Yoo, R.E. Russo, *Spectrochim. Acta Part B*, vol. 54, pp. 1607–1624, 1999.

[55] N.M. Shaikh, B. Rashid, S. Hafeez, Y. Jamil and M.A. Baig, *J. Phys. D: Appl. Phys.*, vol. 39, pp. 1384–91, 2006.

[56] B. Le Drogoff, J. Margot, M. Chaker, M. Sabsabi, O. Barthélemy, T.W. Johnston, S. Laville, F. Vidal, Y. von Kaenel, *Spectrochim. Acta, Part B*, vol. 56, pp. 987–1002, 2001.

[57] M. Shaikh, Sarwat Hafeez, M. A. Kalyar, R. Ali, and M. A. Baig Nek, *J. Appl. Phys.*, vol. 104, p. 103108, 2008.

[58] G. Abdellatif, H. Imam, and Y. Gamal, *J. Korean Phys. Soc.*, vol. 56, no. 1, pp. 300-308, 2010.

[59] G. Cristoforetti, S. Legnaioli, V. Palleschi, A. Salvetti and E. Tognoni, *Spectrochim. Acta, Part B*, vol. 59, pp. 1907-17, 2004.

[60] G. A. Hebner, C. B. Fleddermann and P. A. Miller Hebner, *J. Vac. Sci. Technol. A*, vol. 15, no. 5, p. 2698, 1997.

[61] Y.I. Lee, K. Song, H.K.Cha, J.M. Lee, M.C. Park, G.H. Lee, J. Sneddon, *Appl. Spectrosc.*, vol. 51, pp. 959-964, 1997.

[62] N.Glumac and G.Elliott, *optics and lasers in engineering*, vol. 45, pp. 27-35, 2007.

[63] N. Glumac, G. Elliott and M. Boguszko, "AIAA J.," vol. 43, pp. 1984–94, 2005.

[64] J.R. Freeman, S.S. Harilal, P.K. Diwakar, B. Verhoff and A. Hassanein, *Spectrochim. Acta, Part B*, vol. 87, pp. 43–50, 2013.

[65] N. Farid, S. Bashir and K. Mahmood, *Physica Scripta*, vol. 85, no. 1, p. 015702, 2012.

[66] Y. Iida, *Spectrochim. Acta B*, vol. 45, p. 1353, 1990.

[67] G. Asimellis, S. Hamilton, A. Giannoudakos and M. Kompitsas, *Spectrochim. Acta, Part B*, vol. 60, p. 1132, 2005.

[68] S.S. Harilal, C.V. Bindhu, M.S. Tillack, F. Najmabadi and A.C. Gaeris, *J. Appl. Phys.*, vol. 93, no. 5, pp. 2380–2388, 2003.

[69] A.K. Sharma and R.K. Thareja, *Appl. Surf. Sci.*, vol. 243, no. 1, pp. 68–75, 2005.

[70] J.A. Aguilera and C. Aragón, *Appl. Phys. A*, vol. 69, pp. S475–S478, 1999.

[71] W. Sdorra and k. Niemax, *Mikrochim. Acta*, vol. 107, pp. 319-327, 1992.

CHAPTER 2:

Experimental setup, diagnostic descriptions, and spectroscopic techniques

Chapter 2:
Experimental Setup, Diagnostic Descriptions, and Spectroscopic Techniques

2.1 Introduction

The experimental setup consists of a pulsed laser, a delay generator, a spectrometer, and an ICCD camera. The plasma is produced in a chamber equipped with a quartz window enabling us to control of the local environment of the ablation plume, such as the ambient gas composition and pressure around the target. The target is mounted on a motorized sample holder that is continuously translated and rotated across the laser beam. This movement of the target produces a fresh surface exposed to the laser beam with successive shots, and it helps to maintain the spatial homogeneity of the plasma plume. The schematic diagram of the experimental setup is shown in Figure (2-1).

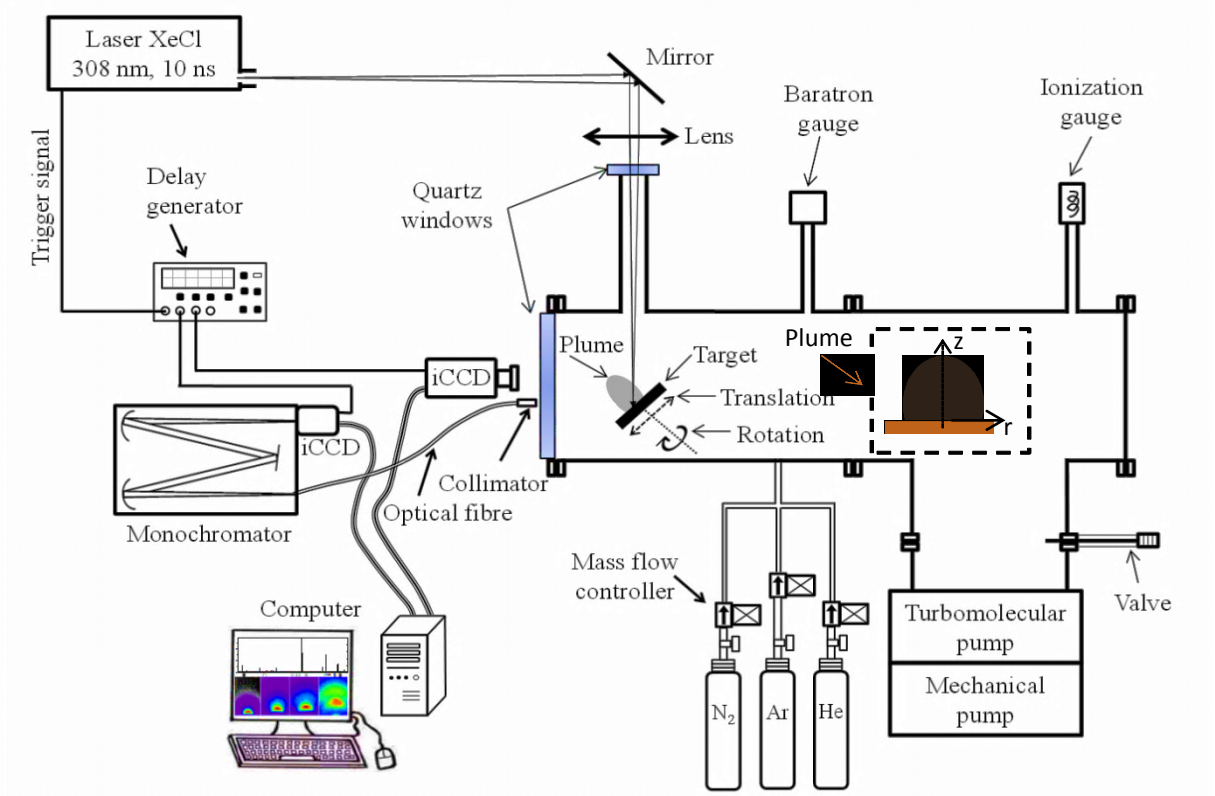

***Figure (2-1)**: Schematic drawing of the experimental arrangement.*

2.2 Pulsed Laser

The plasma is created from an aluminum target by a XeCl excimer laser of pulse duration τ = 10 ns, operating at the wavelength λ = 308 nm with a repetition rate of 10 Hz. The laser energy per pulse is set at 250 mJ for the entire experiment. The laser beam is focused at 45^{o} to the Al target surface by a quartz lens (f = 110 cm). By inspection of the crater on the target surface caused by the laser pulse, we estimate the spot area to be ~0.4 mm^2 so the fluence on the target is ~50 J/cm^2.

2.3 Target and Manipulator

We used doped aluminum targets, one containing 0.1% magnesium impurities for spectral and n_e measurements, and the other 0.65% Fe for excitation temperature measurements. Both targets had diameter and thickness of 58 and 15 mm, respectively. The target was mounted on a motorized sample holder which was continuously translated horizontally and vertically with velocities of 0.6 and 2.9 mm s^{-1}, respectively. This motion enables us to generate the plume from different spots of the target surface material and therefore to maintain the spatial homogeneity of the plasma plume. A fresh target surface is continuously translated and rotated across the laser beam by allowing the target to rotate with an angle ~45º between the laser beam and the target normal and keeping it unchanging during the whole of the experiments.

2.4 Spectrograph, ICCD camera and data acquisition

The spectrum emitted from the plume was collected by an optical fibre of 1 mm diameter for the temporal measurements and of 0.2 mm rectangular slit for the spatial measurements. The optical fibre is connected to the entrance slit of a Jobin-Yvon Triax 550 with a focal length of 55 cm; entrance slit width of 10 μm, equipped with an ultraviolet-blazed grating of 3600 grooves/mm. The spectra is acquired by an intensified charge-coupled device (ICCD) detector from Andor Technology (520-18F-01, 1024×256 pixels), equipped with a macro lens (90 mm, F/2.5) and it is cooled at -10 ^{o}C by Peltier effect. Using a delay generator (Quantum composers plus model 9518^{+}) to synchronize the whole system, a laser shot is used

to trigger the delay generator, which subsequently controls the delay time and exposure time of the spectrometer and ICCD camera system, by means of an electrical signal.

The data acquisition and recordings are performed by Andor Solis software v. 4.10.3 which enables us to control the various parameters of both spectrometer and ICCD camera. The acquisition mode used is full vertical binning, which adds the photon count for each pixel in a column and plots it as a photon count per horizontal pixel number (wavelength) in arbitrary units. By varying the delay time and exposure time of the ICCD camera, we are able to perform high resolution temporal measurements by time-gating the plume light emission with spectral resolution of 0.015 nm at 281.6 nm. The ICCD camera delay time and exposure time diagram and values are shown in Figure (2-2) and table [2-1]. Spatial resolution of 1 mm in both axial and radial directions is obtained by using an optical fibre, collimator and a movable stand system depicted in Figure (2-3).

It is worth mentioning that the energy delivered by the laser fluctuates from one shot to another, which affects the ablated plasma properties such as temperature, density, intensity of spectral lines. To overcome the energy fluctuations and therefore improve the signal-to-noise ratio, each spectrum is recorded by accumulating spectra from 100 laser shots using the same gating parameters. The number of laser shots is optimized by ensuring that the signal did not change any more with time taking into account the impeding of the creation of deep craters into the target under the laser impact.

We may summarize the process of collecting plume spectra and data acquisition as follows: 1) Set the delay time to a certain value (50 ns to 40 μs). 2) Set the gate width and exposure time, to a comparable value (50 ns to 5 μs). 3) Ablate the target with 100 laser pulses. 4) Capture plume spectra. 5) Obtain a fresh surface of the target by rotating the target with the manipulator. 6) Increment the delay time. 7) Repeat steps 3-6 until the end of data collection.

Plume imaging is captured directly by the ICCD camera by varying the delay and gate times so we were able to temporally resolve two-dimensional nanosecond ICCD photographs of the transient plasma. Photographs are taken “side view”, i.e., the ICCD camera positioned in a plane perpendicular to the plume propagation. A time resolution of 10 ns is obtained by triggering the ICCD intensifier by using the delay generator synchronized on the laser output

trigger. The experiments were carried out in Ar, N_2 and He atmosphere at pressure ranging from 10^{-7} to 760 Torr.

Finally, this process can be described as follows: 1) Set the gate width to 10 ns. 2) Set the time delay to the initial value. 3) Trigger the system by a laser shot. 4) Capture the image. 5) Obtain a fresh surface area of the target. 6) Increment the delay time. 7) Repeat steps 4-6 as wanted.

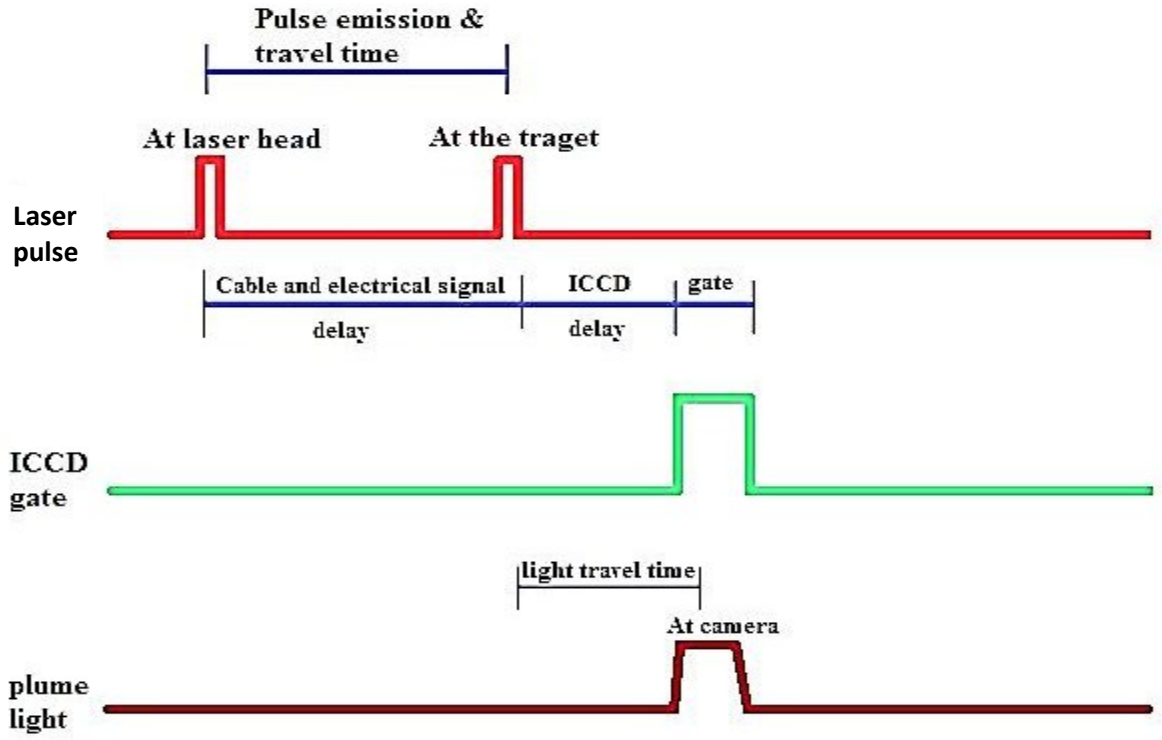

***Figure (2-2)**: ICCD camera delay and integration times diagram.*

***Table (2-1)**: ICCD camera delay and integration time values.*

Al II and Mg lines		**Fe I lines**	
Delay time (τd) (μs)	Integration time (τ_i) (μs)	Delay time (τ_d) (μs)	Integration time (τ_i) (μs)
[0,1]	0.05	[0,1]	0.1
[1,2]	0.1	[1,5]	0.2
[2,5]	0.2	[5,10]	0.5
[5,15]	0.5	[10,30]	1
15 and more	1	30 and more	5

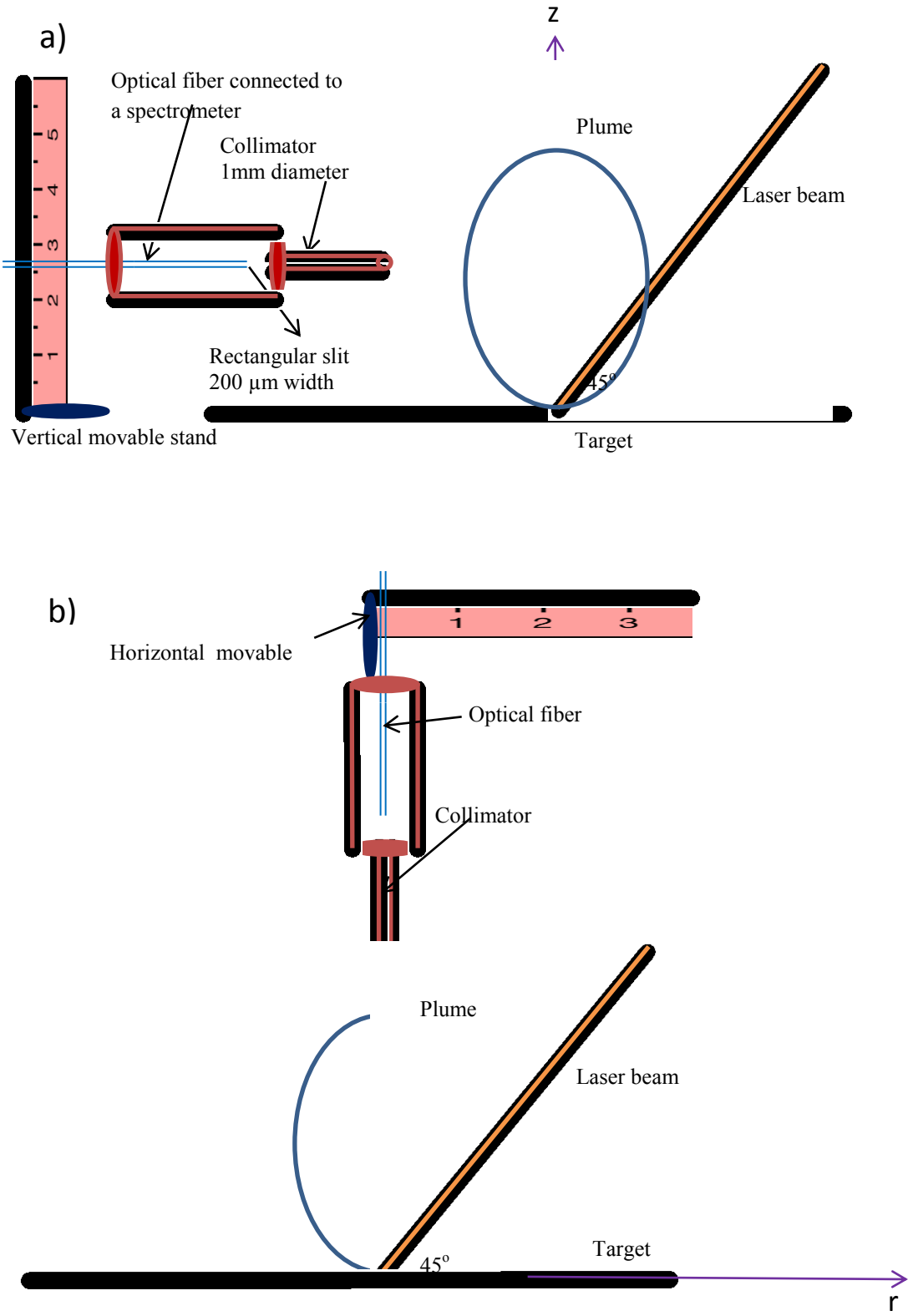

***Figure (2-3)**: Schematic drawing of the spatial experimental arrangement in the direction a) axial b) radial.*

2.5 Target chamber

The chamber is cylindrically shaped with six ports as shown in Figure (2-1). One port is equipped with a 25 cm quartz window for collecting and imaging the plasma plume emission. Another port is capped with a 3.5 cm quartz window for radial measurements. A third port allows the laser pulse to enter the chamber through a cylindrical tube of length 1 meter. On the opposite side, the fourth port is used for target motion by the manipulator. Finally, the last two ports are used to control the pumping system, is mounted on a cart occupied with both mechanical and high-speed turbomolecular pumps, so the plume can be generated in high vacuum or at the required pressure. The chamber is mounted on a table, which facilities, laser alignment along the axis of the cylindrical chamber.

With the aim of studying the effect of ambient atmosphere on the aluminum laser - induced plasma, the target is placed in the chamber evacuated to a residual pressure of 5x 10^{-7} Torr. Gases, namely Ar, He and N_2 (purity of 99.998%) are introduced into the chamber by means of MKS Mass-Flow controllers with a maximum flow limit of 100 sccm (Standard Cubic Centimeters per Minute). After the introduction of the gas, the pressure in the chamber is measured by means of two Baratron gauges from MKS instruments (ranges of 0-2 and 0-100 Torr). The gas pressures could be adjusted to cover the range from vacuum (5x10^{-7}) to atmospheric (760 Torr).

2.6 Electron density measurements

Stark broadening was used to determine the evolution of plasma density after delays varying from 50 ns to 10 µs. As mentioned in chapter 1, line broadening usually results from a combination of factors that include natural broadening, Doppler broadening, pressure broadening and Stark broadening. A supplementary factor is usually added, and it involves due to the instrument.

Natural broadening has origin from the uncertainty of the energy levels (Heisenberg uncertainty principle) and it is usually neglected compared to other mechanisms. Doppler broadening is related to the thermal movement of the emitted species in the plasma and a simple relation [1] given by $\Delta\nu_D = 7.16\ 10^{-7}\lambda\sqrt{T_e(K)/M(amu)}$ where M is the mass of the emitting species, has been derived to compute its contribution. Pressure broadening results

from two components: resonance and van der Waals broadenings. Stark broadening is due to the interaction of the emitting species with the surrounding charged species (electrons and ions) through the dynamic micro-electric field created by these species. For optically thin plasma, the total line intensity can therefore be described by the convolution of these line shapes and can be fitted with a Voigt profile.

In our experimental conditions, instrumental broadening is reduced by minimizing the slit width of the spectrometer. This broadening is described by a Gaussian profile with a FWHM assumed to be 0.039 nm from the acquisition of a low pressure lamp spectrum. On the other hand, the effect of Doppler broadening is expected to be relatively small, so that Stark broadening should be the dominant broadening mechanism [2]. Stark broadening is determined by fitting each transition peak of interest AlII 281.6 nm ($3s4s\ ^1S_0 \rightarrow 3s3p\ ^1P_1$), Mg II 279.55 ($2P^6\ 3S\ ^2S_{1/2} \rightarrow 2P^6\ 3P\ ^1P^0_{3/2}$) and AlI 394 nm ($4s\ ^2S_{1/2} \rightarrow 3P\ ^2P_{1/2}$) by a Voigt profile and removing the contribution of the instrumental broadening.

Figure (2-4) represents the profile shape of the Al II emission line at 281.6 nm ($3s4s\ ^1S_0 \rightarrow 3s3p\ ^1P_1$) acquired in argon (Figure 2-4a) and in helium (Figure 2-4b) ambient gases. These profiles are fitted by a Voigt profile, and then we deduce the FWHM of the Lorentzian contribution. It is found to be ~0.29 and 0.22 nm in Ar and He ambient gas, respectively. The Lorentzian FWHM acquired in N_2 is found to be higher than that in He and lower than that in Ar.

Finally, in our case, the Stark effect results mostly from collisions of the charged particles [3]. Therefore, n_e, can be calculated from the relation [4,5]:

$$n_e \approx \frac{1}{2\omega}(\Delta\lambda_{\frac{1}{2}} 10^{16}), \qquad (2-1)$$

The spectral parameters used in equation (2-1) are presented in Table (2-2).

Experimental evidence indicates that the uncertainty in the theoretical calculations of the Stark broadening parameter w results in a 15% error on n_e [6]. In addition, in the present work the statistical error in fitting the Voigt profile of the lines results in about 2-5% error on the n_e. Therefore, the maximum total error in the n_e determination is about 20%. Note that due to the presence of an important continuum from 50 ns to 1 μs, the Stark width measured for the Al ion lines has a higher uncertainty than for the neutral lines that are considered for delays larger than 1 μs.

By this manner, n_e has deduced and studied for different ambient gases and pressures at different delay times after the laser shots, and in the axial (perpendicular to the target) and radial (parallel to the target) positions: z and r.

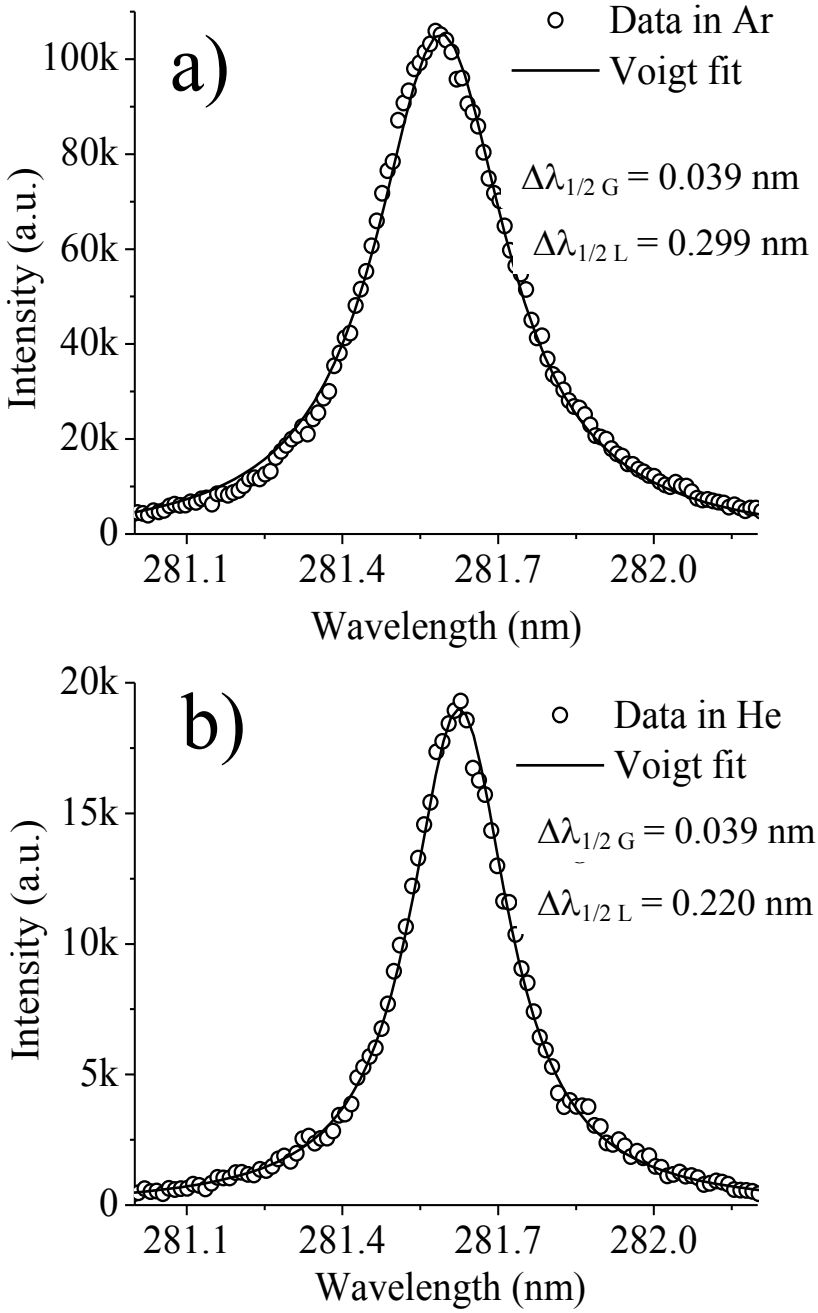

Figure (2-4): *The emission line profile of aluminum ion Al II at 281.6 nm in a) argon and b) helium background gases.*

***Table (2-2)**: Spectral data for the transitions of Al II, Mg II and Al I.*

λ (nm)	E_m(eV)	E_n(eV)	A_{mn} ($10^8 s^{-1}$)	ΔA(%)	g_m
Al II 281.62	17.81	7.41	3.83	25	1
MgII 279.55	12.08	7.65	2.60	25	4
Al I 394.40	3.14	0.00	4.93	24	1

2.7 Excitation temperature measurements

For the determination of T_e, assuming local thermodynamic equilibrium (LTE) in the plasma, the Boltzmann plot is the most widely used method. It consists in plotting the spectral line intensities of the plasmas as a function of the energy level. The relative line intensities obey the relation [1,5]:

$$\ln\left(\frac{I_{mn}\lambda_{mn}}{g_m A_{mn}}\right) = -\frac{E_m}{KT_e} + \ln\left(\frac{N(T)}{U(T)}\right), \qquad (2-2)$$

where I_{mn}, λ_{mn} and A_{mn} are respectively the intensity, the wavelength and the probability of the transition from the upper level m to the lower level n. g_m and E_m are the statistical weight and the energy of the upper level m, respectively. $U(T)$, $N(T)$, K, and T_e are the partition function, total number density, Boltzmann constant and T_e, respectively. Values of λ_{mn}, A_{mn}, g_m and E_m have been taken from the NIST database. T_e can thus be expressed as the linear slope of $ln\ (I_{mn}\ \lambda_{mn}/g_m A_{mn})$ *vs* E_m plot.

In this study, we use the emission of eight iron (Fe I) lines of plasma produced from an Al alloy containing 0.65% Fe in the spectral region (from 371.5 to 376.5 nm). Indeed, it was chosen because the emitted lines of Fe I cover a large energy range to make a Boltzmann plot. The density of Fe atoms in the discharge is low (compared with the density of Al atoms) which leads to a well-defined line profile (no self-absorption – optically thin plasma). We present in Figure (2-5a) an example of the iron lines emitted by the plasma, the lines used for the Boltzmann plot being indicated by arrows. An example of the Boltzmann plot is presented in Figure (2-5b). All the spectroscopic parameters used in the calculations were taken from the NIST database [7] see Table (2-3).

Finally, the uncertainty in the T_e determination, including transition probabilities, integrated intensities of spectral lines and the least-square errors in the slope of the Boltzmann plot is estimated to be 5% to 10%.

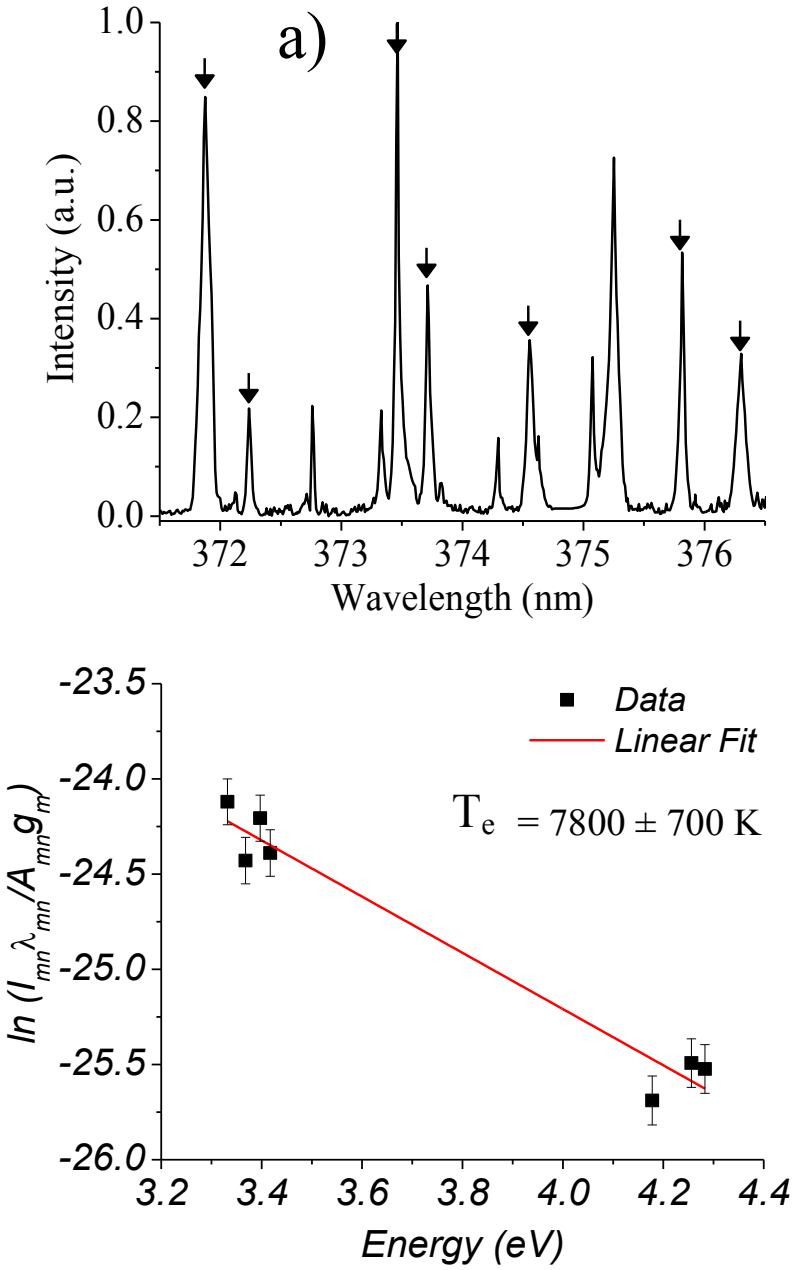

***Figure (2-5)**: a) Spectrum of Fe I lines observed in the plasma and used to make a Boltzmann plot presented in b).*

***Table (2-3)**: Spectral data for the transitions of Fe I.*

λ (nm)	E_m (eV)	E_n (eV)	A_{mn} ($10^8 s^{-1}$)	ΔA (%)	g_m
371.99	3.39	0	1.62	10	11
372.26	3.42	0.09	0.0497	10	5
373.49	4.18	0.86	0.902	10	11
373.71	3.37	0.05	0.142	10	9
374.56	3.40	0.09	0.115	10	7
375.82	4.26	0.96	0.634	10	7
376.38	4.28	0.99	0.544	10	5
376.55	6.53	3.24	0.980	25	15

2.8 Aluminum ion dynamics: Time-Of-Flight

The spectral line emission intensity I_{ij} is related to the excited state population n_{ij} by the equation:

$$I_{ij} \approx \frac{A_{ij} n_{ij} hc}{\lambda_{ij}} = \frac{A_{ij} n_i g_j hc}{U(T)\lambda_{ij}} \, exp[\frac{-E_j}{KT_e}] \qquad (2-3)$$

where A_{ij} is the spontaneous transition probability; λ_{ij}, the transition wavelength; n_i, the total density of the emitting species (ions or neutrals); g_j, the statistical weight of the transition's upper level; E_j, the excitation energy;

Since the line intensity is proportional to the localized ion density, Time-Of-Flight technique provides a useful means of tracking bulk mass motion within the plasma and thus hydrodynamic expansion. This technique depends on tracing the time evolution of a spectral emission line at sequential spatial positions along the propagation axis.

We limit the data processing to follow the temporal evolution of the maximum intensity of the line emission of Al ions at successive axial positions (4, 8 and 10 mm) from the target surface and along the propagation axis. Whatever the axial position from the target, the emission intensity of this transition reaches a maximum in time and the values reported are normalized to unity. One can deduce the most probable expansion velocity of Al ions in the

plasma plume by measuring the time separating the maximum emission intensity at different axial positions.

The emitted radiation of Al II species at 281.6 nm ($3s4s\ ^1S_0 \rightarrow 3s3p\ ^1P_1$) is chosen to be followed in time due to several reasons. First, the Al ion ejected from the target can be used as a probe for the ionization front's propagation. Second, the line profile of this transition is well defined (no superposition with any other line). Moreover, it has a high lower energy level (E_n= 7.4 eV) and it has a small transition probability ($3.8\times10^8\ s^{-1}$) [7], which strongly lowers the possibility of self-absorption in the profile [9]. The Time-Of-Flight of the atomic emission line Al I at 394.4 nm is neglected because it possesses an additional delay due to three-body recombination, as explained by De Giacomo [10] and Imam *et al.* [11].

An example of the temporal evolution of the normalized intensity of Al II emission in vacuum, at 281.6 nm at 4,8 and 10 mm from the target surface, is presented in Figure (2-6). The mean velocity of the Al^+ ions can be estimated using the aforementioned method at 4 mm the emission intensity is maximal at 90 ns which gives a velocity of ~4.4×10^6 cm s^{-1}.

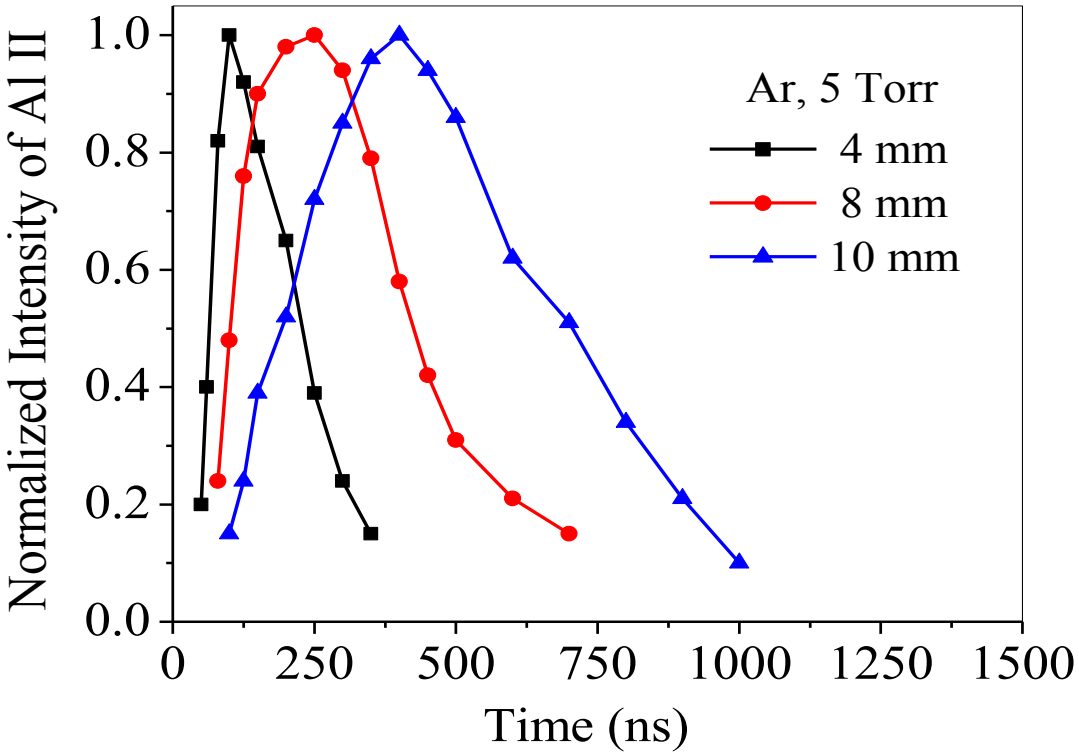

***Figure (2-6)**: Temporal evolution of the normalized intensity of Al II emission (at 281.6 nm) in vacuum at distances of 4, 8 and 10 mm from the target surface in the axial direction.*

2.9 References

[1] H.R. Griem, Plasma spectroscopy, New York: McGraw-Hill, 1964.

[2] W. L. Wiese, in Plasma Diagnostic Techniques, edited by R. H. Huddlestone and S. T. Leonard (Academic Press, New York), 1965.

[3] J. P. Singh, and S. N. Thakur, eds. Laser-induced breakdown spectroscopy. Elsevier, 2007.

[4] N. Konjević, A. Lesage, J.R. Fuhr and W.L. Wiese, J. Phys. Chem. Ref. Data, 31(3), 819–927, 2002.

[5] S.S. Harilal, B. O'Shay, M.S. Tillack and M.V. Mathew, J. Appl. Phys. 98 013306, 2005.

[6] B. Le Drogoff, J. Margot, M. Chaker, M. Sabsabi, O. Barthélemy, T.W. Johnston, S. Laville, F. Vidal, Y. von Kaenel, *Spectrochim. Acta, Part B*, 56, 987–1002, 2001.

[7] National Institute of Standards and Technology, available on line at: http://physics.nist.gov/PhysRefData/ASD/lines_form.html.

[8] G. Abdellatif, H. Imam and Y. Gamal, J. Korean Phys. Soc., 56(1), 300–308, 2010.

[9] S.S. Harilal, C.V. Bindhu, M.S. Tillack, F. Najmabadi and A.C. Gaeris, J. Phy. D Appl. Phys. 35(22), 2935, 2002.

[10] A. De Giacomo, *Spectrochim. Acta, Part B*, 58, 71–83, 2003.

[11] H. Imam, G. Abdellatif, V. Palleschi, M.A. Harith and Y. E-El. Gamal, MTPR-06 AIP.

CHAPTER 3:

Effect of ambient gas pressure and nature on the temporal evolution of aluminum laser induced plasmas

Chapter 3:

Effect of ambient gas pressure and nature on the temporal evolution of aluminum laser-induced plasmas[1]

3. 1 Introduction

In order to better understand the evolution of a laser-produced plume plasma, it is necessary to investigate the characteristics of its different parameters such as emission spectra, n_e and T_e. In this context, time-resolved optical emission spectroscopy, a non-intrusive diagnostic method, is applied to analyze aluminum laser-induced plasma plume produced in Ar, N_2 and He at different pressures. Our studies in this chapter concentrated on the temporal behavior of the emissions of atomic and ionized Al and Fe lines in the emission region AlII 281.6 nm ($4s\ ^1S_0 \rightarrow 3P\ ^1P_1$), AlI 394.4 nm ($4s\ ^2S_{1/2} \rightarrow 3P\ ^2P_{1/2}$) and Fe I from 344.1nm to 407.17nm. Stark broadening is used to determine the temporal behavior of plasma density with delays varying from 50 ns to 10 μs. For the determination of the excitation temperature, assuming (LTE) in the plasma, the Boltzmann plot is used within a time delay range from 100 ns to 40 μs. Experimental measurements suggest that the time-resolved emission spectroscopy is found to be strongly affected by the plume confinement that differs with the nature of the ambient gas and its pressure. Our observations show that both n_e and T_e increase with the ambient gas pressure. In addition, Ar is found to produce the highest plasma density and temperature and He the lowest, while N_2 yields intermediate values.

[1] This chapter is part of an article: M.S. Dawood and J. Margot, AIP Advances 4, 037111 (2014).

3. 2 Temporal dependence of plasma emission on gas pressure and nature

Plasma emission intensity, which is basically the fingerprint of the plasma's physical state, is affected by the ambient gas pressure and composition in an extremely complex manner [1]. In order to better understand the relation between the Al plasma emission intensity and the ambient gas condition, emission spectra were recorded in the wavelength regions close to the ion Al II line at λ=281.6 nm and to the neutral Al I line at λ=394 nm as a function of both the delay after laser shot and the ambient gas pressure in Ar, He and N_2.

Within the first few nanoseconds, the plasma begins a rapid growth, produces an extremely energetic cloud of electrons and ions. At that time, the emission is dominated by the background continuum (Bremsstrahlung radiation) resulting from free-free electron–ion collisions in that hot and dense plasma. Although the continuum background is very intense, the ion lines can still be detected. At this moment, the ambient gas pressure and its nature have only little effect on the plume characteristics.

As seen in Figure (3-1), after about 100 ns, the continuum emission has sufficiently decreased to make the Al II (281.6nm), Mg II (279.55nm) and Mg II (280.7nm) lines well defined so that accurate intensity measurements can then be performed. During this stage, the gas pressure and type begin to affect the shape, size and the properties of the plasma.

Beyond 1 μs, the ion lines vanish. This is due to recombination of electrons and ions. Only the atomic line of Al I can still be observed. As the recombination process lasts for tens of microseconds, and the number of neutral atoms continues to increase in the plasma volume so that the spectral lines corresponding to these neutral atoms can still be detected.

As plasma energy continues to decay, the atomic lines progressively disappear until tens of microseconds, their intensity decreasing with time. The plasma completely extinguishes when no more emission is detectable and that the plasma volume is once again occupied by neutral constituents at or near ambient conditions.

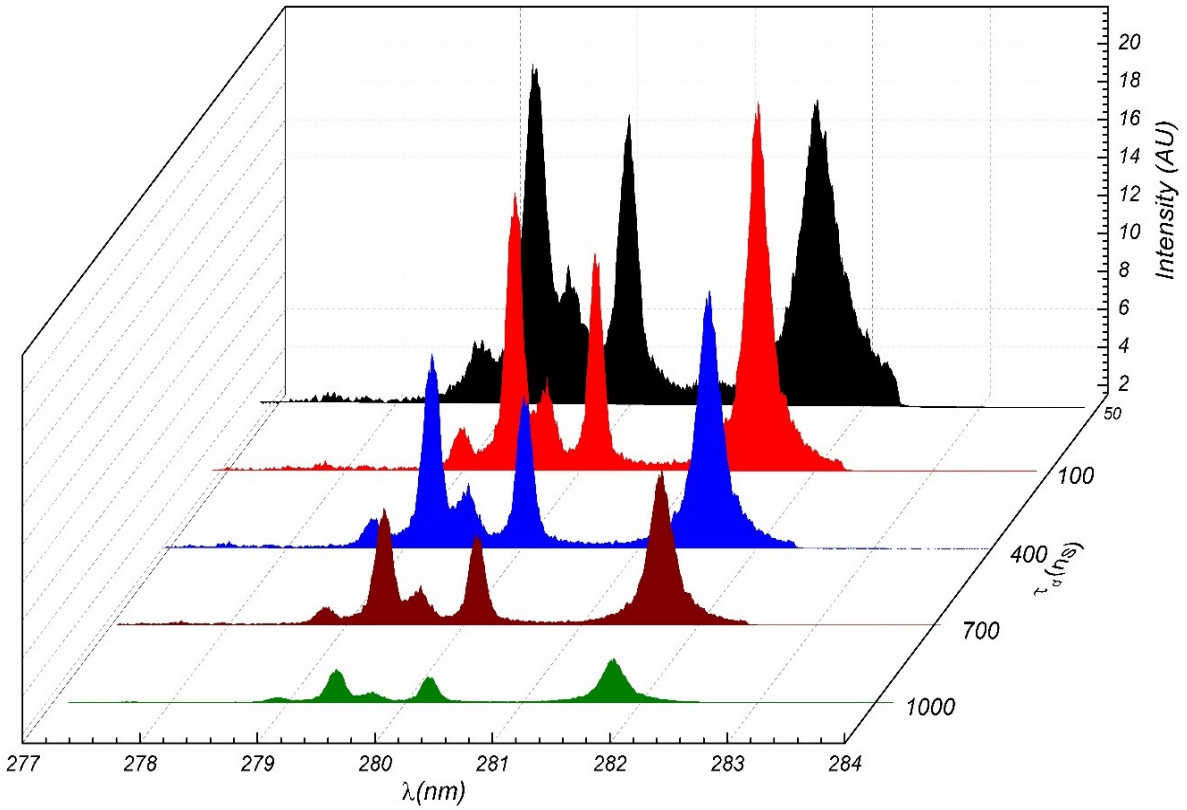

***Figure (3-1)**: Time dependent behavior of optical emission intensity of Al plasma in the presence of Ar at 100 Torr. The wavelength range contains the AlII line at 281.6 nm, as well as MgII line at 279.55 and 280.7nm.*

Figure (3-2) shows the emission intensity in the 279 to 283 nm region 100 ns after laser shots for pressures varying from vacuum to 760 Torr of Ar. The intensity of the lines significantly increases with rising pressure, which can be (at least in part) explained by the plasma's confinement due to the surrounding gas. It is indeed observed that at low pressure the plume is long and conical, ~2 cm in length, while at higher pressure the expansion is spherical and the plume becomes short, e.g. ~1 cm. Figure (3-3) illustrates the pressure dependence of the plasma length, determined 1μs after the laser pulse from the spectrum of Al II(281.6 nm) line. One can clearly see that the length decreases monotonously with increasing pressure. Furthermore, the length is the shortest in argon that exhibits the highest mass density. Clearly, this suggests that the ambient gas influences the importance of plasma confinement.

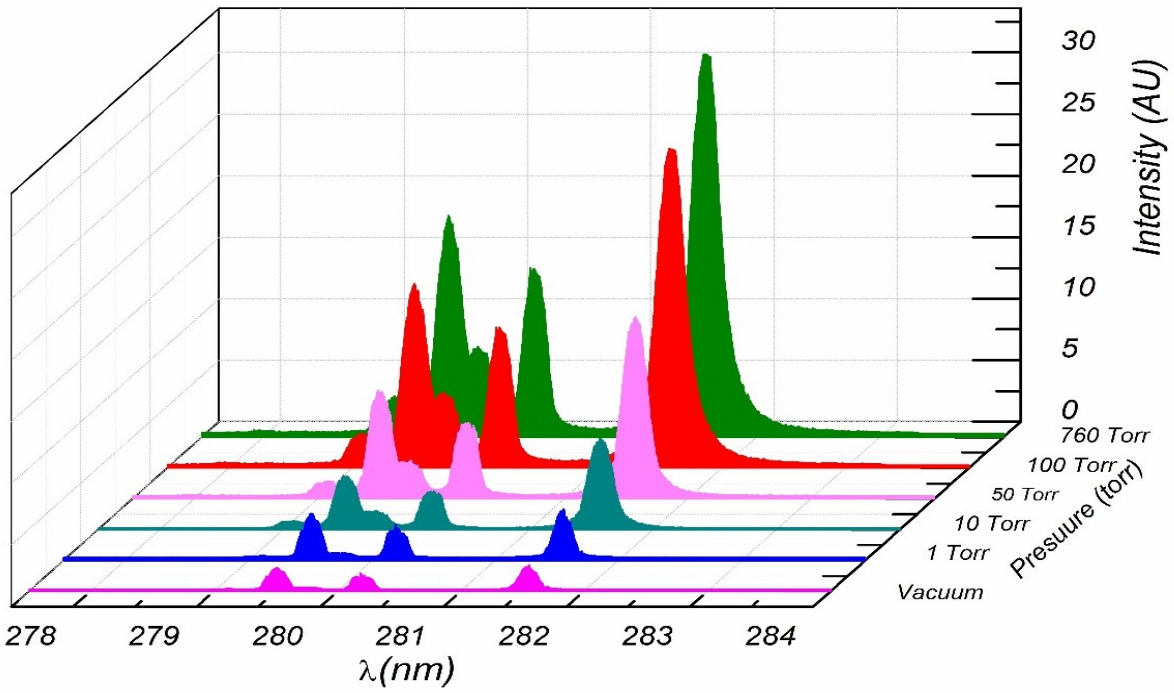

***Figure (3-2)**: The effect of ambient gas pressure on Al II ion line intensity at delay time 100 ns after laser shots. The wavelength range contains the AlII line at 281.6 nm, as well as MgII line at 279.55 and 280.7nm.*

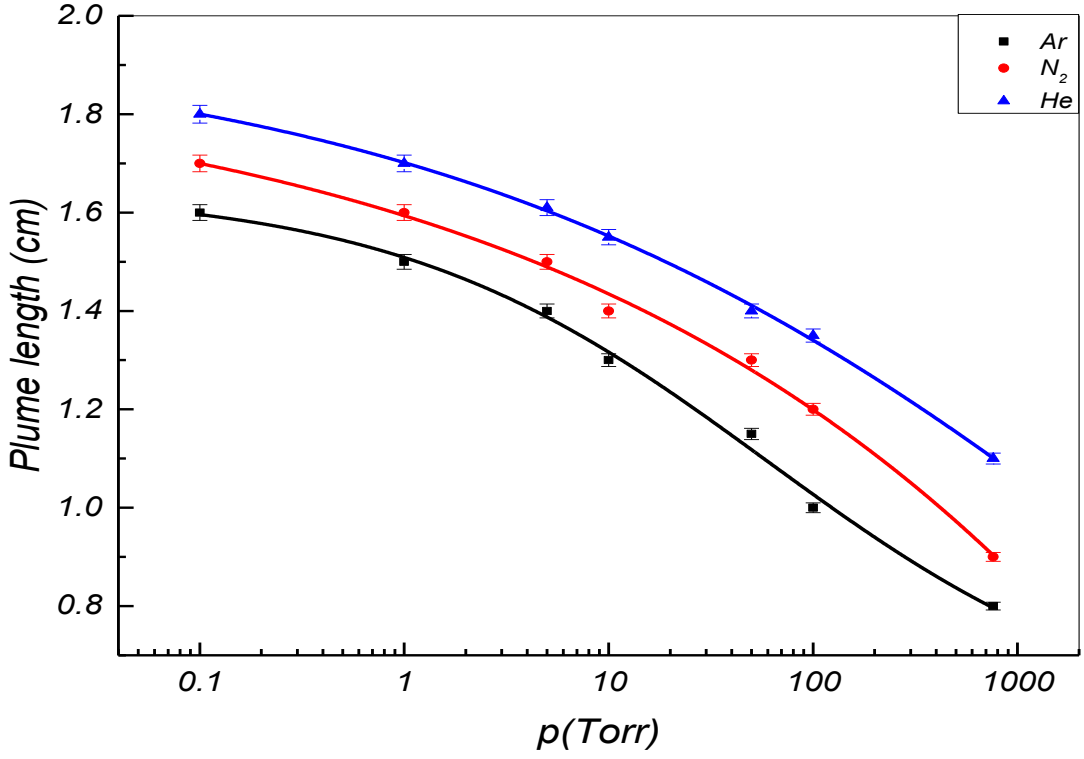

***Figure (3-3)**: Length of the plasma plume as a function of ambient gas pressure and nature.*

The emission intensity also strongly depends on the ambient gas pressure and nature as can be seen in Figure (3-4). From this figure, it can be seen that the intensity not only drastically increases with pressure, as anticipated from Figure (3-1), but also significantly varies with the gas nature. The highest intensity is indeed obtained for Ar while He yields the lowest, with N_2 showing an intermediate value. In addition, the spectral intensity is found to increase more rapidly with pressure in the case of Ar and N_2 than with He, as clearly seen in Figure (3-4). The great importance of the plasma line intensity in Ar could be attributed to the rather lower ionization potential, and to the higher mass density of this gas, as compared to He, which results in an environment favourable to enhanced plasma confinement, hence of electron density [2-4]. Furthermore, the much larger thermal conductivity of He compared to Ar and N_2 causes the plasma to cool faster through heat exchange with the He atoms, after that the excitation of the plasma atoms decreases rapidly with rising gas pressure.

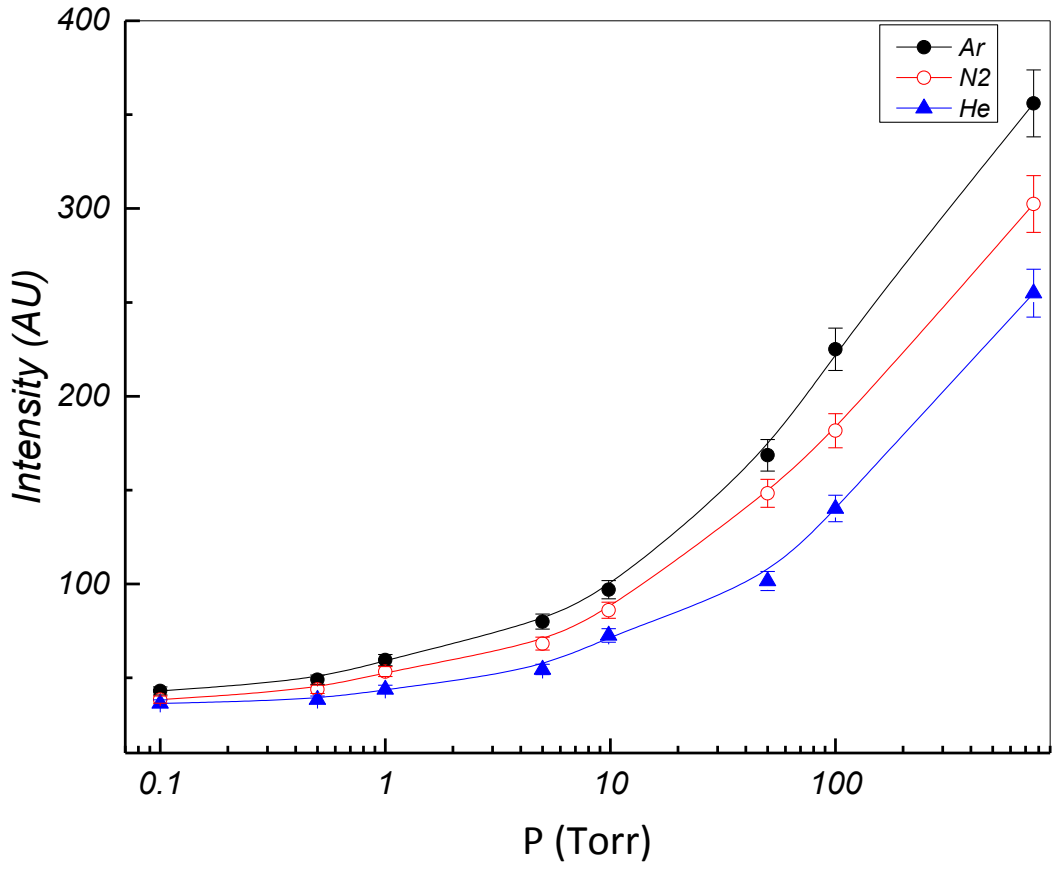

***Figure (3-4)**: Effect of ambient gas pressure and nature on the intensity of the Al II line at 281.6 nm.*

In conclusion of this section, our results show that the presence of ambient gas influences the plasma emission in several ways. The line intensity is strongly affected by the plume confinement that differs with the nature of the ambient gas and its pressure. In particular, the line intensity drops more rapidly with pressure in lighter gases. In addition, both signal-to-noise ratio and peak intensity increase in the heavier gases, which in good accordance with the results obtained by Cowpe *et al.* [5], Vadillo *et al.* [6] and Dreyer *et al.* [7]. This implies that for application to LIBS, Ar produces the most favourable environment.

Finally, whatever the gas pressure or gas type there is no optimum gas pressure region, where the emission intensity is maximum like that observed by Yalcin *et al*. [8], Bashir *et al*. [9] and Shaikh *et al.* [10]. Moreover, at low pressure our results didn't show the emission intensity enhancement proposed by Cremers and Radziemski [11], and Amoruso *et al*.[12]. They refer these enhancements to the ambient gas breakdown and shielding effect. Though, at low pressure there is a lack of ambient atmosphere to produce sufficient confinement. Consequently, there is a steep loss in the plasma emission intensity as previously mentioned.

3.3 Dependence of electron density on delay after laser shot, gas pressure and nature

To understand why line emission depends so strongly on pressure and gas nature, the n_e was measured using Stark broadening of AlII 281.6 nm (below 1 µs) and AlI 394 nm (above 1 µs) spectral lines. The temporal evolution of n_e of laser plasma generated in Ar, N_2 and He at 9 pressures was determined for time delays varying from 50 ns to 10 µs.

Figure (3-5) shows the time dependence of n_e in the case of Ar as ambient gas, for the cases of gases N_2 and He see Figure (A-1 and A-2) in the appendix I. As expected, n_e decreases with time. A detailed analysis of the time-resolved data shows that n_e falls rapidly at the very beginning and then decreases exponentially with time after about 500 ns, it is clearly seen in Figure (A-3) in the appendix I. This drop results from electron and ion recombination yielding neutral atoms. In addition, the most important temporal variation is observed at the highest investigated pressure, i.e. atmospheric pressure. At the opposite, in vacuum, the time dependence is rather slow, with only a factor of 4 between 50 ns and 10 µs.

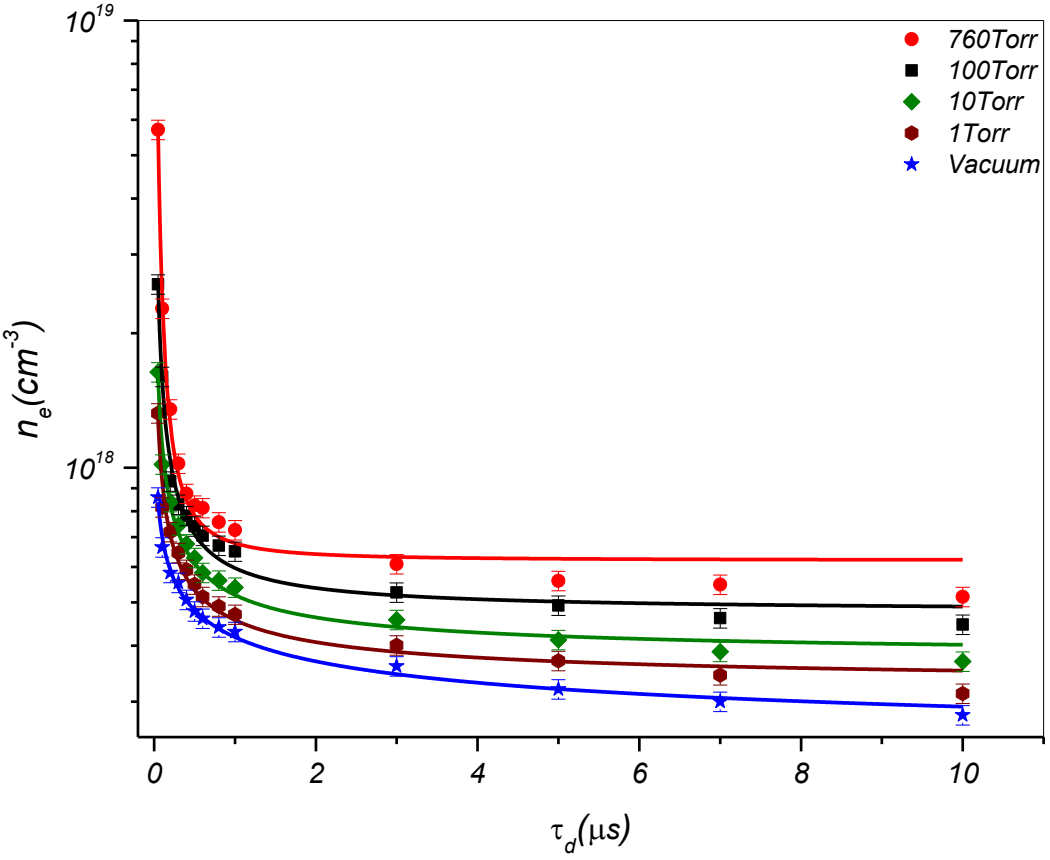

***Figure (3-5)**: Time dependence of n_e for various Ar pressures.*

Overall, at any delay, n_e increases with rising pressure. This is the result of plasma confinement as will be seen later. For Ar, the n_e reaches a maximum value of 5.7 x 10^{18} cm^{-3} at 50 ns after the laser pulse, while the lowest (3 x 10^{17} cm^{-3}) is occurs in vacuum after 10 µs. Our values are in good agreement within the experimental error to the published data of the work done by Aguilera *et al.* [13], Benedetti *et al.* [14] and El Sherbini *et al.* [15].

Figures (3-6a and 6b) compare the effect of ambient gas composition (He, Ar and N_2) on the time dependence of n_e for two different pressure values. Clearly, at both pressures, Ar always results in the highest n_e and He in the lowest, with N_2 yielding intermediate values. The dependence on the nature of the gas is also similar at both pressures. For example, after 600 ns, n_e decreases by about 50% when exchanging Ar for He.

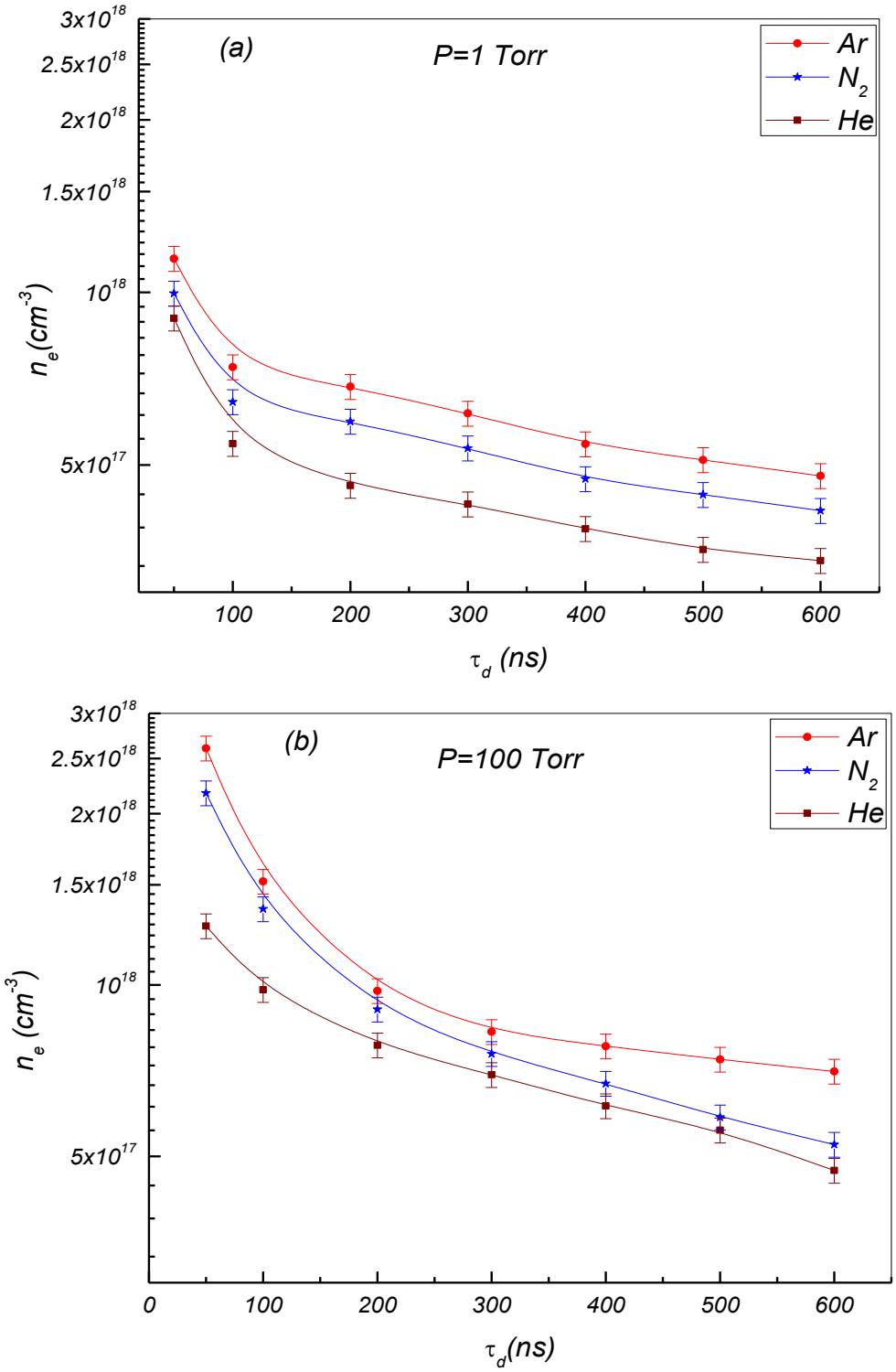

***Figure (3-6)**: Time dependence of n_e at (a) 1 Torr and (b) 100 Torr for the three different gases investigated.*

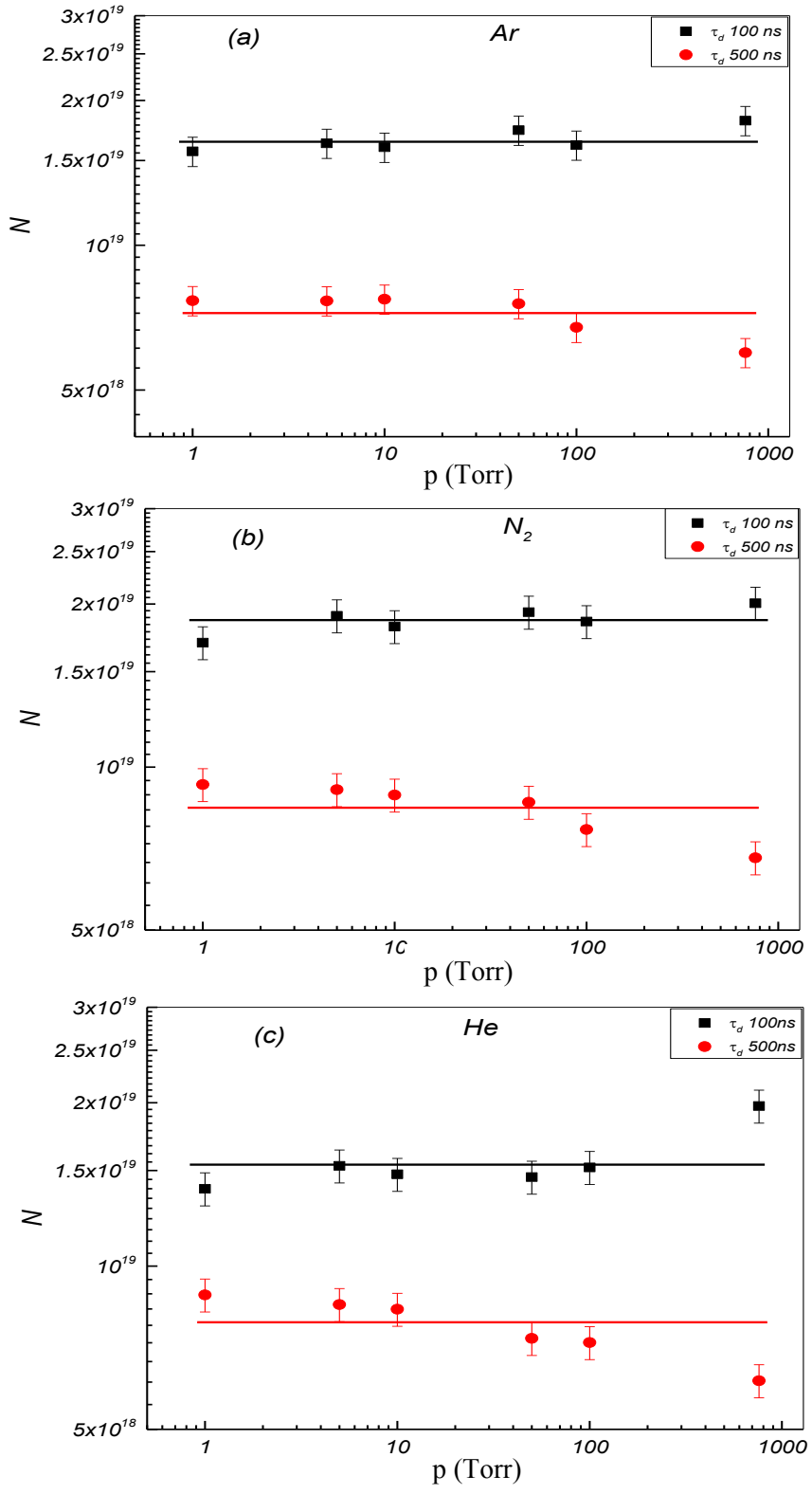

***Figure (3-7)**: Pressure dependence of the total number of electrons in the plasma plume at two delays after laser pulse for (a) argon, (b) nitrogen and (c) helium.*

In order to quantify the importance of confinement and its role in the plasma behaviour, we have estimated the total number of electrons, N, in the plasma in various experimental conditions. This number is determined by multiplying the measured electron density by the plasma volume estimated from its shape (hemispherical, conical, etc.), its radial extension and its length. Figures (3-7a to 7c) show the results obtained as a function of pressure for two different delays after laser shots and for the three ambient gases investigated. Interestingly, one clearly sees that in a first approximation, N nearly constant with rising pressure and almost independent of the gas type. These two observations undoubtedly indicate that plasma expansion is fully inhibited by the presence of the ambient gas when the pressure increases. It also means that the creation of the plasma is not influenced by its environment at time delay < 200 ns. As expected, at time delay 500 ns, N decreases with time delay after laser shots, which is simply due to recombination. Detailed observations suggest a slight decrease of N at atmospheric pressure. This may indicate a stronger interaction between the plume and the gas at higher pressures. However, we have to be careful since the volume was roughly estimated so that it may happen that these variations may not be significant.

3.4 Dependence of excitation temperature on time delay after laser shot, gas pressure and nature

The knowledge of electron temperature is the main key to understand the dissociation, atomization, ionization and excitation occurring in the plasma. In laser-induced plasmas, the electron temperature is usually considered as close to the excitation temperature determined from excitation spectra by examining the distribution of excited atomic or ionic populations. Using the Boltzmann plot method and under the assumption of (LTE), T_e is obtained from the observed intensity of several lines from Fe impurities contained in the Al target. The time dependence of the excitation temperatures for Ar environment is shown in Figure (3-8) for various pressures. It is observed that the temperature relaxes rapidly (about 1-2 μs) to a lower value and then decreases more slowly. For example, at atmospheric pressure, the initial T_e

drops from 9000K at 100ns to 5800K at 30 µs. The same behaviour is observed at each pressure, T_e values being simply lower everywhere when the pressure decreases. This can be understood as being due to the more rapid expansion of the plasma at lower pressure, which makes the total plasma energy distributed over a larger volume. The temporal dependence of T_e in the existence of N_2 and He are shown in Figure (A-4 and A-5) in the appendix I.

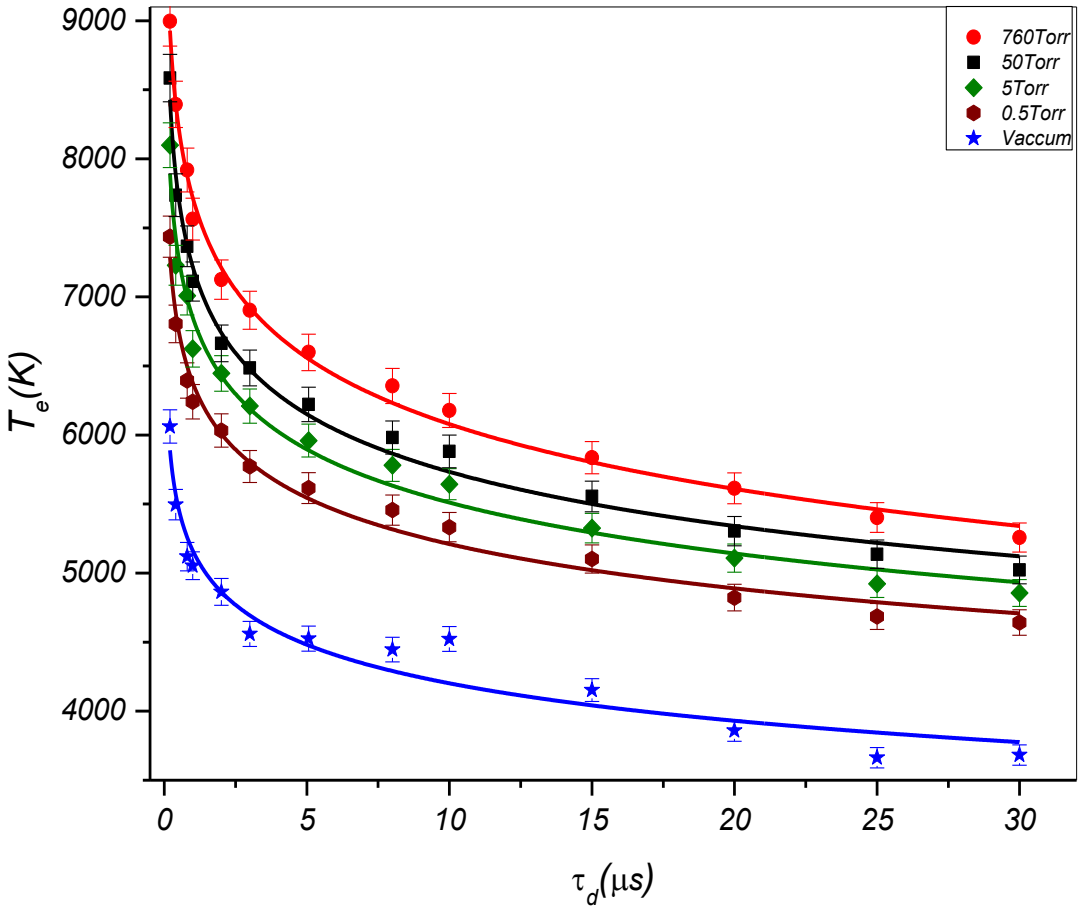

***Figure (3-8)**: Time dependence of T_e for different gas pressure in Ar atmosphere.*

The time variation of T_e of the three ambient gases investigated is presented in Figure (3-9a and 9b) for two different pressures. At both pressures, He is observed to result in the lowest temperature, while Ar provides the highest and N_2 an intermediate value, similar to the observations made for n_e. The fact that the lower temperature values occur in He results from

the much larger thermal conductivity of this gas, which makes the plasma/environment interaction more efficient.

Finally, our observation does not show any optimum pressure for neither n_e nor T_e as their values monotonously decrease with rising pressure. This contrasts with the results reported by Iida [16], Asimellis *et al.* [17], Knight *et al*. [18] and Farid *et al.* [19] who observed a maximum excitation at some finite pressure. The authors attribute such a trend to the interaction of the plasma with the ambient gas where the later act as an energy buffer transferring a fraction of its energy to the Al plasma in low pressure, while at high pressure, collisions of electrons with gas atoms increases so that the cascade condition is not favoured and n_e consequently decreases. However, this assumption clearly contradicts the hydrodynamic hypothesis where the plasma plume pushes out the ambient gas by generating a shockwave. Hence there is no way for the energy to transfer from the gas to the plume and there is no possible electron-gas atom collision until the plume inside pressure approximately reaches the ambient one [20-23]. It remains that the most highly energetic species at the plasma plume front may still interact with the ambient gas and may induce its excitation or ionization. Therefore, the compression of the ambient gas by the generated shockwave should not be considered as fully adiabatic.

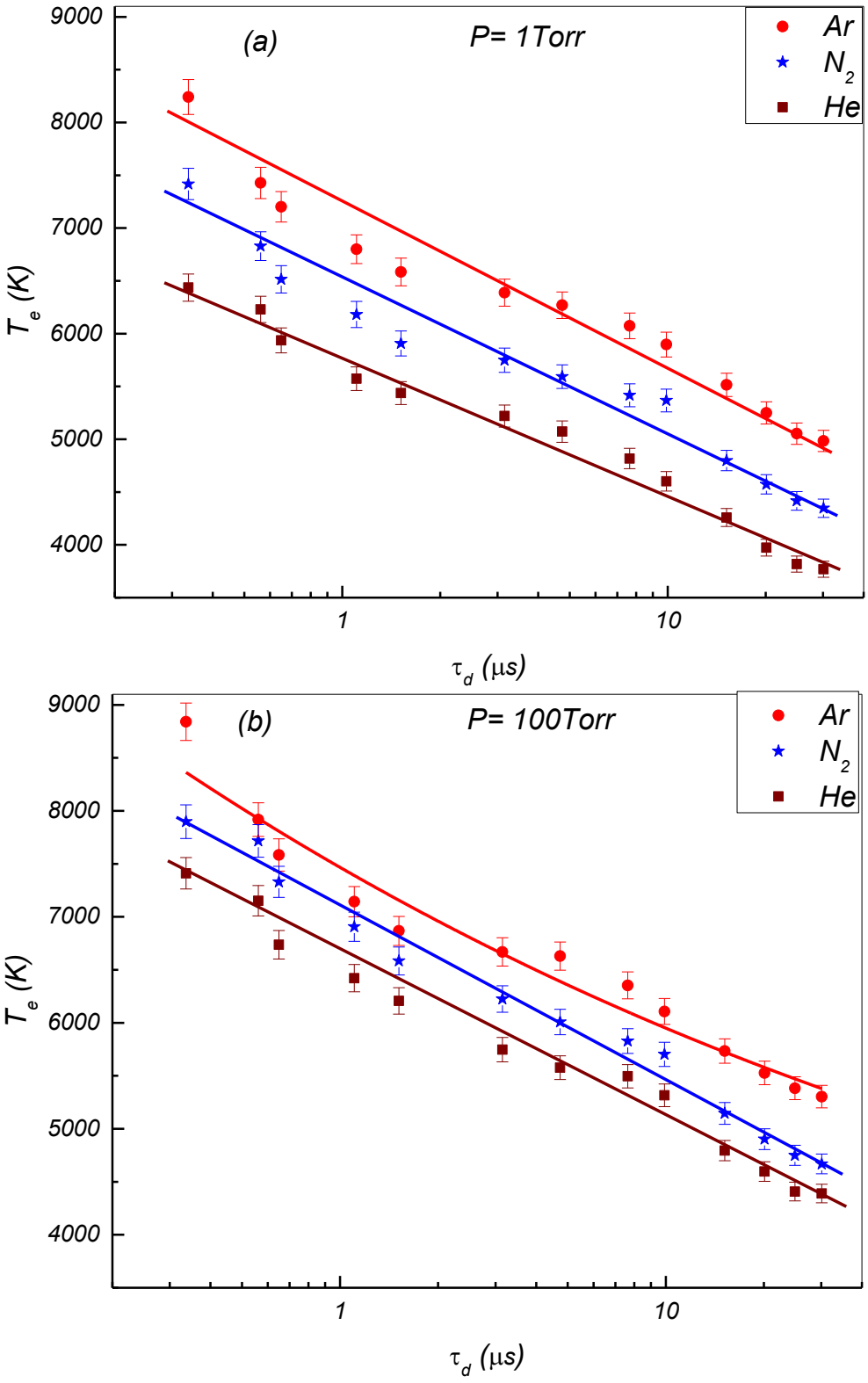

***Figure (3-9)**: Time dependence of T_e at (a) 1 Torr and (b) 100 Torr for the three ambient gases.*

3.5 Conclusion

In summary, the time-resolved emission spectroscopy of Al II at 281.6 nm and Al I at 394 nm lines is found to be strongly affected by the plume confinement that differs with the nature of the ambient gas and its pressure. The intensity is strongly enhanced in Ar as ambient gas, which results in an environment favourable to LIBS application. These phenomena are explained by the relatively low ionization potential and to the high mass density of this gas as compared to He and N_2.

The time dependence of n_e and T_e in Ar, N_2 and He at different pressures fall rapidly at the very beginning and then decrease exponentially with time. In addition, He produces the fastest decay due to its highest thermal conductivity while Ar yields the slowest and N_2 an intermediate behavior. Moreover, both n_e and T_e are the highest in Ar as compared to other gases, which reveals the existence of a stronger plasma confinement in Ar atmosphere.

Finally, in all conditions, (either various delay times or different gas atmospheres) there is no optimum pressure for neither the electron density nor the excitation temperature, which is consistent with the hydrodynamic hypotheses.

3.6 References

[1] J. Hermann, S. Bruneau, Thin Solid Films 453-454, 377, 2004.

[2] Y. Lee, K. Song and J. Sneddon, "Laser induced plasmas for analytical atomic spectroscopy" ch. 5 in Lasers Analytical Atomic Spectroscopy, J. Sneddon et al (Eds.), New York: VCH, 197-235, 1997.

[3] W. Sdorra and k. Niemax, Mikrochim. Acta 107, 319, 1992.

[4] H. Lindnera, K. H. Loperb, D. W. Hahnb and K. Niemax, Spectrochim. Acta B 66, 179, 2011.

[5] J.S. Cowpe, J.S. Astin, R.D. Pilkington, A.E. Hill, in *4th Euro Mediterranean Symposium on Laser Induced Breakdown Spectroscopy*, Paris, France, September 11-13, 1066-1071, 2007.

[6] J.M. Vadillo, C.C. Garcia, S. Palanco , J. Ruiz and J.J. Laserna, *Spectrochim. Acta, Part B*, vol. 56, pp. 923–31, 2001.

[7] C.B. Dreyer, G.S. Mungas, P. Thanh, J.G. Radziszewski, *Spectrochim. Acta, Part B*, vol. 62, pp. 1448-1459, 2007.

[8] Serife Yalcın, Ying Y. Tsui and Robert Fedosejevs, *J. Anal. At. Spectrom.*, vol. 19, pp. 1295 – 1301, 2004.

[9] S. Bashir, N. Farid, K. Mahmood and M.S. Rafique, *Appl. Phys. A*, vol. 107, no. 1, pp. 203–212, 2012.

[10] N.M. Shaikh, S. Hafeez, M.A. Baig, *Spectrochim. Acta, Part B,* 62, 1311, 2007.

[11] D. A. Cremers and L. J. Radziemski, *Handbook of Laser-Induced Breakdown Spectroscopy*. Chichester: Wiley, 2006.

[12] S. Amoruso, R. Bruzzese, N. Spinelli and R. Velotta, *J. Phys. B: At. Mol. Opt. Phys.*, vol. 32, pp. R131–R172, 1999.

[13] J.A. Aguilera, C. Aragón, Appl. Phys. A 69, S475–S478, 1999.

[14] P.A. Benedetti, G. Cristoforetti, S. Legnaioli, V. Palleschi, L. Pardini, A. Salvetti, E. Tognoni, *Spectrochim. Acta, Part B*, 60, 1392–1401, 2005.

[15] A.M. El Sherbini, H. Hegazy, Th.M. El Sherbini, *Spectrochim. Acta, Part B*, 61, 532–539, 2006.

[16] Y. Iida, Spectrochim. Acta B 45, 1353, 1990.

[17] G. Asimellis, S. Hamilton, A. Giannoudakos and M. Kompitsas, *Spectrochim. Acta, Part B,* 60, 1132, 2005.

[18] A. K. Knight, N. L. Scharbarth, D. A. Cremers and M. J. Ferris, Appl. Spectrosc. 54, 331, 2000.

[19] N. Farid, S. Bashir and K. Mahmood, Phys. Scr. 85, 015702 (2012).

[20] Q. L. Ma, V. Motto-Ros, W. Q. Lei, M. Boueri, X. S. Bai, L. J. Zheng, H. P. Zeng and J. Yu, *Spectrochim. Acta, Part B,*65, 896, 2010.

[21] A. De Giacomo, M. Dell'Aglio, R. Gaudiuso, S. Amoruso and O. De Pascale, Acta B 78, 1 (2012).

[22] O. Barthelemy, J. Margot, S. Laville, F. Vidal, M. Chaker, B. Le Drogoff, T. W. Johnston and M. Sabsabi, Appl. Spectrosc. 59, 529 (2005).

[23] S. C. Singh, H. B. Zeng, C. Guo & W. Cai, eds. Nanomaterials: processing and characterization with lasers, John Wiley & Sons, 2012.

CHAPTER 4:

Axially- and radially- resolved electron density and excitation temperature of aluminum plasma induced by nanosecond laser pulses: effect of the ambient gas composition and pressure

Chapter 4:

Axially- and radially-resolved electron density and excitation temperature of aluminum plasma induced by nanosecond laser pulses: effect of the ambient gas composition and pressure[1]

4.1 Introduction

The spatial variation of the characteristics of an aluminum plasma induced by a pulsed nanosecond XeCl laser is studied is this chapter. The electron density and the excitation temperature are deduced from time- and space- resolved Stark broadening of an ion line and from a Boltzmann diagram, respectively. The influence of the gas pressure (from vacuum up to atmospheric pressure) and compositions (argon, nitrogen and helium) on these characteristics is investigated. It is observed that n_e occurs near the laser spot and decreases by moving away both from the target surface and from the plume center to its edge. n_e increases with the gas pressure, the highest values being occurred at atmospheric pressure when the ambient gas has the highest mass, i.e. in argon.

T_e is determined from the Boltzmann plot of line intensities of Fe impurities present in the Al target. The highest T_e is observed close to the laser spot location for Ar at high pressure. It decreases by moving away from the target surface in the axial direction. However, no significant variation of temperature occurs along the radial direction. The differences observed between the axial and radial direction are mainly due to the different plasma kinetics in both directions.

[1] This chapter is part of article: Mahmoud S. Dawood, Ahmad Hamdan and Joelle Margot, submitted to Journal of Physics B: Atomic, Molecular and Optical Physics (2015).

4.2 Axial dependence of electron density and excitation temperature

Using the Stark broadening method presented in chapter 2, n_e is studied for different ambient gases and pressures at different axial, z, (perpendicular to the target) and radial, r, (parallel to the target) positions. In Figure 4-1, we present the axial variation of the radially integrated n_e in Ar gas at pressures varying from vacuum to 760 Torr. These measurements are carried out at three times-delays after the laser pulse, namely 100 ns (Figure 4-1a), 500 ns (Figure 4-1b) and 1000 ns (Figure 4-1c).

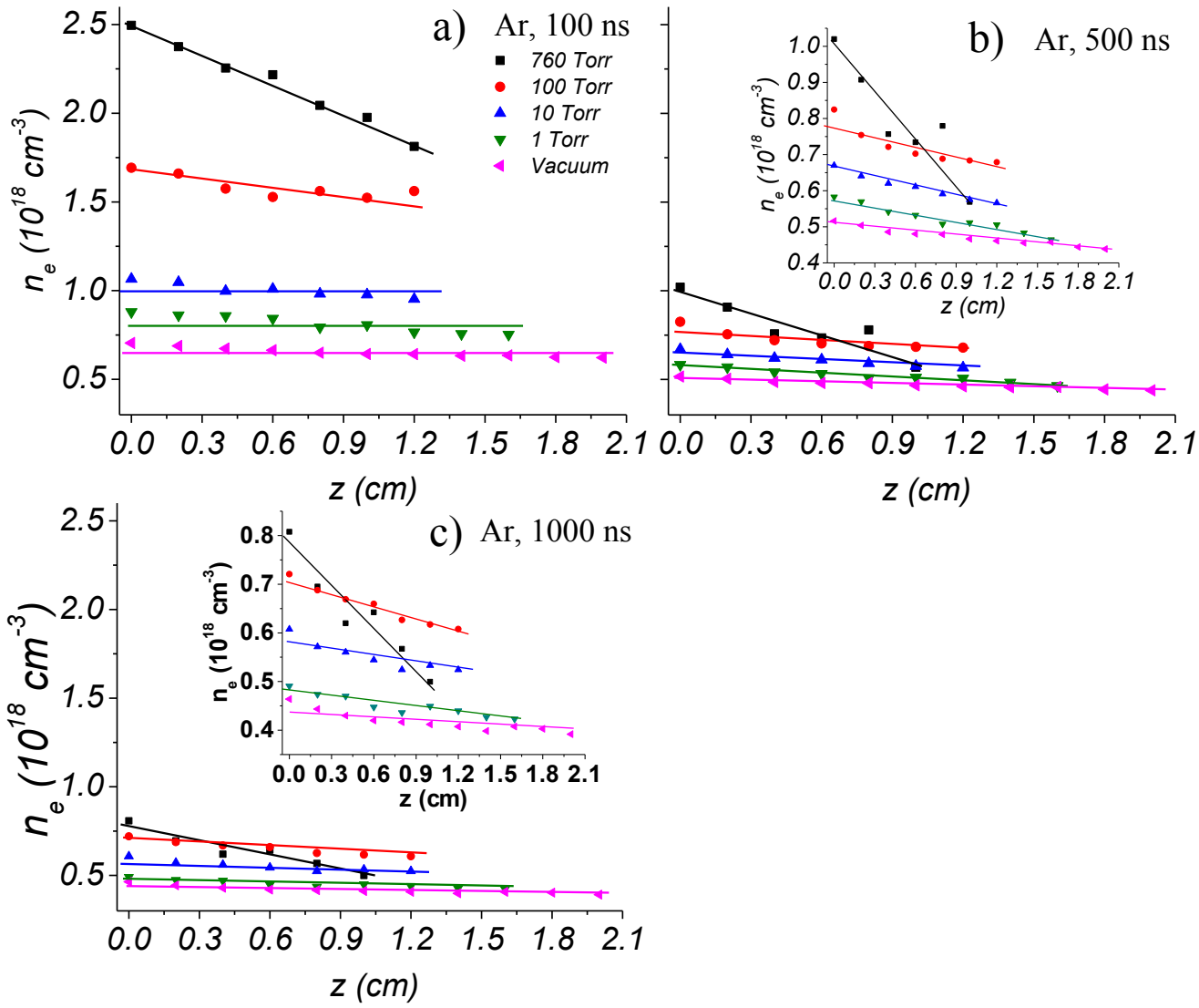

***Figure (4-1)**: Axial variation of n_e in ambient Ar for different pressures (from vacuum up to atmosphere) at a) 100 ns, b) 500 ns and c) 1000 ns. The insets show the same experimental results with an expanded vertical scale.*

Before discussing the results, let us mention that the plasma length depends on the gas composition and pressure as reported in details in the references [1-6]. Therefore, the maximal value of z depends on their experimental conditions. First of all, as it can be seen in Figure (4-1), n_e decreases with time and with the distance from the target surface, the latter corresponding to $z = 0$. At high pressure and at 100 ns (Figure 4-1a), n_e attains its highest value (~2.5×10^{18} cm^{-3} at $z = 0$) and decreases linearly to ~1.8×10^{18} cm^{-3} at $z = 1.2$ cm.

At lower pressures (typically < 10 Torr), the spatial variation is less important, and n_e is almost constant along the plume axis. In addition, n_e decreases, when the pressure is reduced, varying from ~1.6×10^{18} at 100 Torr to ~0.65×10^{18} cm^{-3} in vacuum. At 500 ns (Figure 4-1b) and 1000 ns (Figure 4-1c), n_e is significantly reduced and it varies, depending on the gas pressure, from 0.5×10^{18} to 1×10^{18} cm^{-3} at 500 ns and from 0.4×10^{18} to 0.8×10^{18} cm^{-3} at 1000 ns. At given gas pressure, the axial variation of n_e is generally insignificant at the exception of the atmospheric and 100 Torr pressures. When Ar is replaced by N_2 or He, n_e keeps a similar behavior (Figures 4-2 and 4-3). However, one still observes some differences. For instance, at atmospheric pressure and at 500 ns, the highest density n_e occurs for N_2 (~3.1×10^{18} cm^{-3} at $z = 0$) and the lowest for He (~2×10^{18} cm^{-3} at $z = 0$). Similar trends are observed at the later time delay. Again, at atmospheric pressure, the gradient of n_e is higher compared to other pressures. This is in part due to the greater confinement of the plume by the ambient atoms when the pressure is high. However, this behavior can also be attributed to two other phenomena, namely electron-ion recombination and formation of nanoparticles and clusters. Indeed, at higher pressure, both the plasma plume volume and the inter-particles distance are reduced. Thus, the plasma is more strongly correlated. However, the rate of the electron-ion recombination increases substantially leading to the loss of charged particles, in particular the electrons, along the plasma. The second phenomenon is related to the increase of the interaction rate between the aluminum-ablated nanoparticles, which leads to the formation of clusters. The surface of these clusters becomes so huge that it can collect the free electrons present in the plasma [7, 8] resulting in a reduction of the density. Indeed, because of the nanoparticles ejection and of their transport along the axial direction, the electron collection takes place progressively as one move away from the target surface, which results in a higher n_e gradient.

Several authors observe a different behavior of the n_e axial variation during the ablation of Al in air [9, 10]. Their axial distribution of n_e is spatially structured, showing a shallow minimum. This is attributed to the recombination processes occurring in regions of high number density. On the other hand, Shaikh *et al.* [11] and Aguilera and Aragon [12] have performed ablation of Al and Fe-Ni alloy in air at atmospheric pressure using an Nd:YAG laser. Their results are in agreement with ours and they attribute the decrease to the recombination of the electrons and ions.

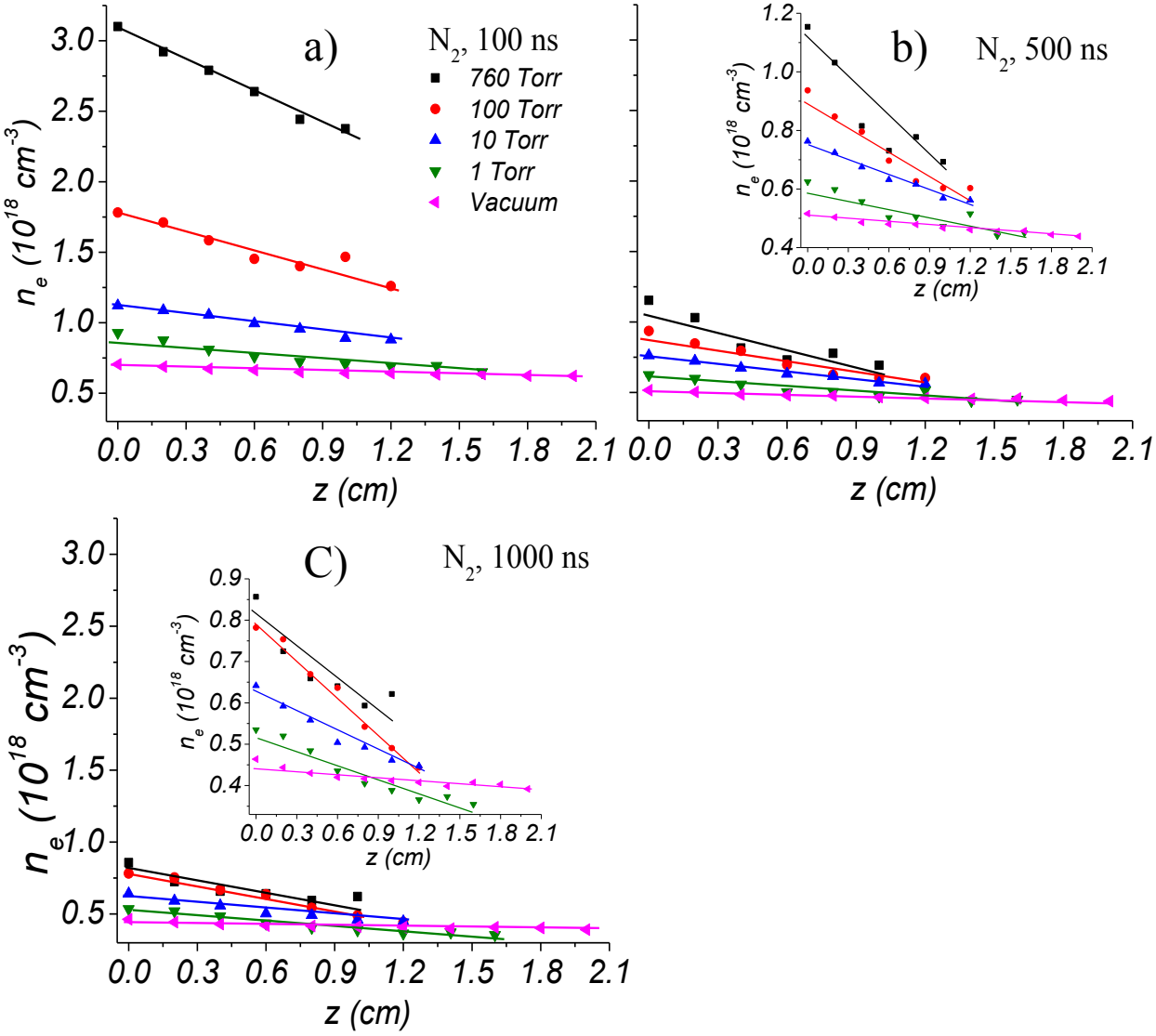

***Figure (4-2)**: Axial variation of n_e in ambient N_2 for different pressures (from vacuum up to atmosphere) at a) 100 ns, b) 500 ns and c) 1000 ns. The insets show the same experimental results with an expanded vertical scale.*

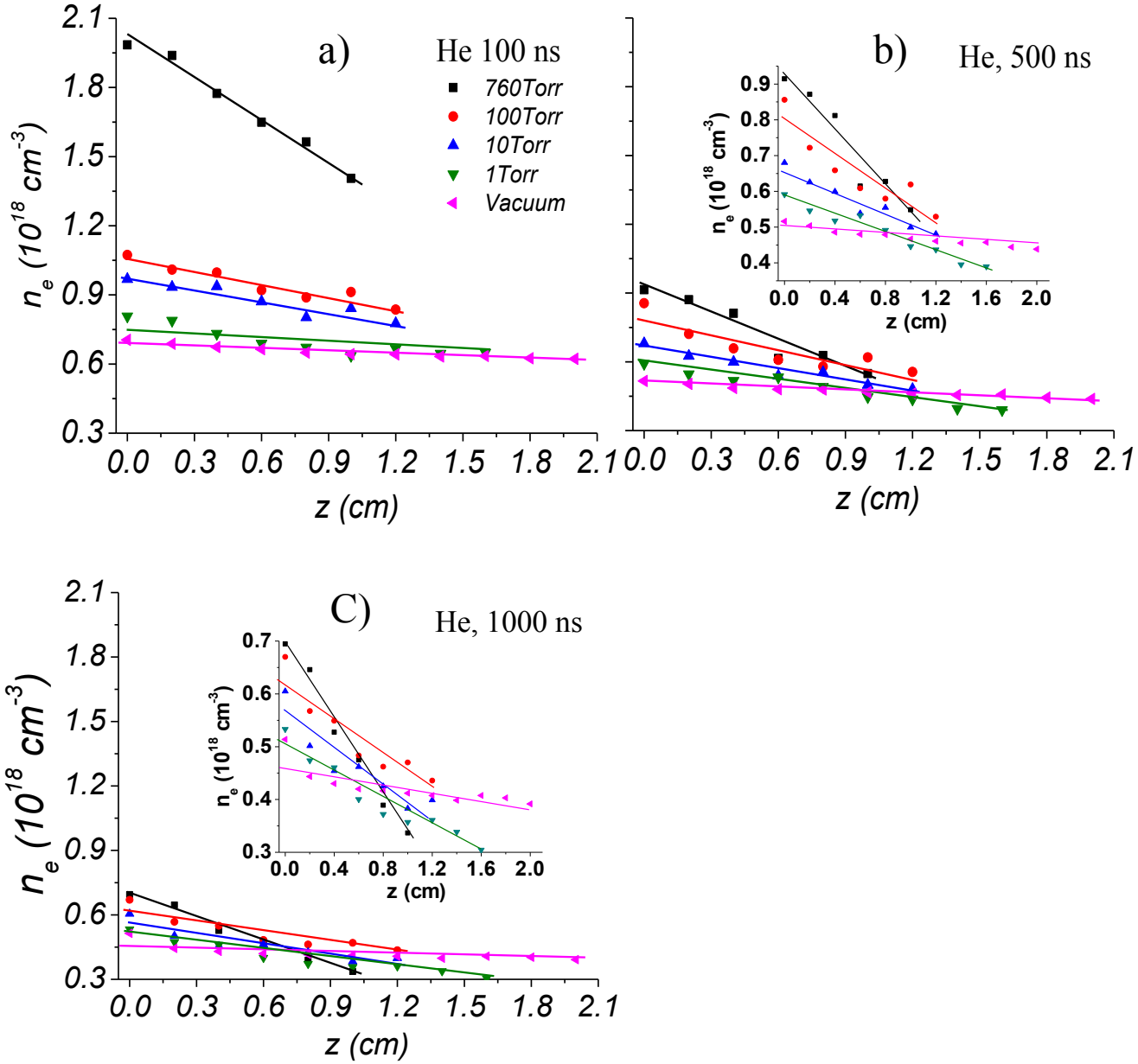

***Figure (4-3)**: Axial variation of n_e in ambient He for different pressures (from vacuum up to atmosphere) at a) 100 ns, b) 500 ns and c) 1000 ns. The insets show the same experimental results with an expanded vertical scale.*

The axial variation of T_e in Ar is presented in Figure (4-4) for different pressures and for three time delays from the laser pulse, 500 ns (Figure 4-4a), 5 µs (Figure 4-4b) and 20 µs (Figure 4-4c). In general, T_e decreases quasi-linearly from the target surface and with time. The highest temperature is obtained at high pressure. At earlier time, the thermal gradient of

the plasma plume is stronger, with a difference of about 1000 K from the target surface ($z = 0$) to the end of the plume, and this remains true over the whole pressure range, from vacuum up to atmospheric pressure. At a later time, the thermal gradient is significantly weaker. For instance, we observe a decrease of ~800 K at 5 µs and ~750 K at 20 µs. In addition, the thermal gradient does not depend much on the argon pressure.

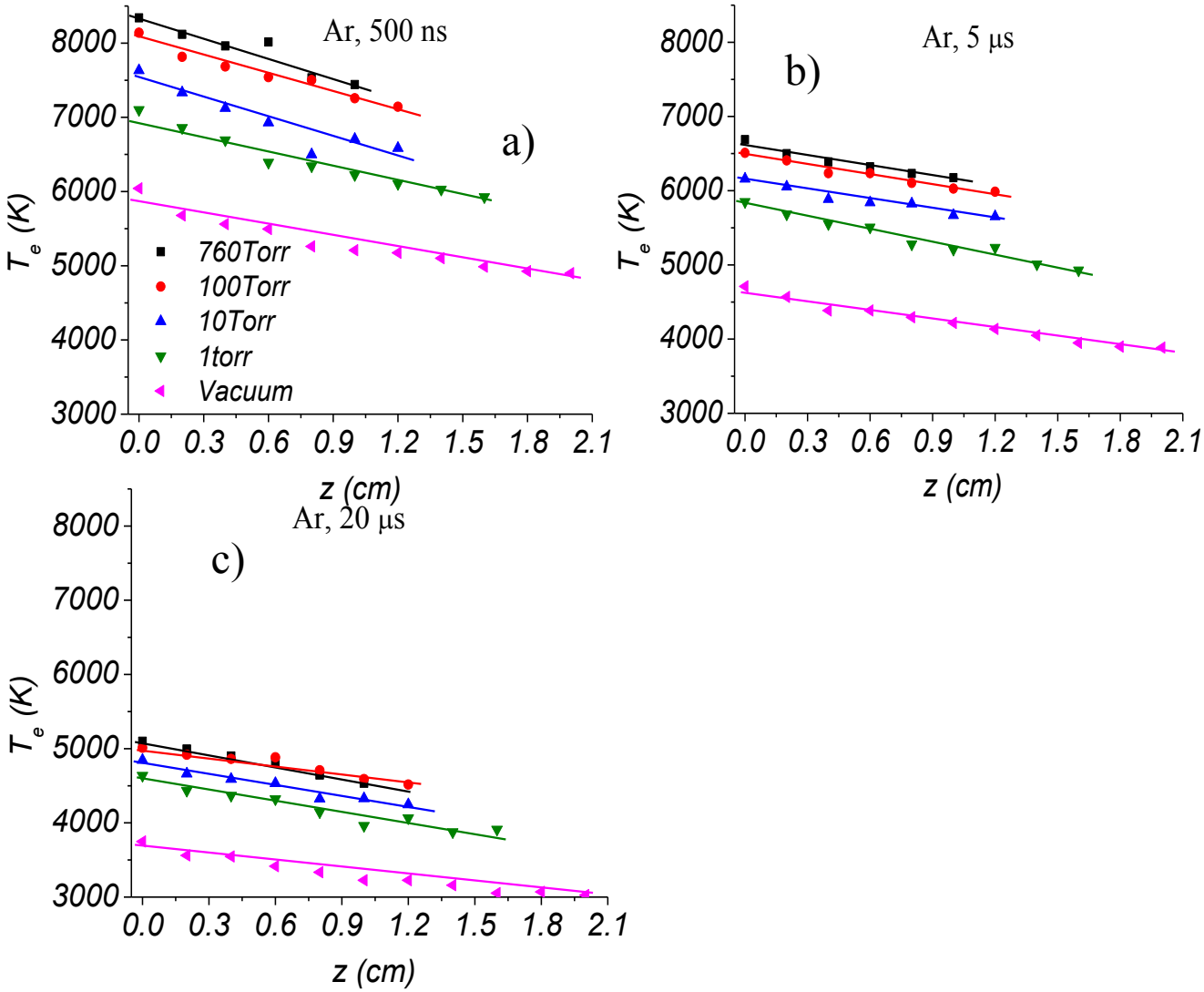

***Figure (4-4)**: Axial variation of T_e in ambient Ar for different pressures (from vacuum up to atmosphere) at a) 500 ns, b) 5 µs and c) 20 µs.*

In the case of N_2 (Figure 4-5), T_e is slightly lower (by hundreds of K) than in Ar. Moreover, at 500 ns, T_e decrease achieved when moving away from the target surface is more rapid than that observed in Ar. At a later time (at 5 and 20 µs), the axial variation becomes

more linear and thus similar to that observed in Ar. We further note that the gas pressure influences the axial gradient. For instance, at atmospheric pressure, T_e drop from the target surface to the end of the plume is ~1500 K at 500 ns, ~1200 K at 5 µs and ~500 K at 20 µs. At low pressure (vacuum), it is rather ~1000 K at 500 ns, 750 K at 5 µs and ~700 K at 20 µs.

In the case of He ambient gas (Figure 4-6), T_e is lower than that obtained in N_2 and in Ar. A nonlinear decrease is observed at atmospheric pressure and at an earlier time (500 ns) where it becomes linear at low pressure (< 10 Torr), similarly to that observed in N_2 and in Ar. Concerning the thermal gradient, at atmospheric pressure, it is ~1400, ~500 and ~550 K at 0.5, 5 and 20 µs, respectively, where at low pressure (vacuum), it is ~1100, ~900 and ~750 K at 0.5, 5 and 20 µs, respectively.

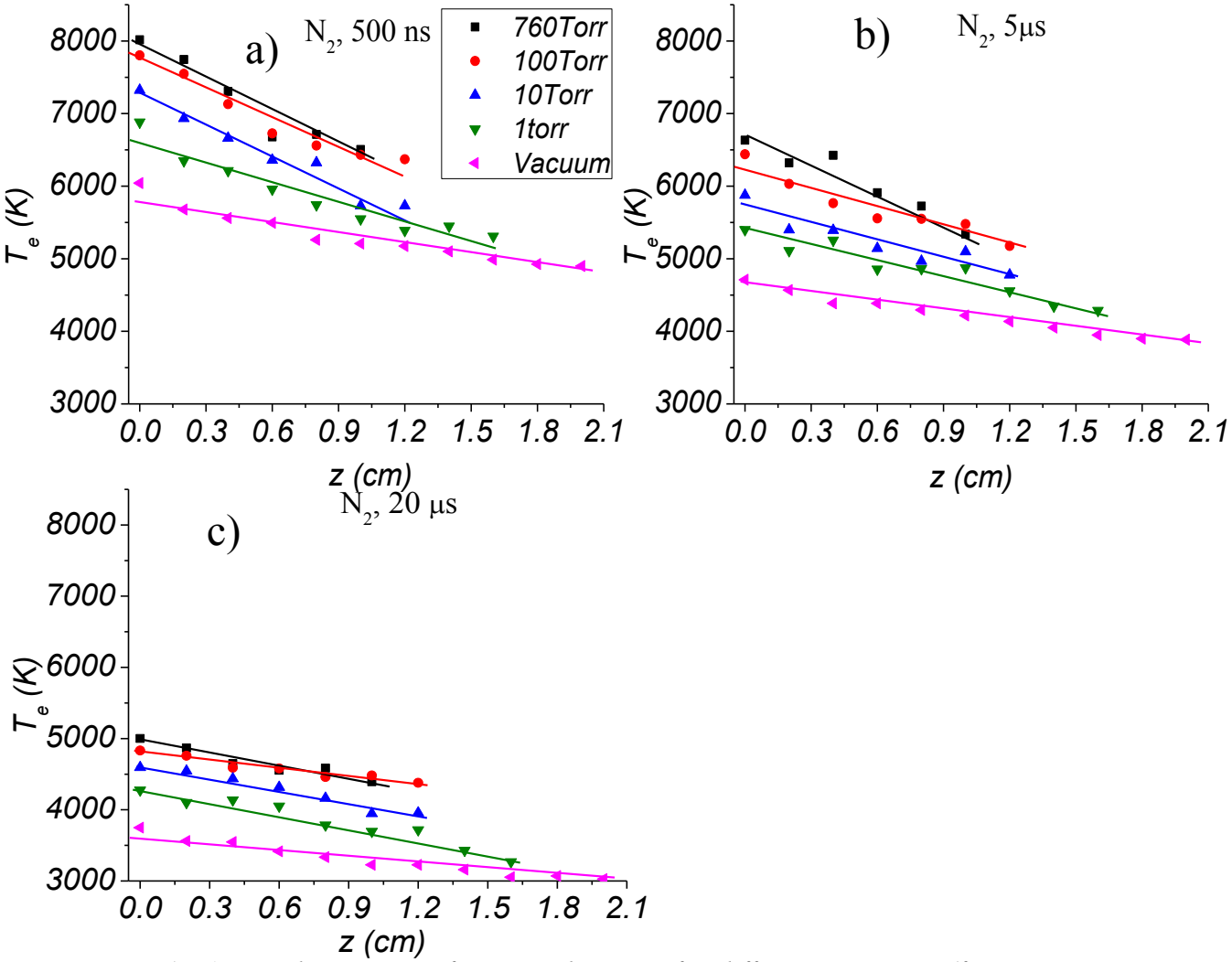

***Figure (4-5)**: Axial variation of T_e in ambient N_2 for different pressures (from vacuum up to atmosphere) at a) 500 ns, b) 5 µs and c) 20 µs.*

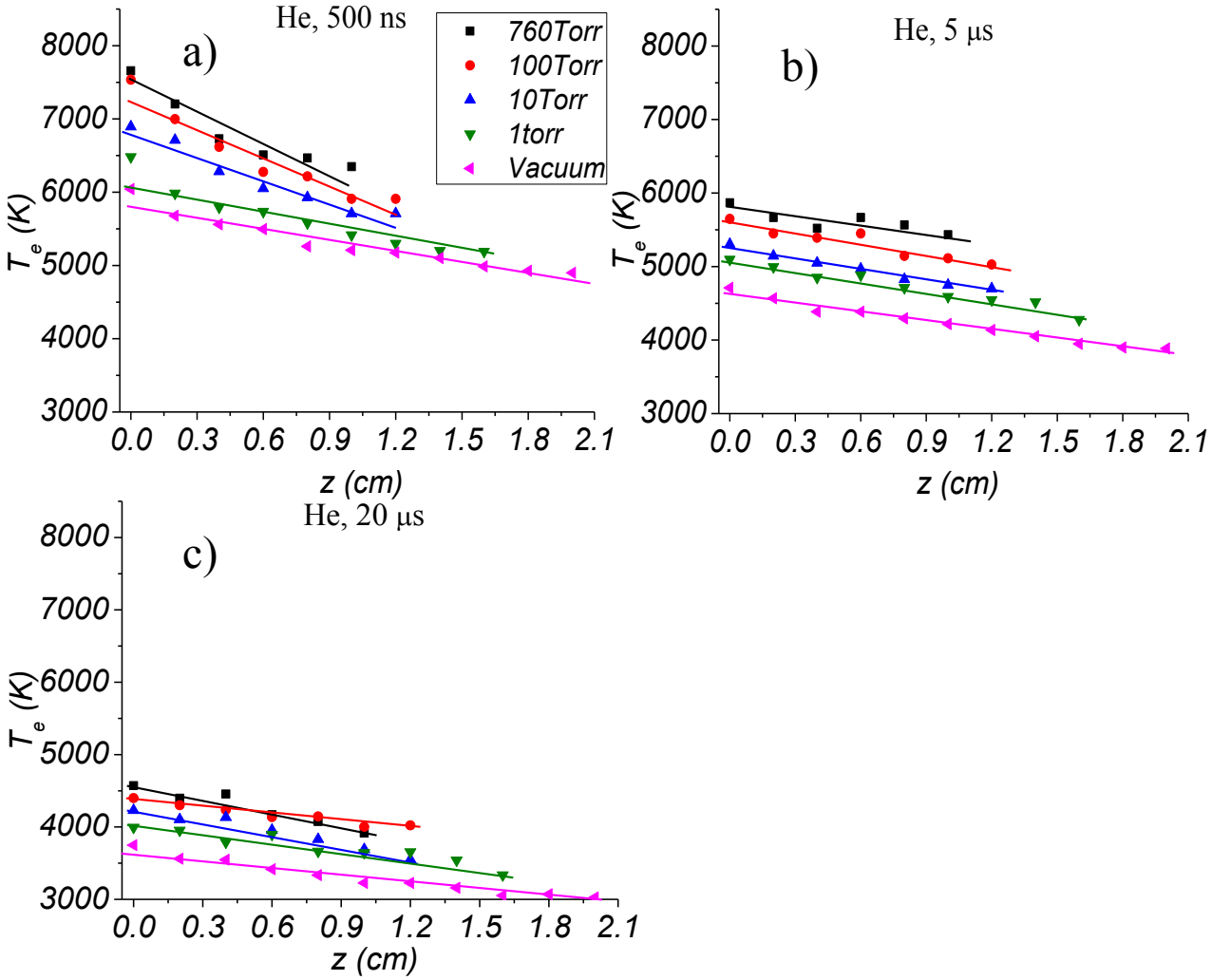

***Figure (4-6)**: Axial variation of T_e in ambient He for different pressures (from vacuum up to atmosphere) at a) 500 ns, b) 5 µs and c) 20 µs.*

The confinement of the plasma plume by the background gas results in a force exerted by the gas species on the plasma species leading to more collisions and heating in the plume. This force depends on the mass of the gas atoms and molecules so that the highest T_e is achieved for Ar and the lowest for He.

In agreement with the observations reported in references [13] and [14], for any gas composition, T_e decreases when the gas pressure is reduced due to less efficient plasma confinement, as the energy is distributed over a large volume. Another mechanism that could explain the axial variation of T_e is the thermal conductivity of the ambient gas. Indeed, the gas with the largest thermal conductivity, helium, results in a faster decrease of T_e than argon at

least at 500 ns. However, when the thermal conductivity is low, argon, the spatial variation of T_e is quasi-linear with independence on the gas pressure. Giacomo *et al.* [9], Barthélemy *et al.* [10] and Ma *et al.* [15] have studied the ablation of Al in air. They observed that T_e has a special behavior: it drops close to the target side and at the plasma edge and this is attributed mainly to the thermal conduction from the plasma toward the solid target and to the radiative cooling, respectively. The target may gain energy from plasma by either normal electron heat conduction or short-wavelength thermal plasma radiation. For this reason, plasma temperature may decreases at region very close to the target surface. This behavior was not observed in our case and T_e shows a high value at the target surface followed by a continuous decrease as the results observed by Shaikh *et al.* [11] and this is attributed to the fast thermalization, recombination processes and it is in part consumed by hydrodynamical expansion [16].

4.3 Radial dependence of electron density and excitation temperature

The radial structure of n_e, *i.e.* in the direction parallel to the target surface was also studied. The results are presented in Figure (4-7), Figure (4-8) and Figure (4-9) for Ar, N_2 and He, respectively. Recall that for $\tau_d > 0$, the plasma dimension is small and it expands with increasing the time. This explains why the radial dimension differs from 100 to 1000 ns. These measurements were obtained for fixed axial position, at $z = 0$, near the target surface. As expected, the radial distribution is symmetric with respect to the axis. For all gases, n_e is observed at the plume's center ($r = 0$) and it decreases by moving away to the plume's edge. At 760 Torr, n_e is significantly higher in argon. At low pressure (<10 Torr), the radial distribution of n_e flattens, so that the central density is close to the cross-section average value and decreases with decreasing gas pressure.

As mentioned above, n_e decreases with the time and, at 1000 ns (Figure 4-7c, 4-8c and 4-9c), n_e distribution becomes flat even at atmospheric pressure. Quantitatively speaking, the highest value of n_e (3×10^{18} cm^{-3}) is obtained at the earliest time (100 ns) in Ar, at 760 Torr and in the plume center ($r = 0$). This value decreases in N_2 (2.75×10^{18} cm^{-3}) and He (2×10^{18} cm^{-3}). This order is also conserved at a later times, for example, at 1000 ns, n_e (at 760 Torr and at $r = 0$) is ~0.83×10^{18}, 0.8×10^{18} and 0.7×10^{18} cm^{-3} when the ambient gas is Ar, N_2 and

He, respectively. Other published works [15, 17, 18] show, during the ablation of steel and Al samples in air, a continuous decrease of n_e by moving towards the plasma edge similar to that observed by our work.

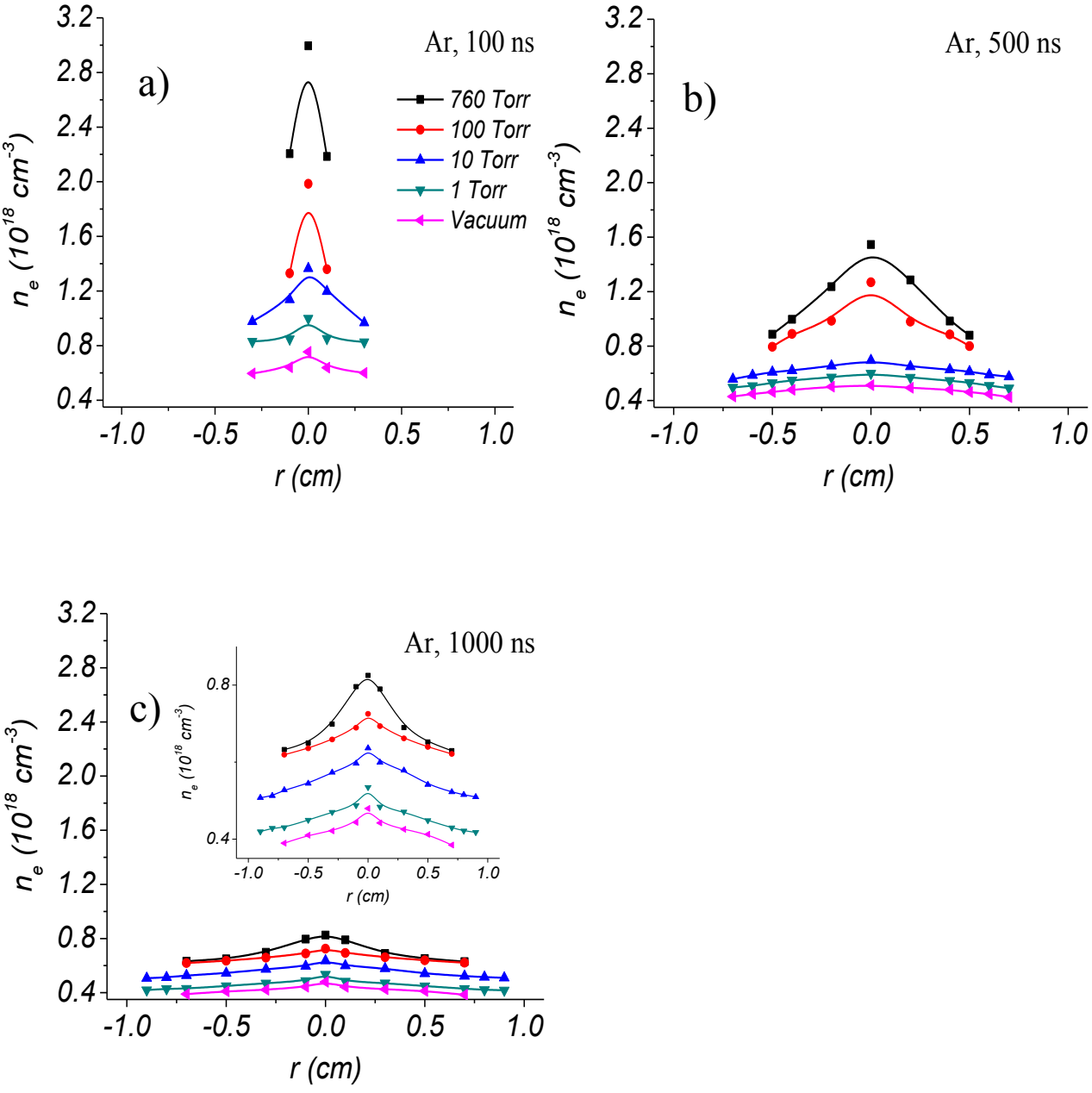

***Figure (4-7)**: Radial variation of n_e in ambient Ar for different pressures (from vacuum up to atmosphere) at a) 100 ns, b) 500 ns and c) 1000 ns. The insets show the same experimental results with an expanded vertical scale.*

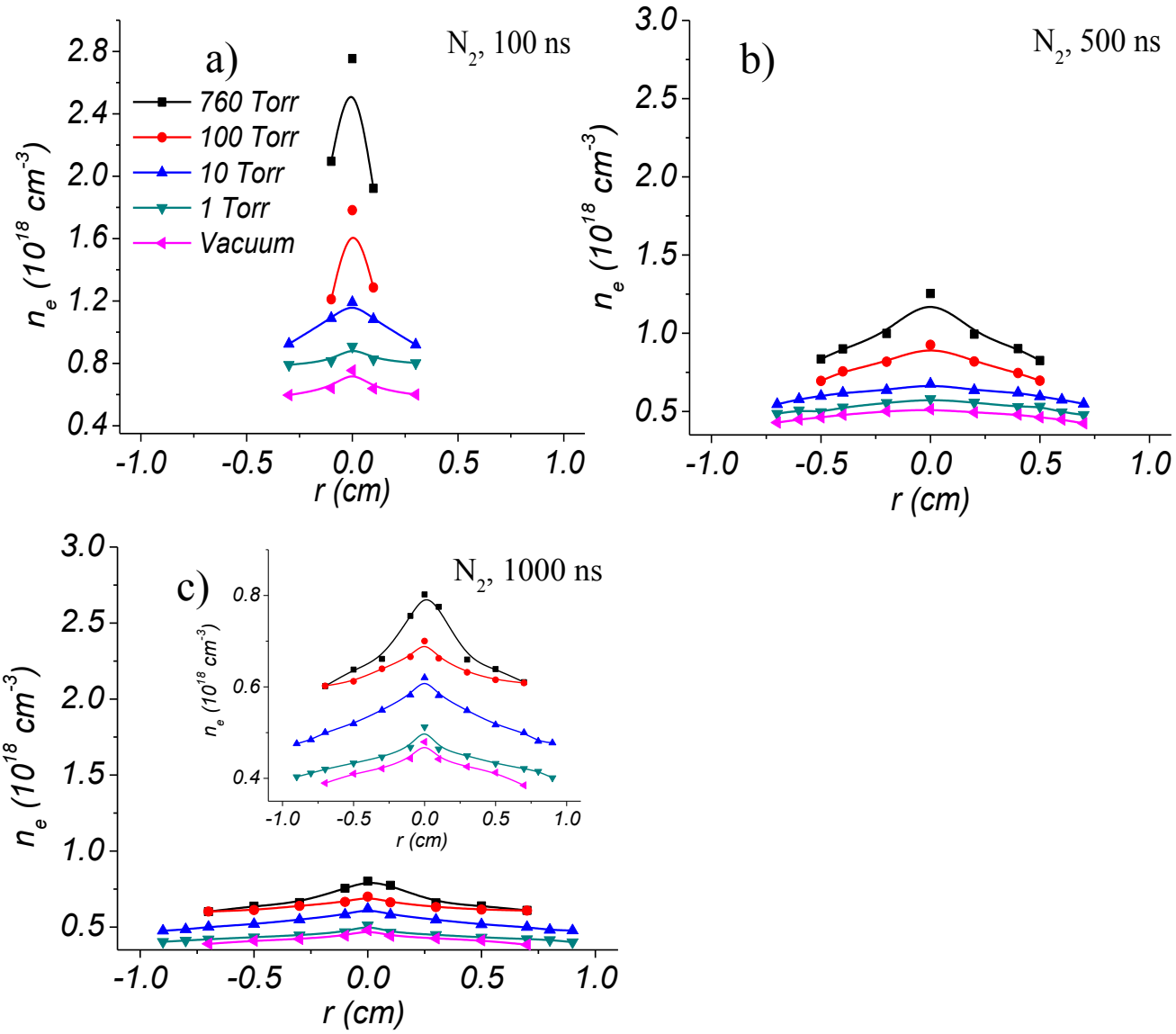

***Figure (4-8)**: Radial variation of n_e in ambient N_2 for different pressures (from vacuum up to atmosphere) at a) 100 ns, b) 500 ns and c) 1000 ns. The insets show the same experimental results with an expanded vertical scale.*

As a partial conclusion, we note that the highest n_e is obtained at 760 torr, when the gas mass is highest and in the position $z = 0$ and $r = 0$. At earlier time (< 100 ns), n_e is higher and depends on the space (axial and radial) position, however, at later time (> 500 ns), n_e decreases and tends to unique value. In other words, the electrons are homogenously distributed in the plume and this is due mainly to collision and diffusion phenomena in the plasma.

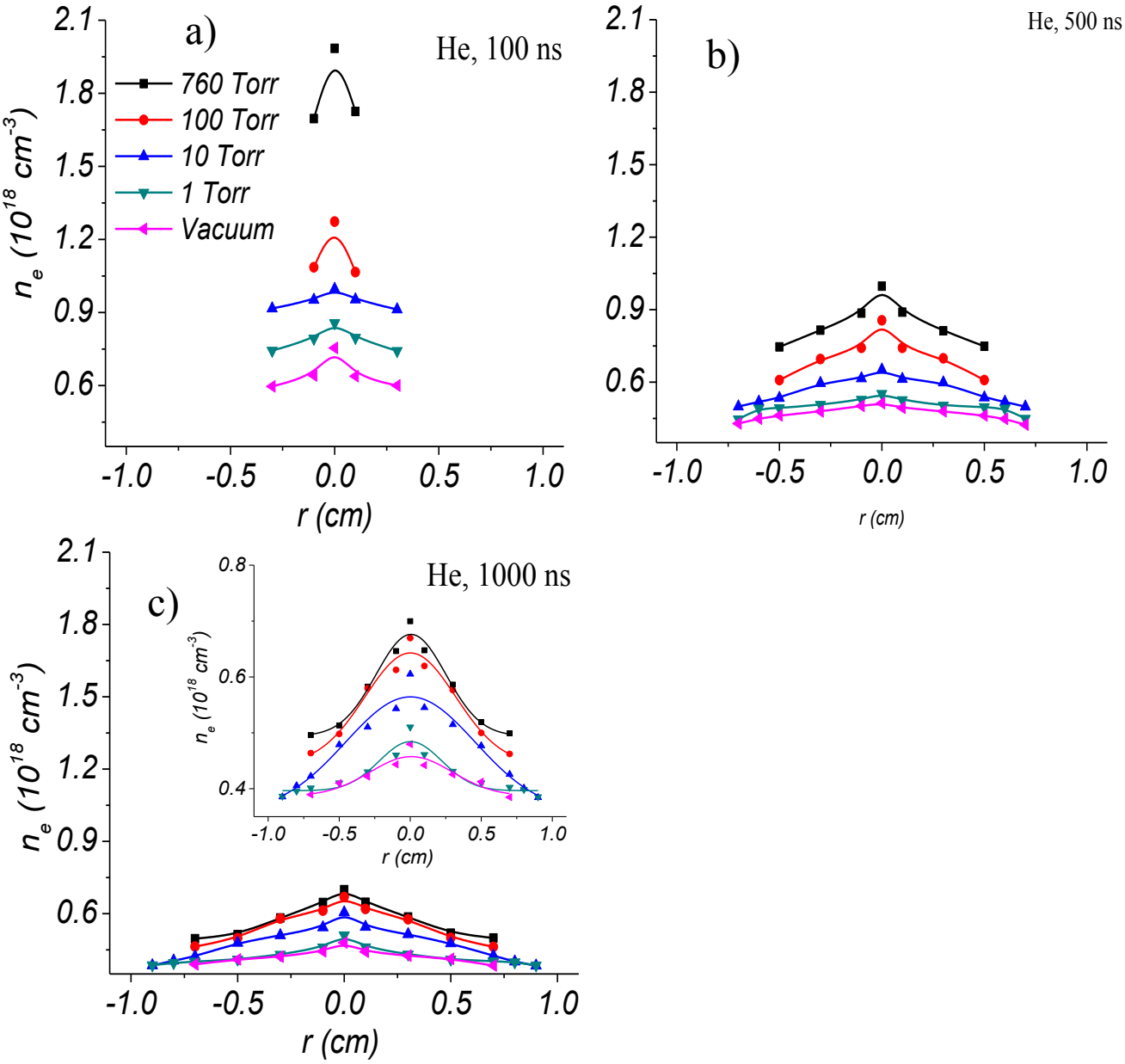

***Figure (4-9)**: Radial variation of n_e in ambient He for different pressures (from vacuum up to atmosphere) at a) 100 ns, b) 500 ns and c) 1000 ns. The insets show the same experimental results with an expanded vertical scale.*

The radial evolution of T_e is also investigated for Ar, N_2 and He ambient gas for pressures starting from vacuum up to atmospheric pressure. As observed for n_e, the radial distribution of T_e is symmetric with respect to the axial axis. The results when the ambient gas is Ar are presented in Figure 4-10 at different time delays. Clearly, T_e decreases as time grows.

T_e is also higher at the center of the plume (*i.e.* $r = 0$ and $z = 0$) and a slight decrease (~500 K or less) is observed by moving towards the plume edge for any time delay and whatever the gas pressure. A similar behavior has been observed by Monge *et al.* [17] between 3 and 8 µs during the ablation of steel sample in air.

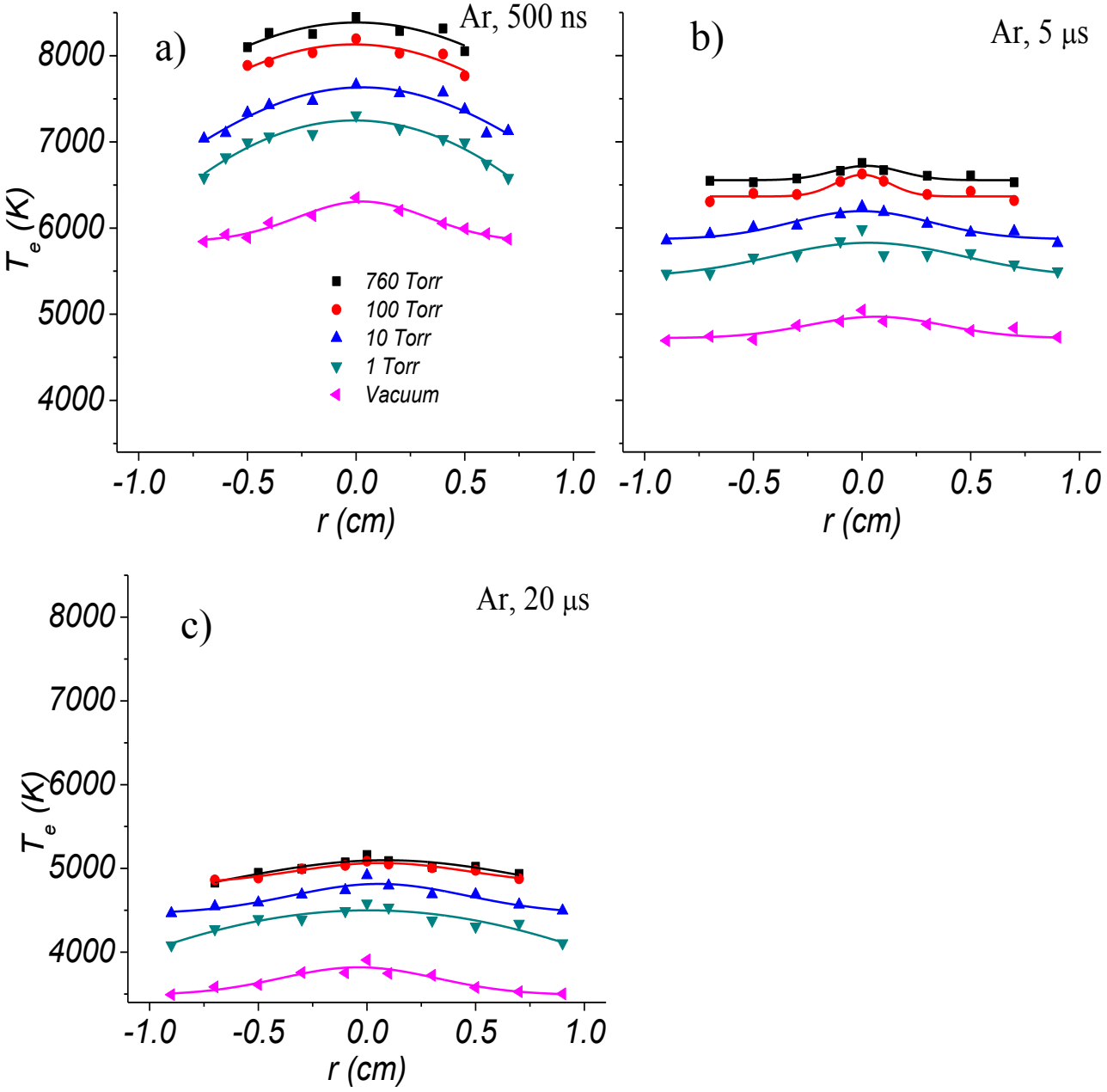

***Figure (4-10)**: Radial variation of T_e in ambient Ar for different pressures (from vacuum up to atmosphere) at a) 500 ns, b) 5 µs and c) 20 µs.*

In the case of N_2 (Figure 4-11) and He (Figure 4-12) ambient gas, a similar evolution can be noted. Unlike the axial variation of T_e, as a first approximation, its radial variation is nearly independent of the surrounding gas. This is very important and means that the plasma kinetics is anisotropic. This behavior was also observed on the plume dynamics as the plasma plume axial length is very sensitive to the ambient gas pressure and composition while its radial dimension is less affected [2, 19].

In fact, the axial variations of T_e are determined by several processes including laser plasma production energy, thermal conduction, plasma expansion, further absorption of the laser beam energy, and plasma cooling. Concerning the radial variation, one can propose two reasons to explain the observed differences. First, the heat loss processes in the radial dimension are significantly different from those in the axial direction. Indeed, by moving towards the radial edge of the plume, the target surface is always present, which facilates heat transfer by conduction etc., and this is not the case in the axial direction. Therefore, an electrostatic sheath interfacing the plasma and the target surface can form.

In contrast, in the axial direction, the plasma is only in contact with the ambient gas, which leads to its rapid cooling. Aguilera *et al.* [12, 20] have developed a deconvolution procedure to transform the measured intensity, integrated along the line of sight, into the radial distribution of emissivity. Their 2D temperature map (Figure 5b in Ref. 10) shows that, near the target surface, the radial variation is not significant which is in agreement with our results. However, the same map shows that by moving away from the target surface, the radial variation becomes similar to the axial one. This supports our previous assumption that the presence of the wall (the target) modifies the plasma kinetics. Moreover, the same authors show that the spatial distribution of (iron) atoms and ions are different. Indeed, the ion distribution is elongated in the axial direction where the atom distribution is rather elongated in the radial direction.

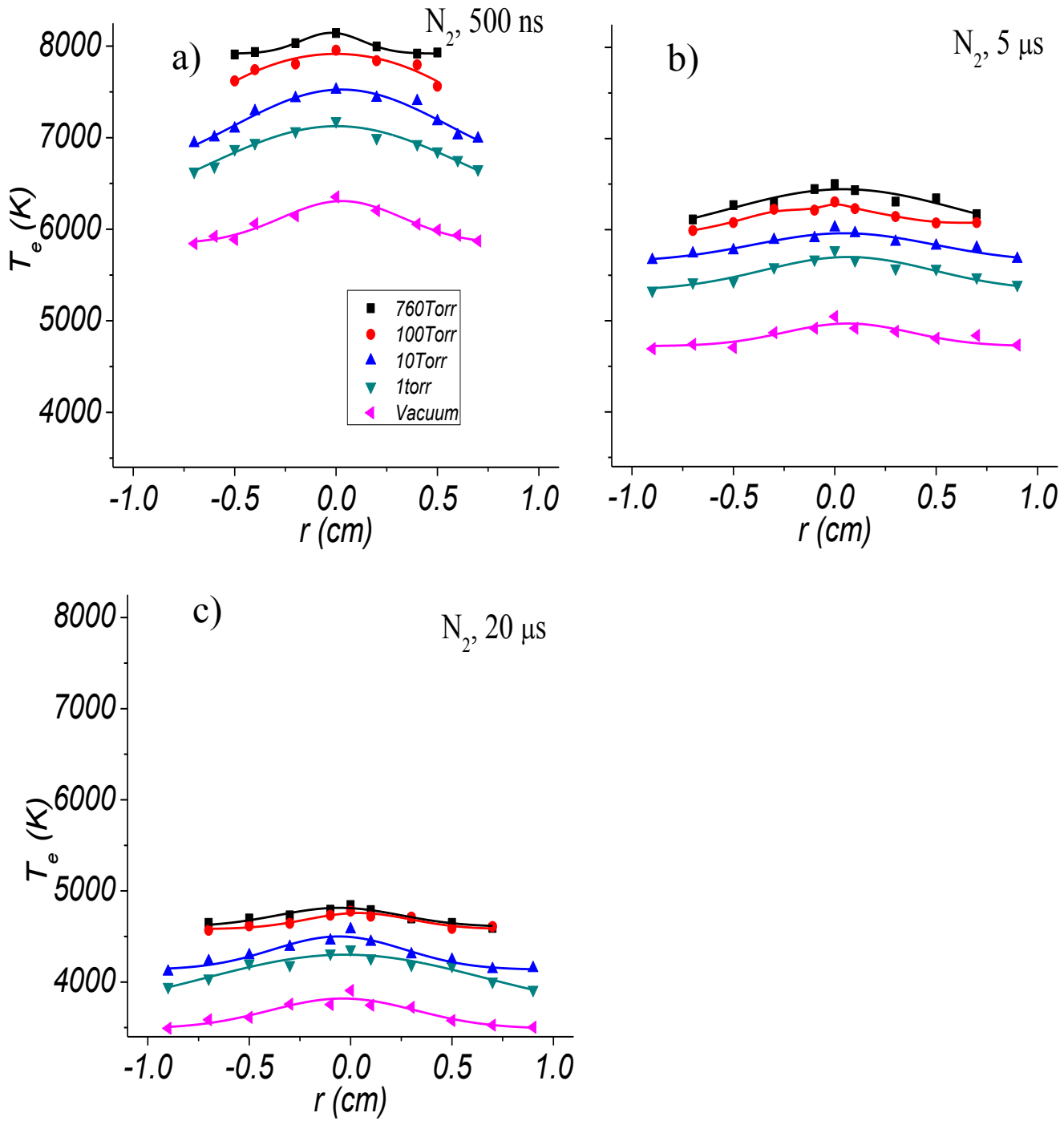

***Figure (4-11)**: Radial variation of T_e in ambient N_2 for different pressures (from vacuum up to atmosphere) at a) 500 ns, b) 5 µs and c) 20 µs.*

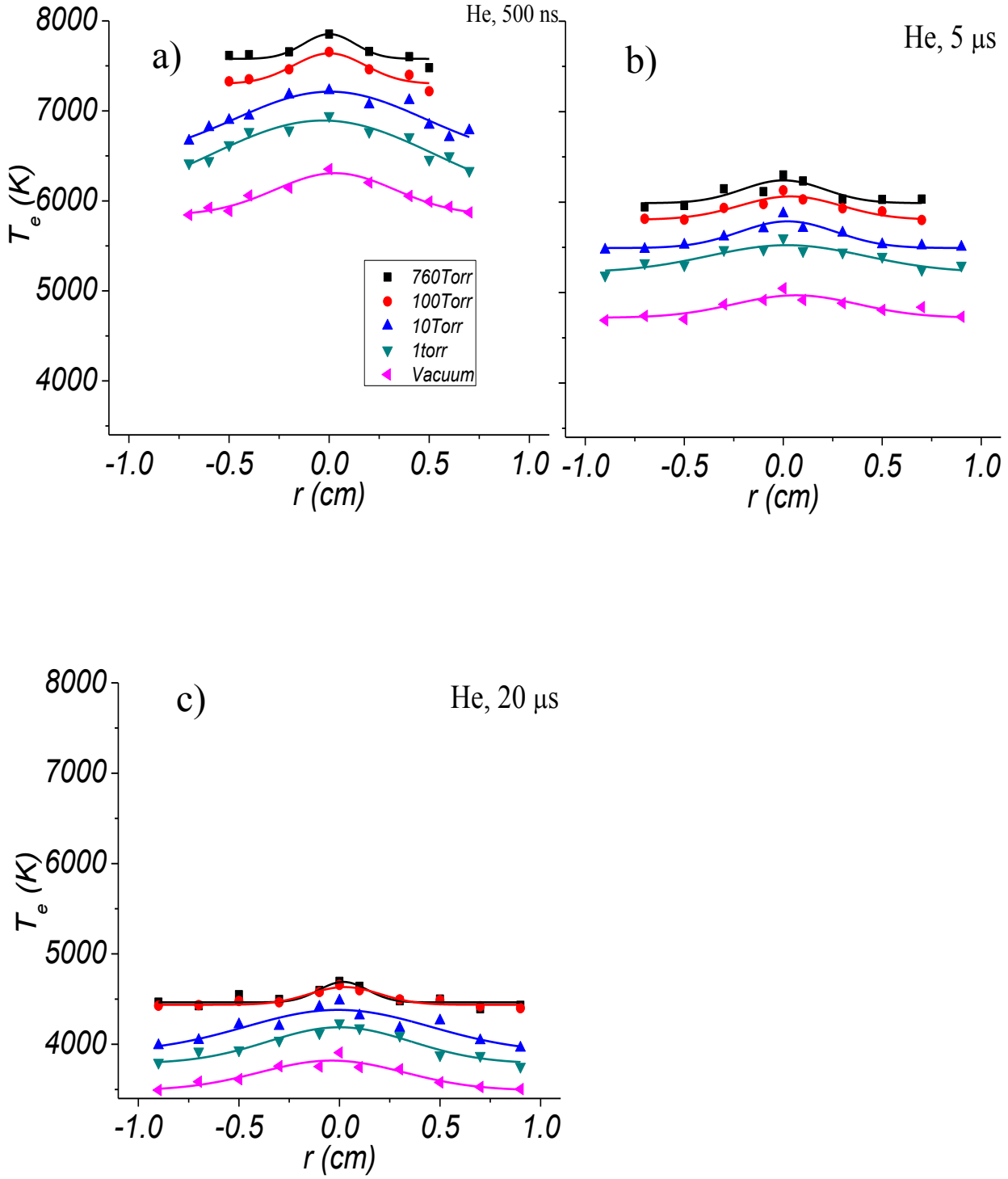

***Figure (4-12)**: Radial variation of T_e in ambient He for different pressures (from vacuum up to atmosphere) at a) 500 ns, b) 5 µs and c) 20 µs.*

4.4 Conclusion

In this chapter, we studied Al plasma plume characteristics induced by 10 ns XeCl excimer laser at 308 nm. On the one hand, the wavelength-resolved profile of Al^+ ion line at 281.6 nm has been studied in details to extract n_e through the Stark broadening induced by the dynamic micro-electric field created by the charged species present in the environment of the emitting ion. On the other hand, the emission of iron spectrum has been used to determine T_e through the Boltzmann plot method. n_e is a maximal in the plasma plume center at atmospheric pressure and for high mass gas species. This is attributed to the confinement of the plasma by the surrounding gas. By moving away, perpendicularly to the target surface, n_e decreases progressively due mainly to the recombination processes. A similar evolution of the temperature has been observed along the axial direction. However, by moving from the plume center to its edge, T_e does not present a strong change. The different behavior, between the axial and radial directions, has been reported to the difference in the plasma kinetics in these directions, in particular, the presence of the wall (target surface) in the radial direction.

4.5 References

[1] M.S. Dawood and J. Margot, AIP Advances **4**, 037111, 2014.

[2] M. S Dawood, A Hamdan and J Margot, submitted to J. Phys. B: At., Mol. Opt. Phys., 2015.

[3] J. Bonse, J. Krüger, S. Höhm and A. Rosenfeld, Journal of Laser Applications, **24**(4), 042006, 2012.

[4] B.K. Nayak and M.C. Gupta, Optics and Lasers in Engineering, **48**(10), 940–949, 2010.

[5] S. Moussa, V. Abdelsayed and M. Samy El-Shall, Chem. Phys. Lett., **510**(4), 179–184, 2011.

[6] C. Aragón and J.A. Aguilera Spectrochim. Acta, Part B, **63** 893–916, 2008.

[7] M.S. Tillack, D.W. Blair and S.S. Harilal, Nanotechnology **15**(3), 390, 2004.

[8] V. Narayanan and R.K. Thareja, Appl. Surf. Sci. **222**(1), 382–393, 2004.

[9] A. De Giacomo, M. Dell'Aglio, R. Gaudiuso, G. Cristoforetti, S. Legnaioli, V. Palleschi and E. Tognoni, Spectrochim. Acta, Part B, (9), 980–987, 2008.

[10] O. Barthélemy, J. Margot, M. Chaker, M. Sabsabi, F. Vidal, T.W. Johnston, S. Laville and B. Le Drogoff, Spectrochim. Acta, Part B, **60**(7), 905–914, 2005.

[11] N.M. Shaikh, S. Hafeez, B. Rashid and M.A. Baig, The European Physical Journal D-Atomic, Molecular, Optical and Plasma Physics **44**(2), 371–379, 2007.

[12] J.A. Aguilera and C. Aragón, Spectrochim. Acta, Part B , (12), 1861–1876, 2004.

[13] K.J. Grant and G.L. Paul, Appl. Spectrosc., **44**(8), 1349–1354, 1990.

[14] Y.I. Lee, K. Song, H.K. Cha, J.M. Lee, M.C. Park, G.H. Lee and J. Sneddon, Appl. Spectrosc. **51**, 959–964, 1997.

[15] Q.L. Ma, V. Motto-Ros, W.Q. Lei, M. Boueri, X.S. Bai, L.J. Zheng, H.P. Zeng and J. Yu, Spectrochim. Acta, Part B, **65**(11), 896–907, 2010.

[16] S. C. Singh, H. B. Zeng, C. Guo & W. Cai, eds. Nanomaterials: processing and characterization with lasers, John Wiley & Sons, 2012.

[17] E.M. Monge, C. Aragón C. and J.A. Aguilera, Appl. Phys. A, **69**(1), S691–S694, 1999.

[18] W.F. Luo, X.X. Zhao, Q.B. Sun, C.X. Gao, J. Tang and W. Zhao, Nuclear Instruments and methods in physics Research A **637**, S158–S160, 2011.

[19] S.S. Harilal, C.V. Bindhu, M.S. Tillack, F. Najmabadi and A.C. Gaeris, Appl. Phys. A, **93**(5), 2380–2388, 2003.

[20] J.A. Aguilera, C. Aragón and J. Bengoechea, Appl. Opt., **42**(30), 5938–5946, 2003.

CHAPTER 5:

Influence of surrounding gas, composition and pressure on plasma plume dynamics of nanosecond pulsed laser-induced aluminum plasmas

Chapter 5:

Influence of surrounding gas, composition and pressure on plasma plume dynamics of nanosecond pulsed laser-induced aluminum plasmas[1]

5.1 Introduction

In this chapter, we present a comprehensive study of the plume dynamics of plasmas generated by laser ablation of an aluminum target. The effect of both ambient gas composition (helium, nitrogen or argon) and pressure (from ~5×10^{-7} Torr up to atmosphere) is studied. The time- and space- resolved observation of the plasma plume are performed from spectrally integrated images using an intensified Charge Coupled Device (iCCD) camera. The iCCD images show that the ambient gas does not significantly influence the plume, as long as the gas pressure is lower than 20 Torr and the time delay below 300 ns. However, for pressures higher than 20 Torr, the effect of the ambient gas becomes important, the shortest plasma plume length being observed when the gas mass species is highest.

On the other hand, space- and time- resolved emission spectroscopy of aluminum ions at λ= 281.6 nm are used to determine the Time-Of-Flight (TOF) profiles. The effect of the ambient gas on the TOF profiles and therefore on the propagation velocity of Al ions is discussed. A correlation between the plume expansion velocity deduced from the iCCD images and that estimated from the TOF profiles is presented. The observed differences are attributed mainly to the different physical mechanisms governing the two diagnostic techniques.

[1] This chapter is part of article: Mahmoud S. Dawood, Ahmad Hamdan and Joelle Margot, submitted to Journal of Physics B: Atomic, Molecular and Optical Physics (2015).

5.2 Plasma plume dynamics

When the laser intensity exceeds the target ablation threshold, the laser induces evaporation and ionization of the target material creating a plasma, called *plasma plume*, above the target surface. The species (atoms, molecules and ions) undergo collisions in the high-density region near the target surface, forming the so-called Knudsen layer, leading to a highly directional expansion perpendicular to the target [1]. The interaction of the laser beam with the evaporating material leads to the formation of isothermally expanding plasma until the end of the laser pulse (~10 ns in our case). Once the laser pulse ends, an adiabatic expansion of the plasma occurs, where the temperature can be related to the plasma dimension.

In order to study the dynamics of the plasma plume as a function of ambient gas composition and pressure, it is useful to first understand its dynamics in vacuum. The 2D temporal evolution of the plasma plume in vacuum with iCCD integration time of 10 ns is depicted in Figure (5-1). All frames are sized to present the same space scale and a zoom on the plasma plume at 50 ns is shown also at the right of the figure.

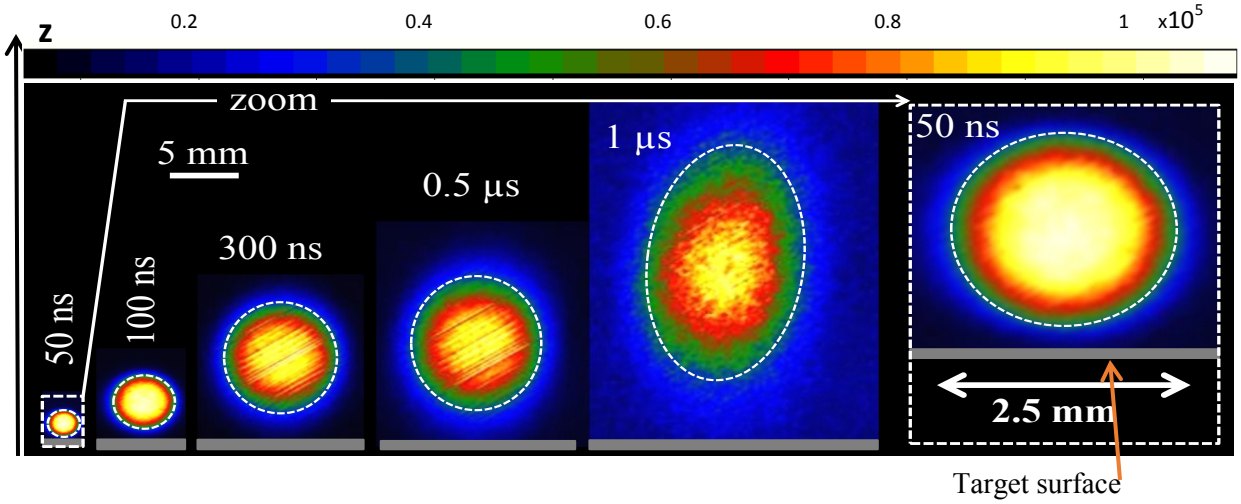

***Figure (5-1)**: iCCD images of the plasma plume in vacuum (5×10^{-7} Torr) at 50, 100, 300, 500 and 1000 ns. A zoom of the plasma plume at 50 ns is shown at the right of figure.*

The plasma plume volume increases with time and reaches a maximum at about 1 µs. At 2 µs, the plasma plume disappears from the region scanned. The plasma shape significantly varies with time. From ignition up to ~200 ns, it remains quite spherical. This means that the

radial (direction parallel to the target) and axial (the direction perpendicular to the target) expansion rates are similar in this interval of time (isotropic expansion). This is due mainly to the homogeneous heating of the plume by the energetic species (electrons and ions) which leads to a rapid expansion in a large cone angle (*i.e.* spherical symmetry) over this time scale [2]. However, at a later time (t > 200 ns), the axial dimension (denoted the plasma plume length, PPL, in the following) becomes larger than the radial dimension, which means that the expansion has become anisotropic. This is rather due to the diffusion of electrons across the focal spot boundary allowing an expansion of the plasma plume length along the axial direction [3]. This result is also supported by the work of Singh and Narayan [4]. Indeed, they explain that the forward directed nature of the laser evaporation process results from anisotropic expansion velocities of the different species (electrons, atoms and ions), which are mainly controlled by the initial dimensions of the expanding plasma.

The plume-contour obtained in vacuum (indicated by a white-dashed line in Figure 5-1) is superimposed with the plasma plume images in the subsequent figures. The 2D time evolution of the plasma plume in helium gas for pressures of 0.1 and 100 Torr is presented in Figures (5-2a) and (5-2b), respectively. At low helium pressure, the plasma plume shape is similar to that obtained in vacuum, but the plasma plume length (PPL) is slightly smaller. At high helium pressure, the PPL is significantly reduced while the radial dimension remains unchanged.

Similar features are observed when the ambient gas nitrogen and argon as shown in Figures (5-3) and (5-4), respectively. Moreover, one notes that increasing the gas mass leads to an important PPL compression, while the radial dimension is weakly influenced, which will be shown later in Figure (5-5). In fact, a higher mass density of the ambient gas results in a perpendicular force to the target which induces deceleration only in the axial direction [5]. Therefore, at higher mass gas, the plasma plume shape keeps its spherical shape at low pressure until the end of the plasma emission while, at high pressure and later time (*e.g.* 1µs), the plume slightly flattens (see Figure 5-3b and 5-4b at 1µs). In other words, the higher gas mass balances the axial expansion of the plume to result finally either in a sphere or in an ellipsoidal shape, as seen in Figures (A-10) to (A-13) in appendix III. In conclusion, the plasma plume anisotropic expansion strongly depends on the velocities of the different species present in the plume, which in turn depend on the gas composition and pressure.

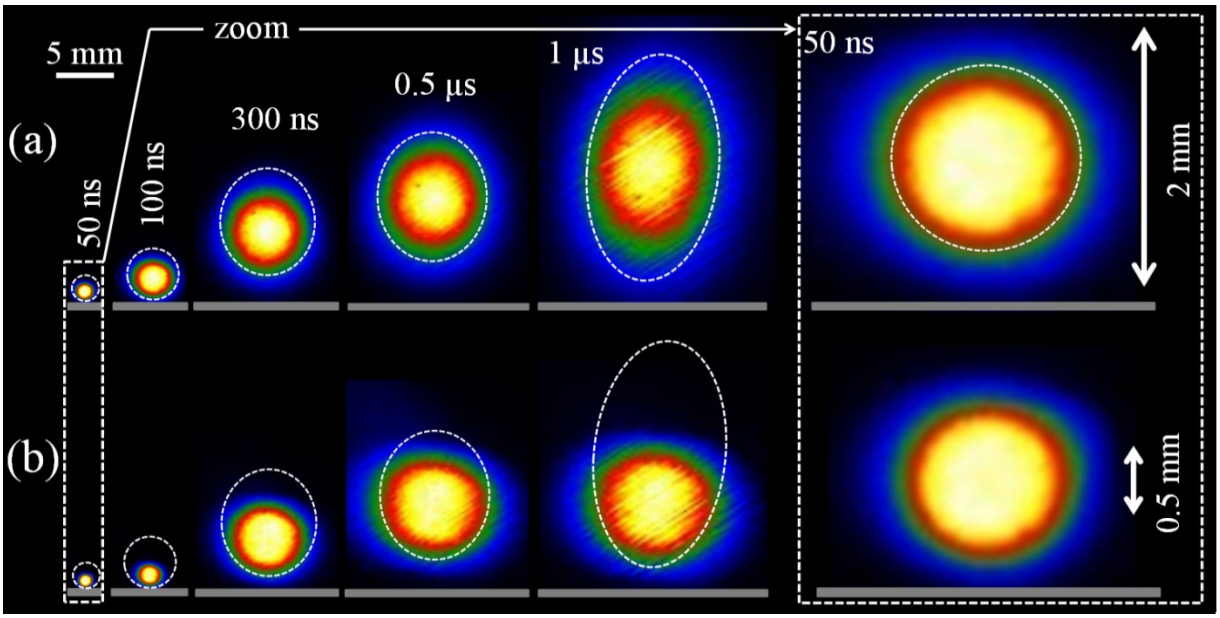

***Figure 5-2**: iCCD images of the plasma plume in helium ambient gas at a) 0.1 Torr and b) 100 Torr. Zoom of the plasma plume at 50 ns is shown at the right of the figure. The white-dashed contours correspond to the plasma plume shape observed in vacuum for the same time delay.*

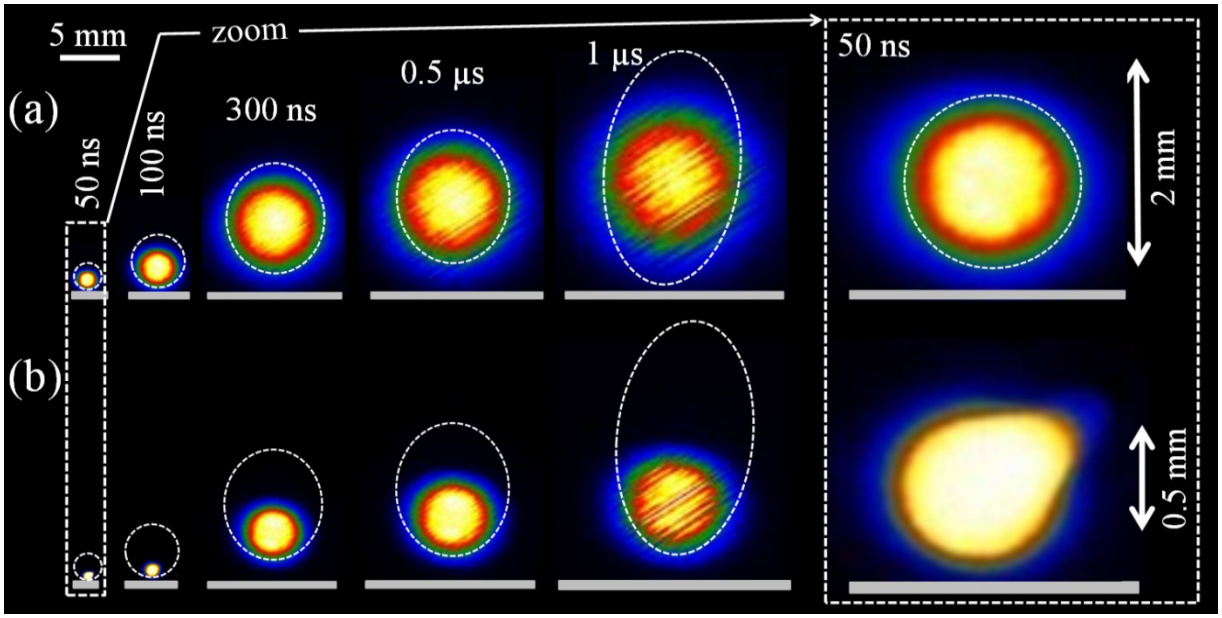

***Figure (5-3)**: iCCD images of the plasma plume in nitrogen at a) 0.1 Torr and b) 100 Torr. A zoom of the plasma plume at 50 ns is shown at the right of the figure. The white-dashed contours correspond to the plasma plume shape observed in vacuum.*

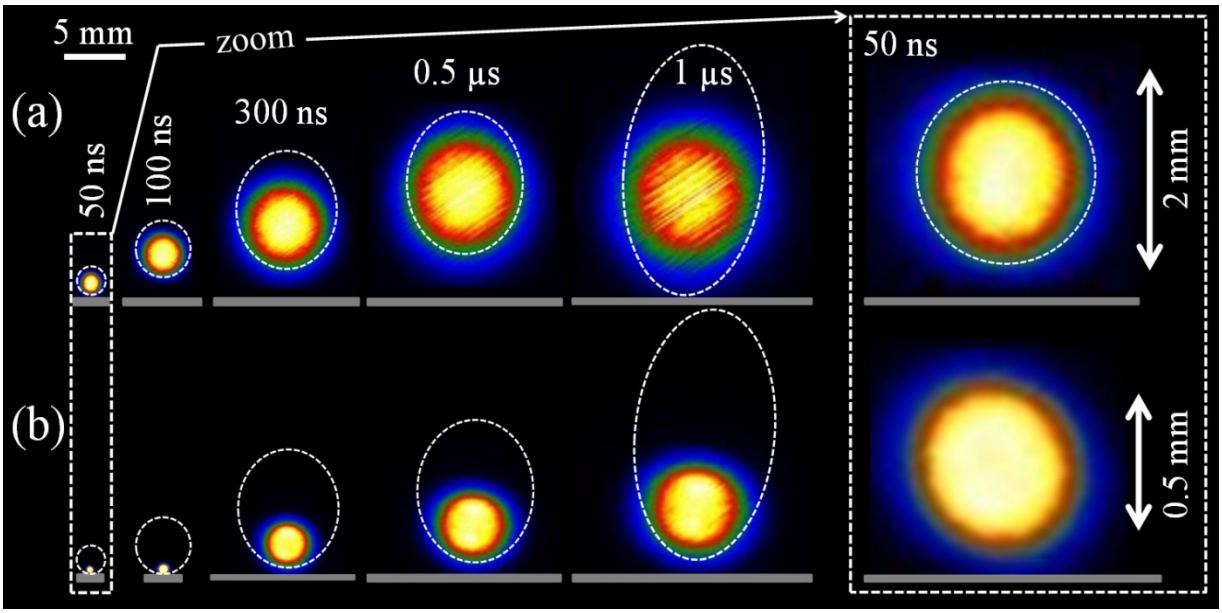

***Figure (5-4)**: iCCD images of the plasma plume in argon ambient gas at a) 0.1 Torr and b) 100 Torr. A zoom of the plasma plume at 50 ns is shown at right of the figure. The white-dashed contours correspond to the plasma plume shape obtained in vacuum.*

By processing the iCCD images, we can deduce the time evolution of the PPL for different gas compositions and pressures. Figure (5-5) shows the time evolution of the PPL for different gas pressures in helium (Figure 5-5a), nitrogen (Figure 5-5b) and argon (Figure 5-5c). Over the whole gas pressure range and composition, the PPL increases with time, the longer PPL corresponds to the lower pressure and for lighter gases (*e.g.* at 100 Torr, $PPL_{argon} < PPL_{nitrogen} < PPL_{helium}$). Therefore, in pulsed laser deposition of thin films, the thickness of the film and indeed the distance between the target surface and the substrate are highly dependent on the gas composition. Thus, gas of higher mass density like Ar exerts confinement to the plasma plume and condenses them in the form of nanomaterial. However, light mass density, such as, He requires a larger target to substrate distance or higher background pressure to deposit maximum thickness of the film compared to heavier gases.

This can be explained considering that the interaction between the plume species and the ambient gas can produce excitation and ionization of gas atoms and molecules, as observed by several authors [6, 7]. Therefore, the dynamics of the plasma plume are expected to depend on the ionization, excitation and dissociation energy of the atoms and molecules. Another mechanism can be involved to explain the dependence of the PPL on the gas

composition. It relies on the thermal conductivity ($k_{thermal}$) of the gas. It is indeed well known that the gas temperature is several thousands of Kelvins in the plasma [8-10]. When the plume interacts with a colder gas, the expansion is expected to depend on the thermal conductivity of the ambient gas [11]. The thermal conductivity of the gases used in this study is in the following order of importance $k_{Ar} < k_{N_2} < k_{He}$ [12]. In particular, helium conducts heat faster than nitrogen and argon. Therefore, we expect that the expansion be the most important in helium for the same pressure [13].

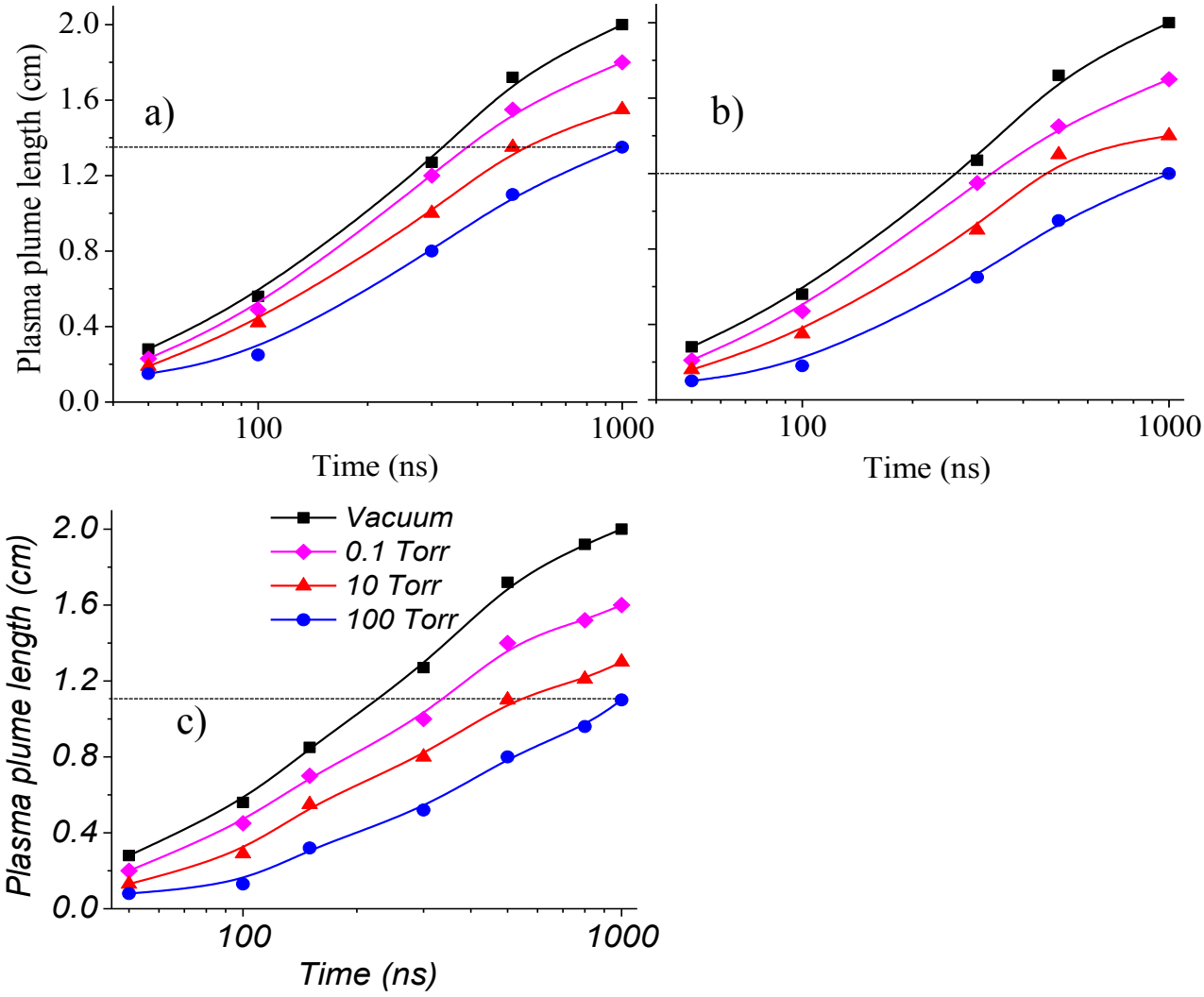

***Figure (5-5)**: Time evolution of the plasma plume length (PPL) in a) helium, b) nitrogen and c) argon at different pressures: vacuum (5×10^{-7} Torr), 0.1, 10 and 100 Torr.*

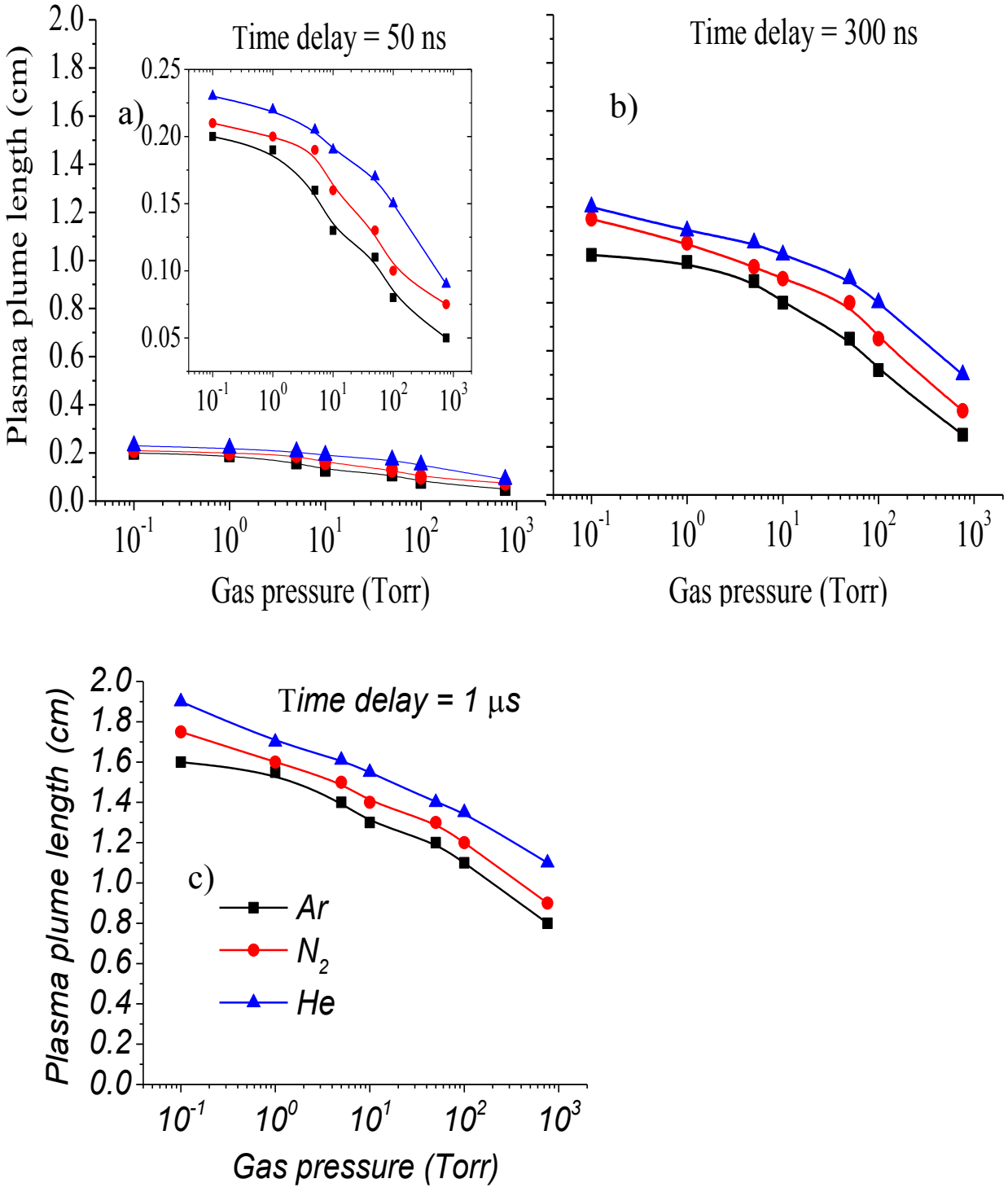

***Figure (5-6)**: Variation of the plasma plume length (PPL) as a function of the pressure in helium, nitrogen and argon at different time delays: a) 50 ns, b) 300 ns and c) 1μs.*

The influence of the pressure on the PPL was studied for the three gases as presented in Figure (5-6) for three different times, 50 ns (Figure 5-6a), 300 ns (Figure 5-6b) and 1 µs (Figure 5- 6c). It is observed that the PPL decreases by increasing the pressure for any gas. At 50 and 300 ns, the PPL decreases only by ~25% when the gas pressure increases from vacuum up to atmospheric pressure. However, at 1 µs, the decrease reaches ~50%. This time dependence is mainly related to the pressure in the plasma plume. Indeed, up to ~100 ns, the pressure in the plume is so high (several tens of bars typically) [14] as compared to the ambient gas pressure that the later does not influence the expansion dynamics. After ~100 ns, the pressure inside the plasma plume undergoes relaxation towards much lower value [10, 15]. At this point, the PPL then depends on the ambient pressure.

From ignition to 200 ns (*i.e.* PPL < 1 cm), the axial plasma expansion can be assumed to vary linearly with time (as shown in Figure 5-5). One can therefore estimate the average expansion velocity of the plasma plume. These results are presented in Figure (5-7). The highest expansion velocity is obtained in vacuum and it decreases with increasing the ambient gas pressure. In addition, in the presence of a gaseous environment, the higher mass leads to the lower expansion velocity and conversely. Moreover, one can identify two time scales. A slow phase is observed for pressures lower than about 1 Torr and a faster one beyond. As mentioned before, in the interval time (*i.e.* t < 200 ns) considered, the pressure in the plasma plume is so high that it is the main factor controlling the expansion. When the pressure of the ambient gas is significant as compared to that in the plasma plume, the dynamics of the latter are affected by the ambient gas, which occurs at about 100 Torr or at time greater than 200 ns.

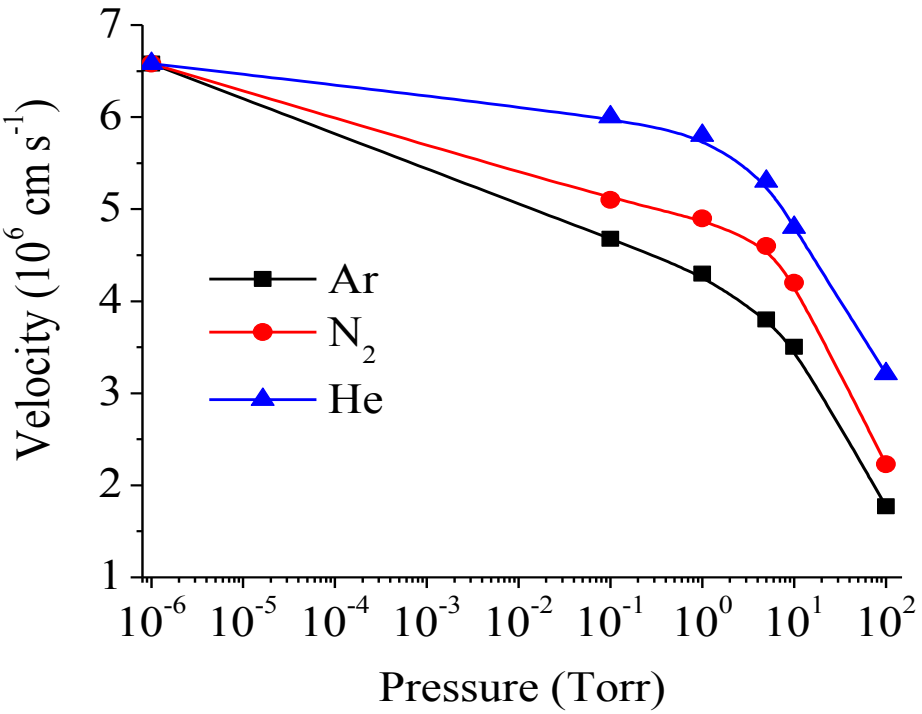

***Figure (5-7)**: Expansion velocity of the plasma plume derived from iCCD images as a function of pressure in helium, nitrogen and argon at delay time 200ns.*

5.3 Aluminum ion dynamics: Time-Of-Flight

In this section, we focus on the results of optical emission spectroscopy, in particular the Time-Of-Flight (TOF) of the Al II species. The aim of these measurements is to determine the flight velocity of the Al II species in the plume and to correlate them to the expansion velocity obtained from the iCCD images. The emission of Al ions at $\lambda = 281.6$ nm ($3s4s\ ^1S_0 \rightarrow 3s3p\ ^1P_1$) was chosen for several reasons. First, the aluminum ions ejected from the target are a convenient probe of the ionization front's propagation. Second, the line profile associated with this transition is well defined as there is no ovelap with other lines. Moreover, the high energy of its lower level (7.4 eV) and its small transition probability (3.6×10^8 s^{-1}) [16] strongly reduce self-absorption [17]. In this study, only the maximum line intensity is used to monitor relative plasma changes.

The temporal evolution of the relative intensity of Al II emission in vacuum is presented in Figure (5-8) at three axial positions (4, 8 and 10 mm) from the target surface. The emission intensity reaches a maximum at a given time that increases with the position from the

target. This is explained considering that the plume is moving from the target as observed from the iCCD photos. At 4 mm from the target surface, the line emission is localized in a narrow region. This indicates that the aluminum ions have a narrow velocity distribution when they come out of the target near the surface. The full width at half maximum (FWHM) of the emission intensity is ~80 ns at 4 mm from the target and it increases to ~260 and ~300 ns at 8 and 10 mm from the target. This means that the Al ions undergo relaxation of their velocity due mainly to collisions. Note that the average velocity of the Al ions can be obtained by measuring the time at which the emission intensity reaches its maximum value for different axial positions. For example, at 4 mm from the target surface, the emission intensity reaches its maximum after 60 ns, which corresponds to a velocity of ~6.6×10^6 cm s^{-1}. This value is in agreement with those found in other works, e.g. 7.6×10^6 cm s^{-1} for the fastest plume expansion and 2.5×10^6 cm s^{-1} for the slowest one [18, 19].

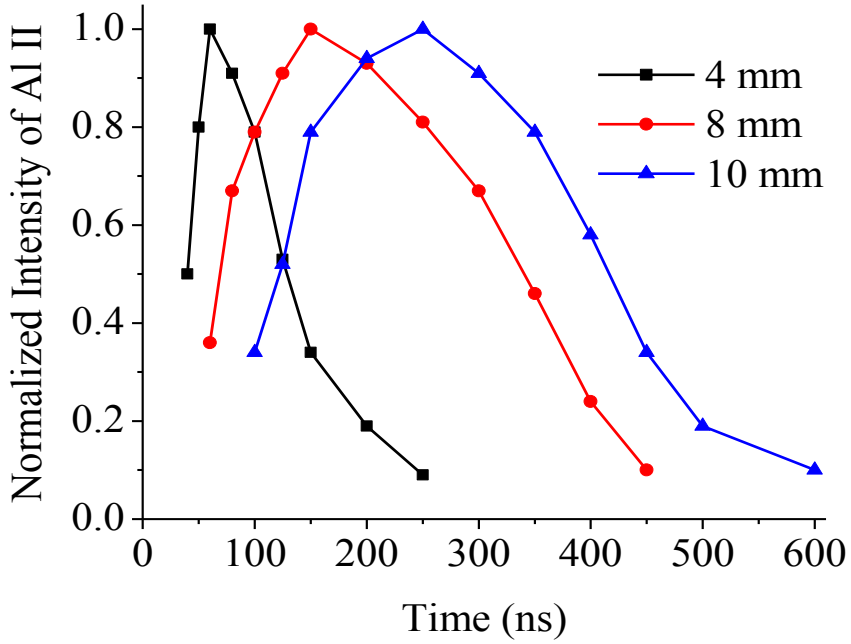

***Figure (5-8)**: Temporal evolution of the normalized intensity of Al II emission (at 281.6 nm) in vacuum at distances of 4, 8 and 10 mm from the target surface.*

We present in Figures (5- 9a to 9f) the TOF profiles obtained at three different axial positions for different gases and at two pressures. In each figure, the profiles were compared with that obtained in vacuum (dashed line). It is observed that whatever the axial position and the gas pressure, the intensity of the TOF profile reaches its maximum earlier when the

background gas changes from vacuum, to helium, to nitrogen and to argon, which indicates a lower ion velocity. As an example, Figure 5-9d shows that the maximum occurs at ~152 ns in vacuum while it occurs at 350, 400 and 500 ns in He, N_2 and Ar, respectively. A similar behavior is observed for other distances and pressures. In other words, when the ambient gas is lighter, the velocity of Al ions increases. Such a behavior is expected because the thermalization of the ions with the ambient medium gets slower when the mass of the collision partner gets smaller [20].

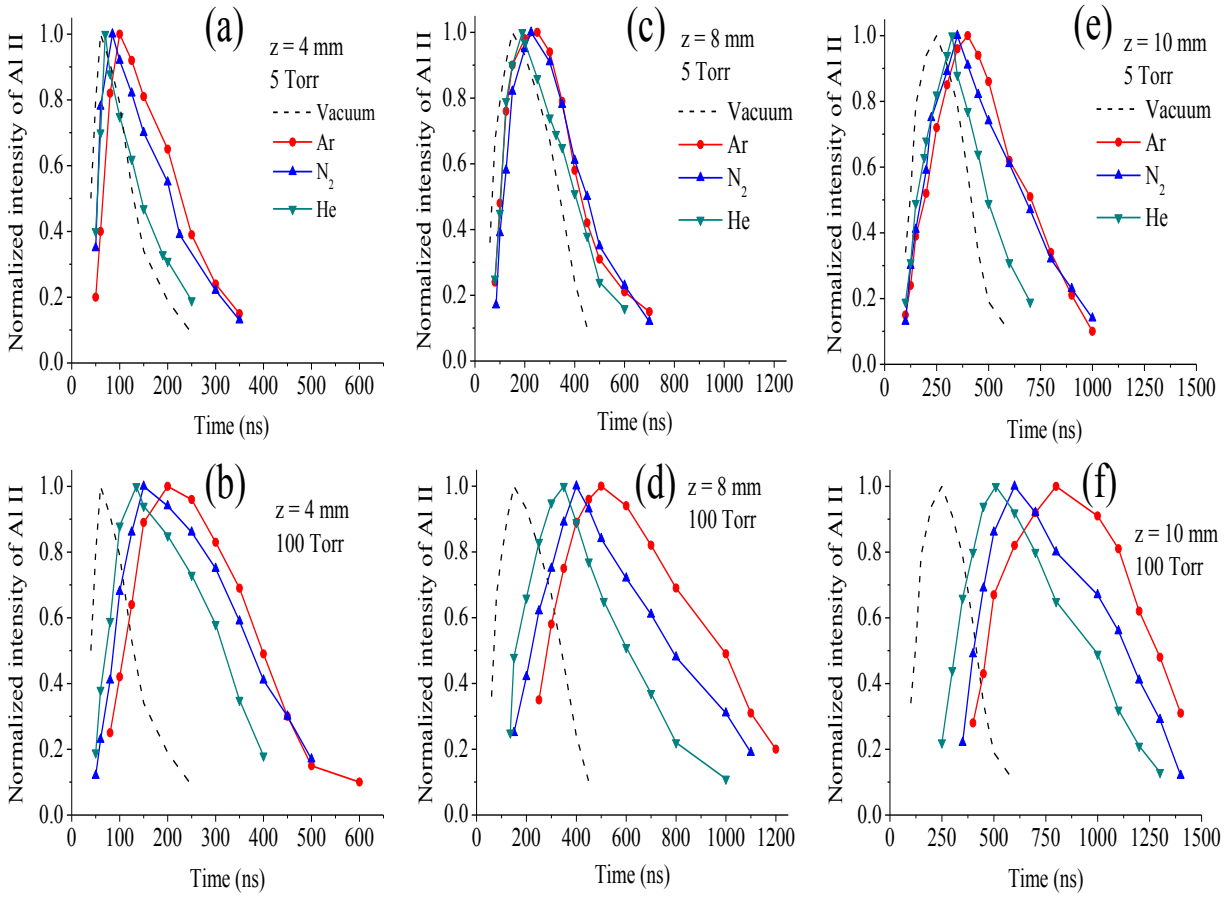

***Figure (5-9)**: Temporal evolution of the normalized intensity of Al II emission (at 281.6 nm) in different ambient gases, pressures and distances from the target surface: a) 5 Torr and 4 mm, b) 100 Torr and 4 mm, c) 5 Torr and 8 mm, d) 100 Torr and 8 mm, e) 5 Torr and 10 mm and f) 100 Torr and 10 mm.*

At 4 and 8 mm from the target surface (Figures 5- 9a & 9d), we also note a significant asymmetry of the TOF profile increases for both pressures investigated. This asymmetry can be defined by the difference in the profile 'tail shape' on each side of the maximum. However,

at 10 mm from the target surface (Figures 5- 9e and 9f), the distribution becomes more symmetric. This change looks more pronounced for the heavier species (argon) and for higher pressures (*i.e.* 100 Torr).

It is worth mentioning that in the region where the intensity is increasing, all the profiles are somewhat similar whatever the gas composition and pressure. This means that the creation processes of the Al ions only weakly depend on the ambient gas [21]. This is expected because the ion creation mechanism should only depend on the laser wavelength and on the fluence, which are both constant in the present study. However, after reaching its maximum, the plasma emission then becomes governed by other factors, such as collisions and recombination that are functions of the environment gas and pressure. This explains why the right tail of the profile changes with the gas composition and pressure.

The average velocity of the Al ions can be estimated using the method mentioned above. At 5 Torr near the target surface (4 mm), the velocity is estimated to be ~4-6×10^6 cm s^{-1}. At 8 mm from the target surface, it decreases to ~1.0- 1.2×10^6 cm s^{-1} independently of the gas composition. However, at higher pressure (*i.e.* 100 Torr), the dependence of the velocity on the ambient gas composition can no more be neglected. At 8 mm from the target surface, it is higher in helium (~3×10^6 cm s^{-1}) than in argon (~2×10^6 cm s^{-1}). At 10 mm from the target surface, the velocity is strongly reduced and the dependence on the ambient gas composition is then more important. For instance, the velocity in helium is ~0.8×10^6 cm s^{-1} while it is ~0.5×10^6 cm s^{-1} in argon.

These values of plume velocity in different ambient gas are in good agreement with other published values [17, 22-25]. For example, Abdellatif *et. al.* [17], stated that the velocity of the Al plasma plume's front found to be 2.5×10^6 cm s^{-1} and 1.2×10^5 cm s^{-1} in vacuum and air respectively. Wang *et. al.* [23], calculated the N^+ ions velocity in the titanium plume and it has a most probable value of 5×10^6 cm s^{-1}. In N_2 ambient atmosphere, Sharma *et. al*. [24], estimated the velocity of Al plume to be in the range 3 ×10^6 cm s^{-1}. Finally, Nica *et. al.* [25] studied the Al plume dynamics in vacuum and he estimated the plume velocity to be 4.66×10^6 cm s^{-1}.

It is interesting to compare the velocity values derived from the iCCD images and from TOF measurements. For this purpose, we have plotted in Figure (5-10) the pressure dependence of the velocity derived from these two diagnostics at 4 mm from the target surface

for various gases. In all cases, the expansion velocity obtained from the iCCD images is slightly lower than the velocity of the aluminum ions calculated from the TOF measurements. The difference between these values may be understood by considering the different physics controlling the two diagnostic techniques. The velocity obtained from the TOF measurements mainly represents singly ionized aluminum atoms undergoing a specific atomic transition as they travel away from the target, resulting in radiation of an isolated wavelength. TOF is therefore the signature of a specific population. In contrast, the iCCD images capture broadband emission (~200-900 nm) resulting from multiple atomic transitions (originating in particular from Al I and Al II species) and continuous radiation (originating from blackbody radiation, Bremsstrahlung, and electron-ion recombination). As a consequence, ICCD images constitute some average over multiple populations of different characteristics.

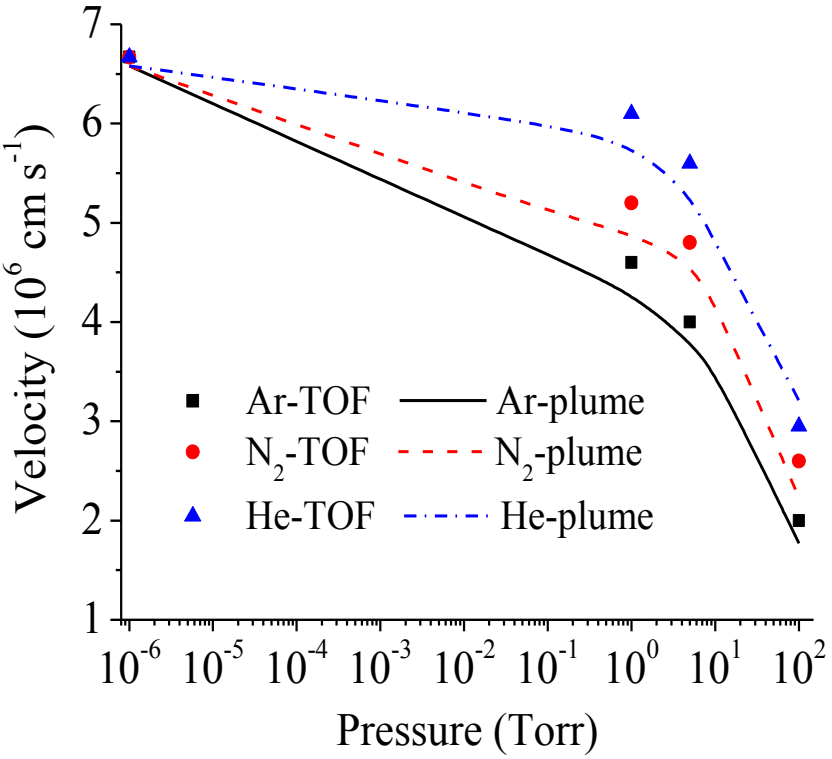

***Figure (5-10)**: Comparison between the expansion velocities of the plasma plume derived from iCCD images and TOF measurements as a function of the pressure for helium, nitrogen and argon.*

5.4 Conclusion

In this chapter, we studied an aluminum plasma plume induced by nanosecond excimer laser at 308 nm. The plasma plume was characterized by two time- and space- resolved techniques, namely spectrally-integrated iCCD imaging and Time-Of-Flight of aluminum ions as a function of the ambient gas composition and pressure.

On the one hand, the iCCD images of the plasma show that the plume dimension depends on the gas environment and on the interval time when the plasma is photographed. Indeed, from plasma ignition up to ~200 ns and for pressures lower than ~20 Torr, the plasma plume has a sphere-like shape. This isotropic expansion is mainly attributed to the homogeneous heating of the plume by the energetic species. Beyond 200 ns, the plasma plume axially expands due to the diffusion of electrons across the focal spot boundary. This is true whatever the ambient gas composition. When the pressure of the ambient gas is higher than ~20 Torr, the axial expansion rate of the plasma plume becomes dependent of the gas composition so that the plasma plume length is shorter when the gas species mass is higher. The thermal conductivity is assumed to also play a role in this expansion. Indeed, the gas with the highest thermal conductivity (helium) leads to the longer plasma plume length.

On the other hand, the TOF measurements of the aluminum ions also show a dependence on the gas environment. At low pressure and near the target surface (< 8 mm), the velocity of Al ions can be estimated to be $\sim 5\times10^{6}$ cm s^{-1}. At higher pressure, it becomes dependent on the ambient gas composition. Far away from the target surface (> 8 mm), the Al ions velocity is strongly reduced and is higher when the gas mass species is lighter.

Finally, we have observed differences between the values of the expansion velocity deduced from iCCD images and TOF. They are attributed to the different physics underlying the two diagnostic techniques.

5.5 References:

[1] R. Kelly, J. Chem. Phys., **92**(8) 5047–5056, 1990.

[2] N. Ahmad and M.H. Key, Appl. Phys. B, **5**, 866, 1972.

[3] J. Dawson, P. Kaw and B. Green, Phys. Fluids, **12**, 875, 1969.

[4] R.K. Singh and J. Narayan, Phys. Rev. B, **41**, 8843, 1990.

[5] S.S. Harilal, B. O'Shay, Y. Tao and M.S. Tillack, Appl. Phys., **99**(8), 083303, 2006.

[6] H. Wang, A.P. Salzberg and B.R. Weiner, Appl. Phys. Lett., **59**(8), 935–937, 1991.

[7] A.K. Sharma and R.K. Thareja, Appl. Phys., **88**(12), 7334–7338, 2000.

[8] S. Bashir, N. Farid, K. Mahmood and M.S. Rafique, Appl. Phys. A, **107**(1), 203–212, 2012.

[9] N. Farid, S. Bashir and K. Mahmood, Physica Scripta, **85**(1), 015702, 2012.

[10] M.S. Dawood and J. Margot, AIP Advances, **4**, 037111, 2014.

[11] X. Tan, D. Zhang, X.A. Li, Z. Li and R. Fang, J. Phy. D Appl. Phys., **41**(3), 035210, 2008.

[12] Y. Kabouzi, M. D. Calzada, M. Moisan, K. C. Tran and C. Trassy, J. Appl. Phys., **91**(3), 1008–1019, 2002.

[13] W. Sdorra and K. Niemax, Mikrochim. Acta, **107**, 319, 1992.

[14] J.R. Ho, C.P. Grigoropoulos and J.A.C. Humphrey, Appl. Phys., **79**(9), 7205–7215, 1996.

[15] P.E. Dyer and J. Sidhu, J. Appl. Phys., **64**, 4657–4663, 1988.

[16] National Institute of Standards and Technology, available on line at: http://physics.nist.gov/PhysRefData/ASD/lines_form.html.

[17] G. Abdellatif, H. Imam and Y. Gamal, J. Korean Phys. Soc., 56(1), 300–308, 2010.

[18] S.S. Harilal, C.V. Bindhu, M.S. Tillack, F. Najmabadi and A.C. Gaeris, J. Phy. D Appl. Phys., **35**(22), 2935, 2002.

[19] Y. Iida, Spectrochim. Acta B, **45**, 1353, 1990.

[20] M. Capitelli, A. Casavola, G. Colonna and A. De Giacomo, Spectrochim. Acta B, **59** 271–289, 2004.

[21] C. Aragon, J. Bengoechea and J.A. Aguilera, Spectrochim. Acta B, **56**, 619 (2001).

[22] J.C.S. Kools, T.S. Baller, S.T. De Zwart and J. Dieleman, Appl. Phys., **71**,4547, 1992.

[23] X.T. Wang, B.Y. Man, G.T. Wang, Z. Zhao, B.Z. Xu, Y.Y. Xia, L.M. Mei and X.Y. Hu, Appl. Phys., **80**, 1783, 1996.

[24] A.K. Sharma and R.K. Thareja, J. Appl. surf. Sci., **234**(1-4), 68, 2005.

[25] P. Nica, P. Vizureanu, M. Agop, S. Gurlui, C. Focsa, N. Forna, P. D. Ioannou and Z. Borsos, Jpn. J. Appl. Phys., 48, 066001, 2009.

GENERAL CONCLUSION & FUTURE WORK

General conclusion

Throughout this study, aluminum plasmas induced by XeCl excimer laser were characterized by space- and time-resolved techniques. The gaseous environment of the plasma plume was the main parameter of which the influence on the plasma plume characteristics was investigated. In particular, we studied the effect of the ambient gas type and pressure on the plasma parameters, including electron density n_e, excitation temperature T_e and on the plume dynamics. In this context, n_e was determined from the Stark broadening of the Al ion line at λ = 281.6 nm, while T_e was deduced by the Boltzmann plot method. On the other hand, the plasma plume dynamics were studied using time-resolved imaging (iCCD) and Time-Of-Flight techniques.

Laser plasma ablation process is a multi-time scale problem. In this context, our results clearly showed two different regimes; one at the earlier time of the plasma initiation until 300 ns and the other from 300 ns to the end of plasma life time. Time-resolved emission of Al II and Al I was strongly affected by the plume confinement that differed with the nature of the ambient gas and its pressure. The line intensity droped more rapidly with rising pressure in lighter gases while both signal-to-noise ratio and emission intensity increased in the heavier gases. More specifically, the emission intensity was strongly enhanced in argon, which can be explained by the relatively low ionization potential of this gas and to its high mass density as compared to helium and nitrogen. Such a gas could therefore be favourable to LIBS applications that require a high emission intensity of analytes as well as high signal-to-noise ratios.

At the very beginning of plasma initiation, the electron density fell rapidly with time. For example, in argon at atmospheric pressure, n_e dropped from $5x10^{18}$ cm^{-3} to $9x10^{17}$ cm^{-3} in the first 300 ns after a laser shot. This drop was mainly due to the electron and ion recombination yielding neutral atoms. In addition, our observations showed that helium produced the fastest decay due to its highest thermal conductivity while argon yielded the

slowest. At the opposite, in vacuum, the time dependence of electron density was relatively slow, with only a factor of 4 between 50 ns and 10 μs. Furthermore, due to its strong confinement on plasma plume, n_e was the highest in Ar as compared to other gases. After 300 ns, the temporal profile of the electron density showed an exponentially decrease with time. The effect of gas composition played an important role after 200 ns where the ambient gas pressure exceeded the pressure inside the plume. For example, after 600 ns, the density decreased by about 50% when changing argon for helium.

The spatial profile of the electron density showed that in the existence of an ambient gas with high mass species (i.e. large confinement of the plasma), the electron density was a maximal ($n_e = 3\times10^{18}$ cm^{-3}) in the plasma plume center (at $z = 0$, $r = 0$) at atmospheric pressure. Moreover, by moving axially (perpendicular to the target) and radially (parallel to the target) to the edge of plasma plume, the electron density linearly decreased progressively due to the recombination processes. Furthermore, our results showed that the spatial variation of electron density was less significant at low pressure so that it can be considered as homogenous along the plume axis. This behavior was attributed to the plume confinement, electron-ion recombination and formation of nanoparticles and clusters.

A similar trend was observed for the temporal dependence of the excitation temperature, which relaxed rapidly over about 2 μs and then decreased slowly. At low pressure, our results showed a significant drop in the excitation temperature values, which was due to the rapid expansion of the plasma that the total plasma energy distributed over a larger volume. In all experimental conditions (either various delay times or different gas pressure), helium had the lowest temperature, while argon provided the highest. This can be attributed to the confinement of the plasma plume by argon gas species that exert a force on the plasma species leading to more collisions and heating in the plume compared to other gases.

Compared to the axial variation of electron density, a similar evolution of the temperature was observed along the axial direction. Overall, the temperature decreases quasi-linearly from the target surface and had a different thermal gradient with the time of delay. We noted also that the axial variation was significant and it linearly decreased along the plasma plume, when the ambient gas had low thermal conductivity (argon), where it became exponentially-like decrease, when the ambient gas had higher thermal conductivity (helium). However, there was no significant change of the temperature in the radial direction. The

different behavior observed along the axial and radial directions can be attributed to different plasma expansion and kinetics, in particular due to the presence of the target surface in the radial direction.

The plasma plume was also characterized by two time- and space- resolved techniques, namely spectrally-integrated iCCD imaging and Time-Of-Flight of aluminum ions as a function of the ambient gas composition and pressure. The iCCD images of the plasma showed that the plume dimension changes drastically with the gas environment and as a function of time. In addition, the plasma plume had a sphere-like shape in the time interval from plasma ignition up to ~200 ns and for pressures lower than ~20 Torr. This isotropic expansion was mainly due to the homogeneous heating of the plume by the energetic species. For all ambient gases, beyond 200 ns, due to electron diffusion along the focal spot boundary, the plasma plume axially expands. The gas composition played an important role on the plume axial expansion at pressure higher than ~20 Torr, as the plasma plume length was observed to be shorter, when the gas species mass is higher and exhibit a lower thermal conductivity. At low pressure, our results showed that gas of higher mass density like Ar exerted confinement to the plasma plume and condenses them in the form of nanomaterial. However, light mass density, such as He required a larger target to substrate distance or higher background pressure to deposit maximum thickness of the film compared to heavier gases.

Our study of the TOF measurements also showed a dependence on the gas environment. At low pressure and near the target surface (< 8 mm), the velocity of Al ions was about 5×10^{6} cm s^{-1}. At higher pressure, it depended on the ambient gas composition. Far away from the target surface (typically beyond 8 mm), the ion velocity was strongly reduced but remained higher when the gas mass species was lighter. Finally, we have observed differences between the values of the expansion velocity deduced from iCCD images and TOF. The expansion velocity obtained from the iCCD images has been always slightly lower than that deduced from the TOF measurements. This can be attributed to the different physics underlying the two diagnostic techniques. Indeed, TOF measurements mainly represent a signature of a specific population (ions), where iCCD images constitute some average over multiple populations of different characteristics.

Future work

In conclusion, to this Ph.D. thesis work, several avenues could be envisioned as a continuation of the results presented. Among them, let us mention the following:

- ***Ambient gas composition***

The interaction between the plasma plume and ambient gas should be more deeply studied in order to elucidate how the energy (electrons, ions, radiation…) is transferred to the atoms of the ambient gas. During this thesis, it has been observed that the gas mass species play a primordial role on the plume dynamics where the plume volume is inversely proportional to the mass gas species. For this purpose, the effect of mixtures between two gases with high (Xe, Kr…) and low (He, Ne…) mass species on the plume dynamics should be carried out. On the other hand, the ablation in reactive ambient gas (N_2, O_2…) could be investigated. It is possible to obtain new chemical components that either growth from the gas or the target.

- ***Laser beam properties***

The present study was voluntarily performed using only the ns excimer laser emitting at 308 nm. However, the effect of the laser parameters, such as pulse duration and wavelength, plays a primordial role in the ablation process as described in the published data. Indeed, the deposition of energy will be very different. Therefore, applying the same ambient conditions used in the present work, it is important to study deeply the effect of fs laser on plasma plume dynamics, properties and interactions with the ambient gas.

- ***Applications: synthesis of thin films and nanomaterials***

Other than the plasma diagnostics, it is strongly recommended to study the effect of the ambient gas on the ablated nanoparticles and clusters. The pressure in the plume is high at the first instants and its relaxation rate will depend a lot on the ambient gas pressure. Indeed, the

lifetime of ablated nanoparticles becomes different and the chance to synthesize new nanomaterial with novel properties is important. Another factor involved in this process is the chemical composition of the target and the ambient gas. For example, in the case of aluminum target and nitrogen gas, it is possible to synthesize nanoparticles of aluminum nitride (AlN). In precisely crystallographic phase, this material is piezoelectric (mechanical energy ↔ electrical energy) and can be applied in a large number of technological applications.

- ***Modelling***

Modelling the plasma can be also suggested to validate some assumptions. By referring to our experimental results, we suggest to model the plasma kinetic in different ambient gas in order to discriminate on the main physical processes. Another point to study is the effect of the target surface on the plasma kinetics. The main question, is there any dynamic sheath? In addition, how it can change the kinetic of plasma species.

APPENDIX

Appendix I

Temporal evolution of n_e and T_e at different gas pressure and compositions.

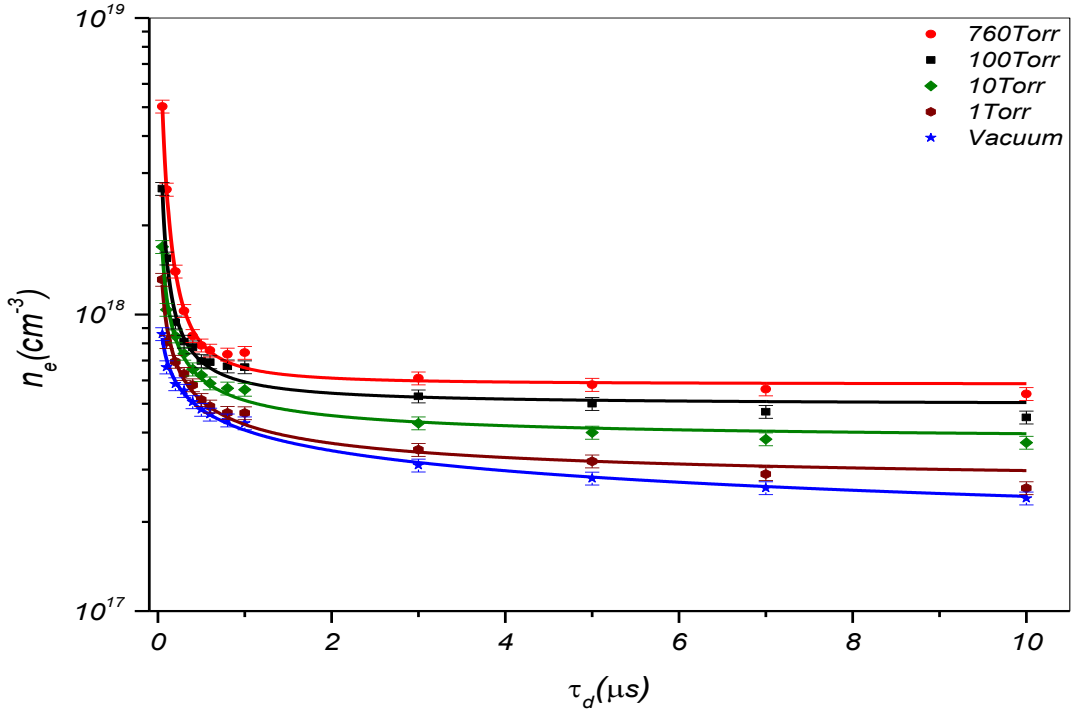

***Figure (A-1)**: Time dependence of n_e for various N_2 pressures. Refer to Page 70.*

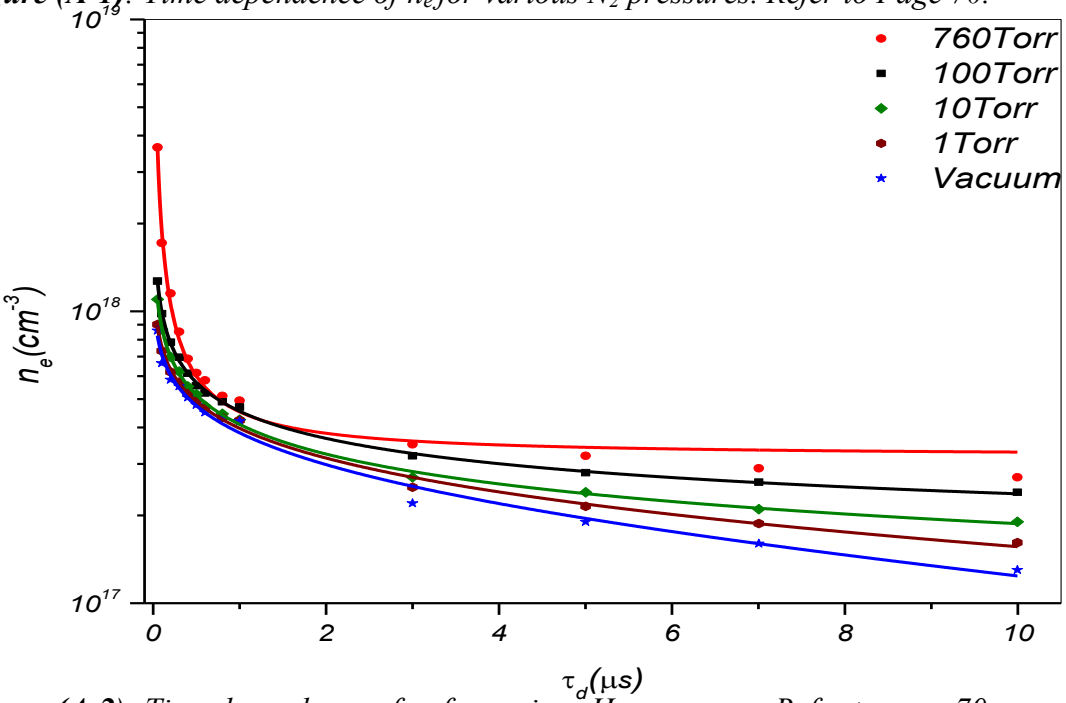

***Figure (A-2)**: Time dependence of n_e for various He pressures. Refer to page 70.*

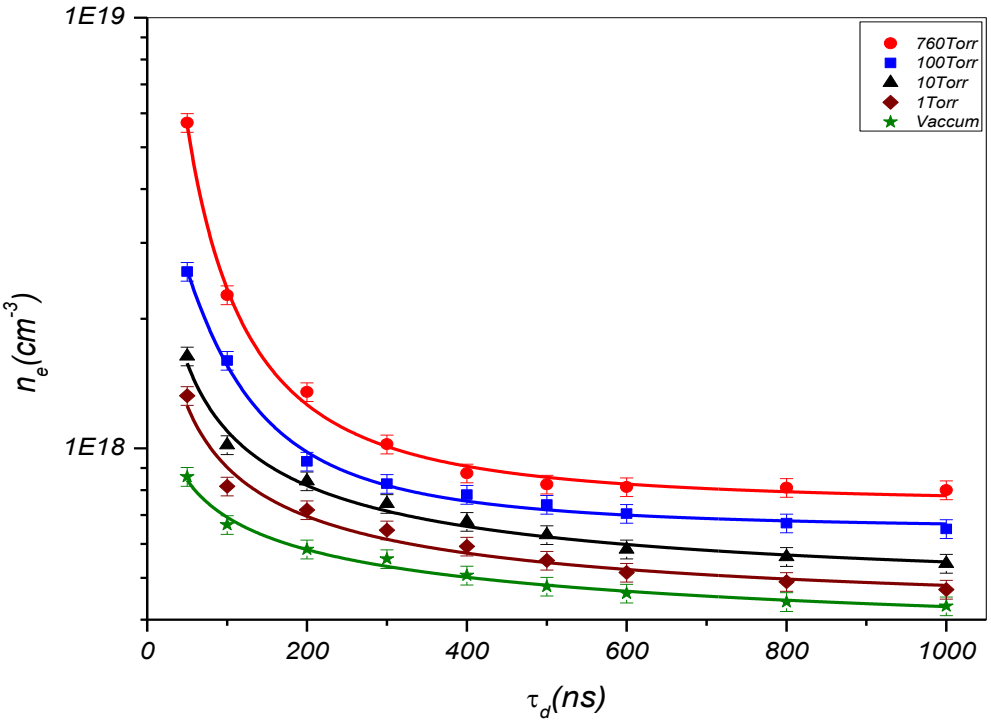

***Figure (A-3)**: Time dependence of n_e for various Ar pressures from AlII (281.6 nm).Refer to page 70.*

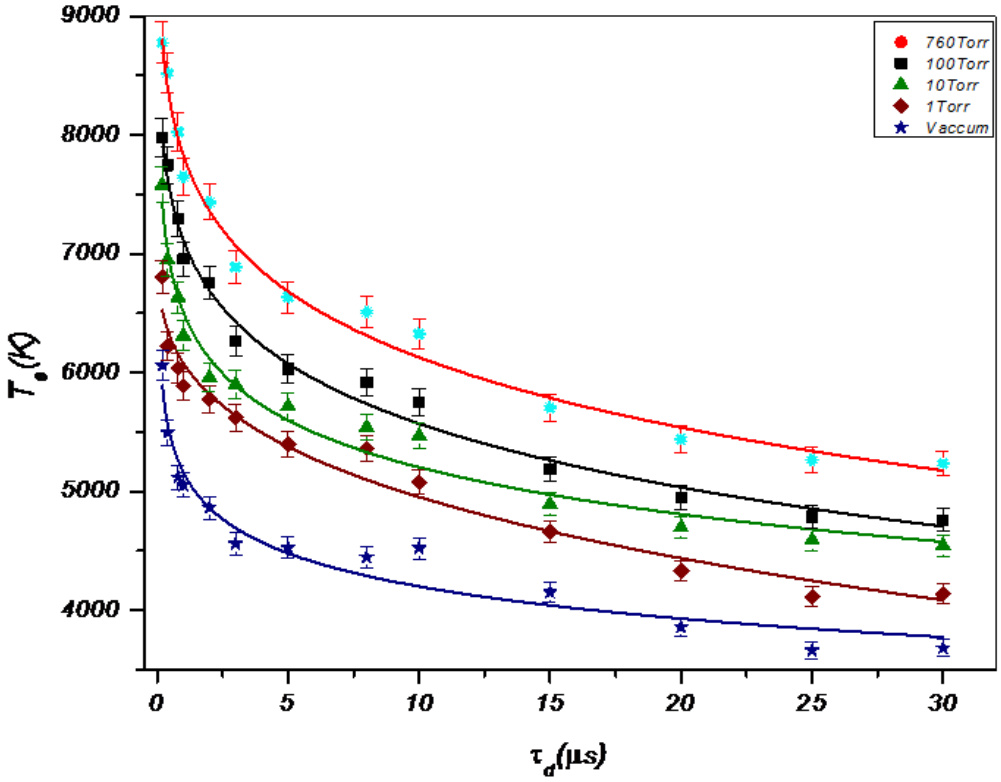

***Figure (A-4)**: Time dependence of T_e for different gas pressure in N_2 atmosphere. Refer to page 75.*

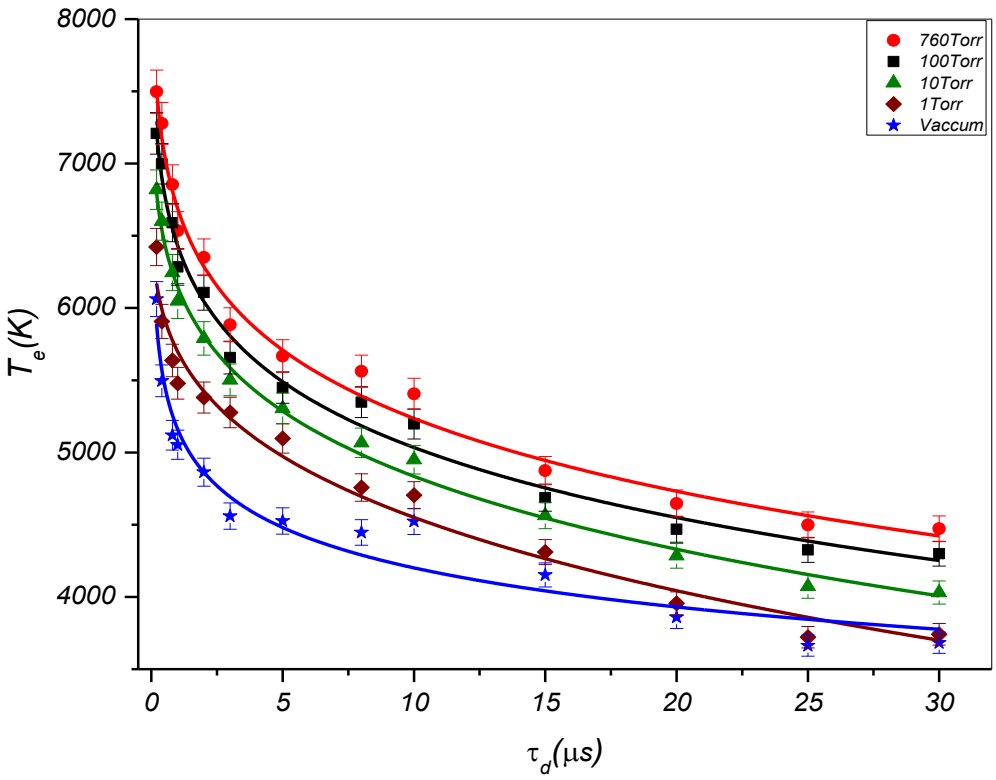

***Figure (A-5)**: Time dependence of T_e for different gas pressure in He atmosphere. Refer to page 75.*

Table (A-1): Physical properties of the gases.

	Molecular weight	Density	Ionization potential	Thermal conductivity	Specific heat
		Kg m^{-3}	eV	$W \cdot m^{-1} \cdot K^{-1}$	kJ K^{-1} kg^{-1}
Argon	39.948	1.784	15.759	17.72×10−3	0.312
Nitrogen	14.007	1.251	14.534	25.83×10^{-3}	0.718
Helium	4.03	0.178	24.587	0.1513	3.12

Table (A-2): Physical properties of the aluminum target.

T_b (K)	T_f (K)	ρ ($kg\ m^{-3}$)	L_v ($J\ g^{-1}$)	L_f ($J\ g^{-1}$)	C_p ($J\ K^{-1}\ kg^{-1}$)	k ($W\ m^{-1}\ K^{-1}$)
2740	934	2700	10800	388	900	237

T_b, boiling point; T_f, melting point; ρ, density; L_v, latent heat of evaporation; L_f, latent heat of fusion; C_p, specific heat; k, thermal conductivity

Appendix II

Spatial evolution of n_e and T_e at different gas pressure and compositions.

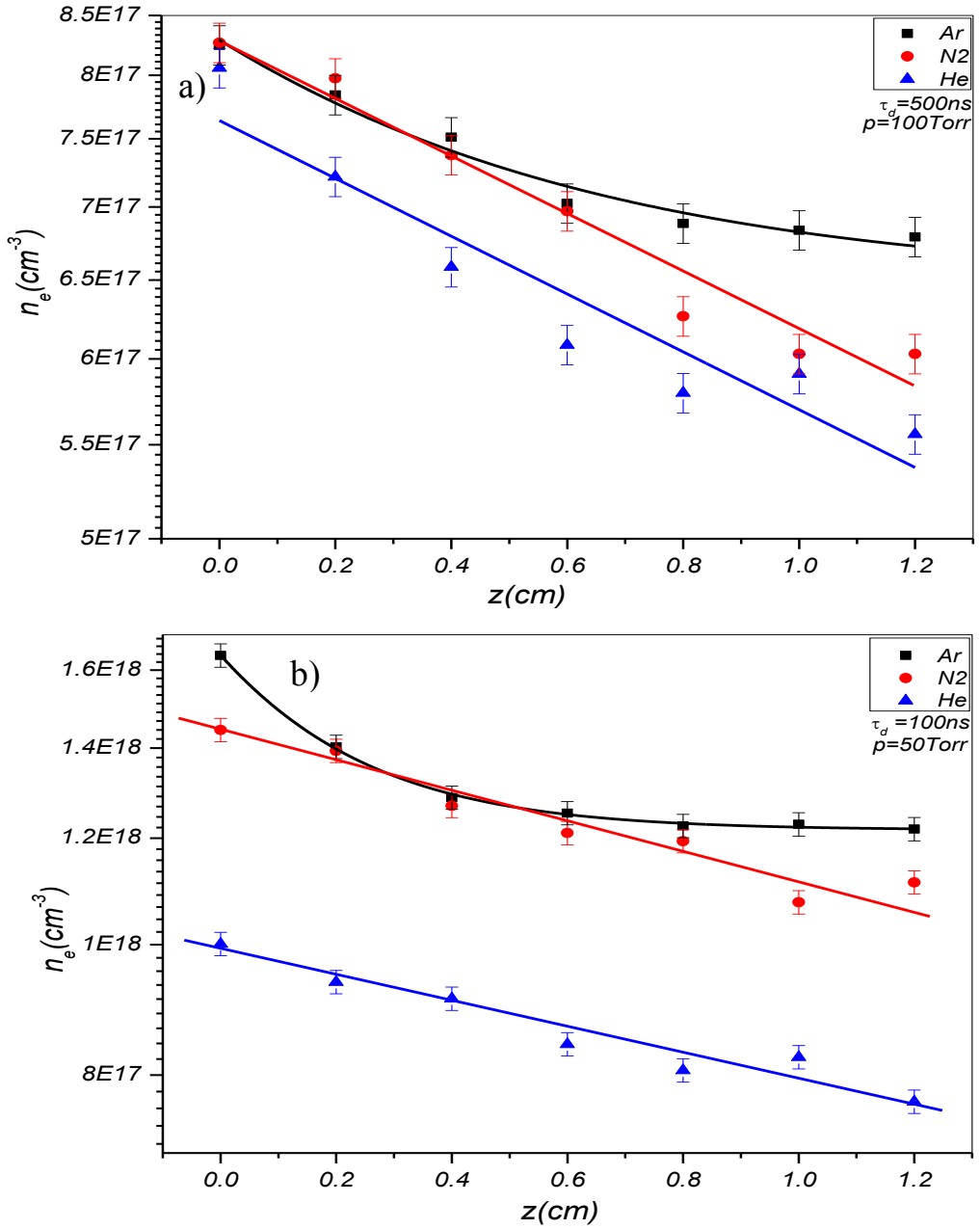

***Figure (A-6)**: Axial variation of n_e in Ar, N_2 and He ambient gases a) at pressure 10 Torr and time delay 500 ns. b) at pressure 50 Torr and time delay 100 ns.*

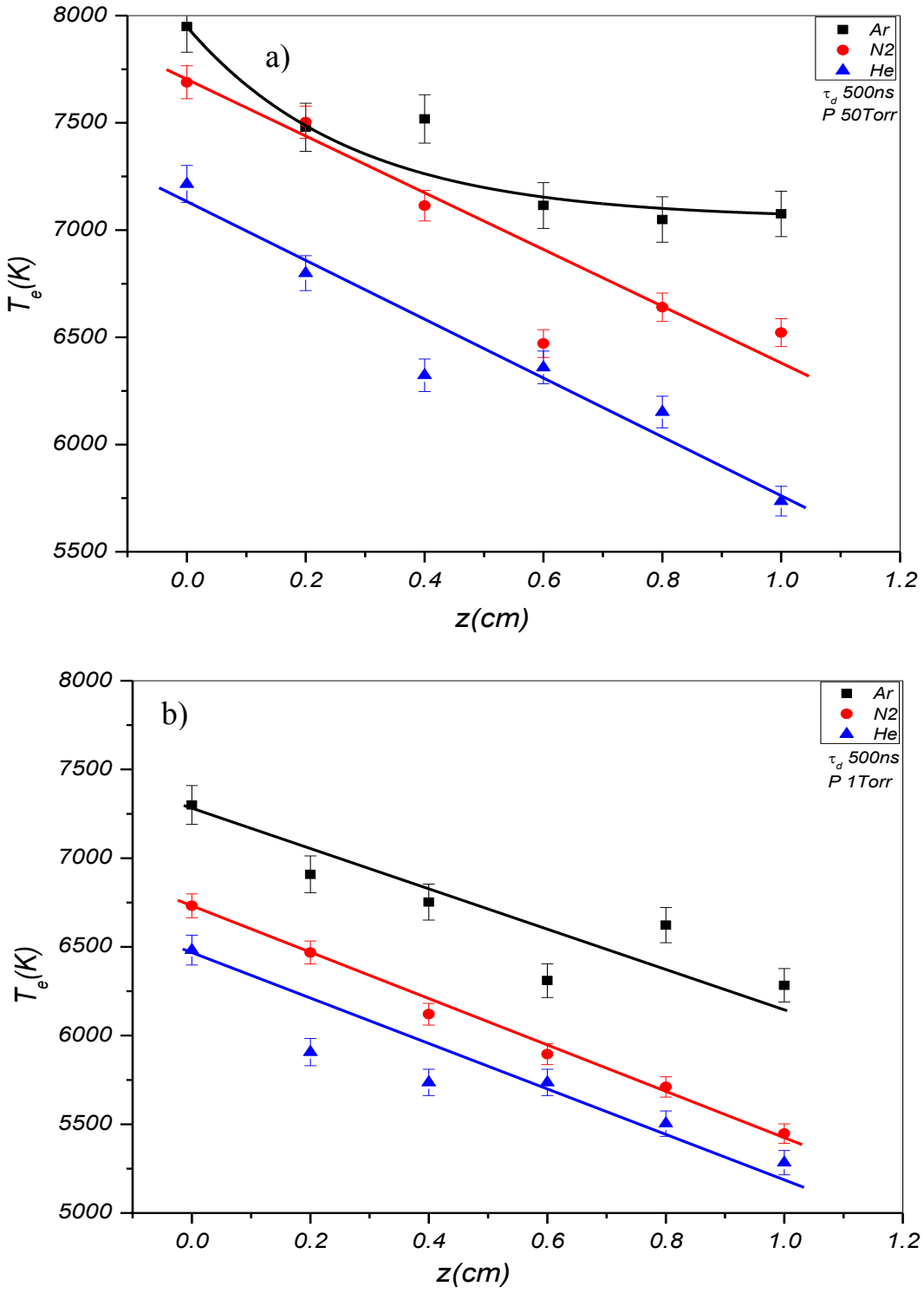

***Figure (A-7)**: Axial variation of T_e in Ar, N_2 and He ambient gases a) at pressure 50 Torr and time delay 500 ns. b) at pressure 1 Torr and time delay 500 ns.*

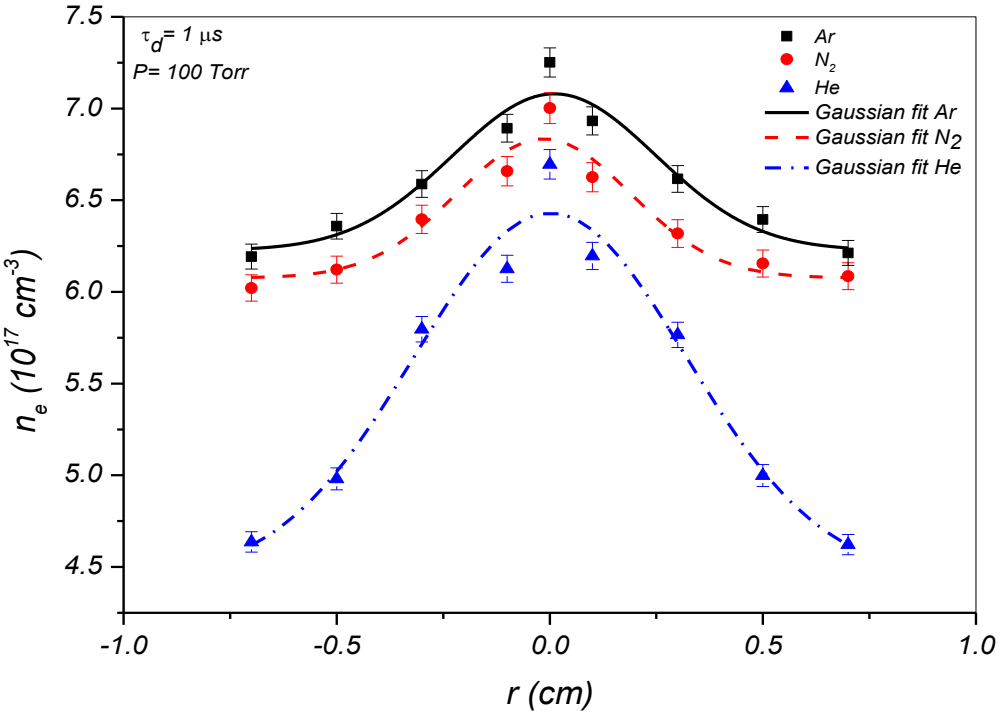

***Figure (A-8)**: Radial variation of n_e in Ar, N_2 and He ambient gases at pressure 100 Torr and time delay 1 μs.*

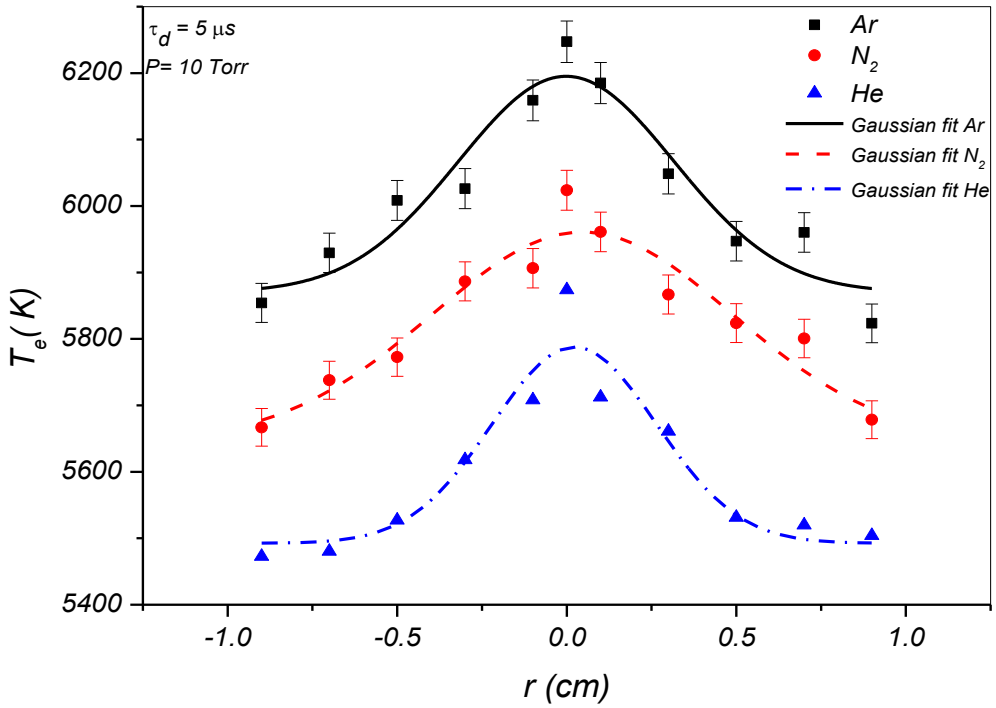

***Figure (A-9)**: Radial variation of T_e in Ar, N_2 and He ambient gases at pressure 10 Torr and time delay 5 μs.*

Appendix III

Temporal and ambient pressure effects on Aluminum plasma plume dynamics induced by an excimer laser in different ambient gases

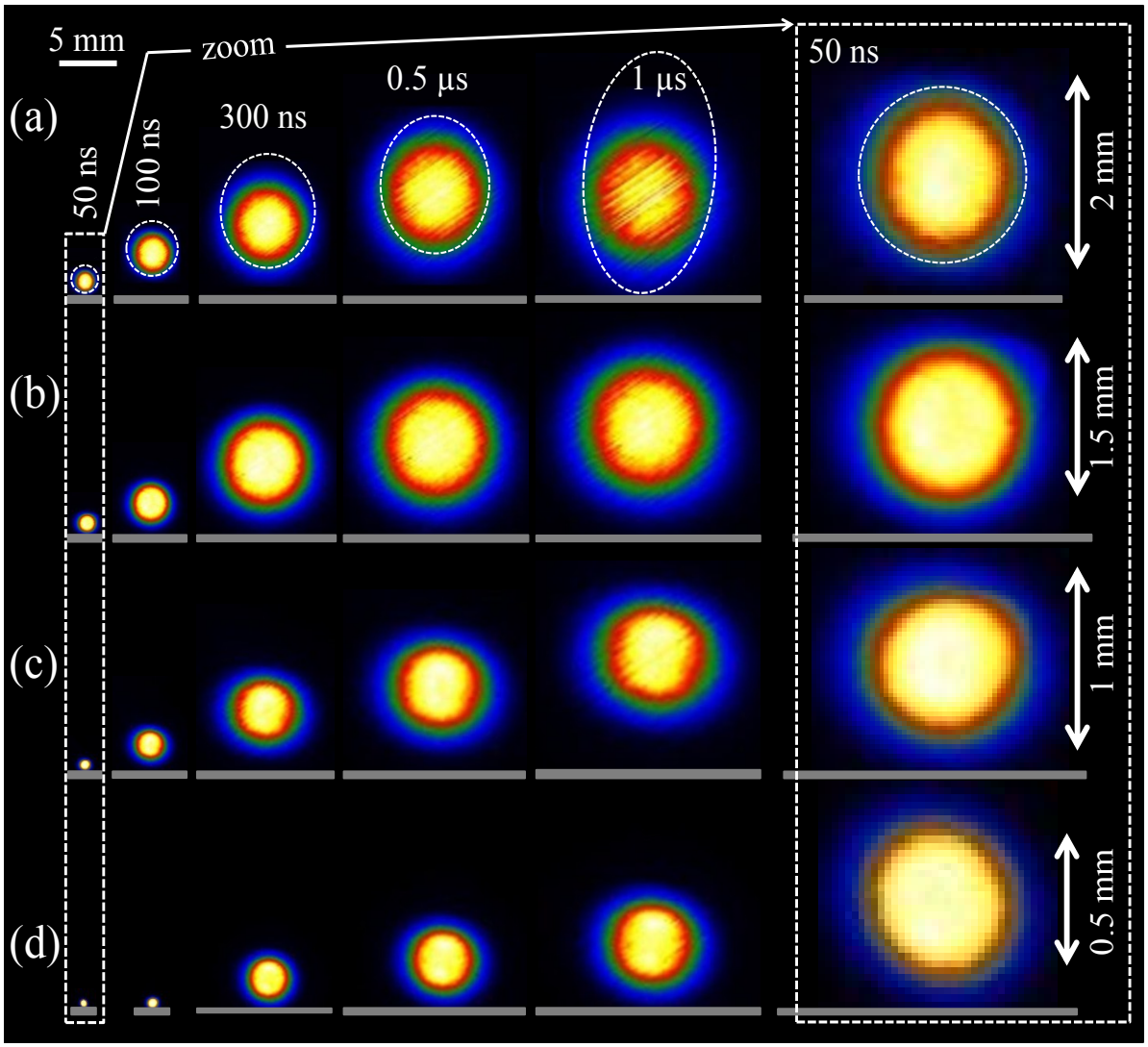

***Figure (A-10)**: iCCD images of the plasma plume in argon ambient gas at a) 0.1 Torr, b) 1 Torr, c) 10 Torr and d) 100 Torr. A zoom of the plasma plume at 50 ns is shown at right of the figure. The white-dashed contours correspond to the plasma plume shape obtained in vacuum.*

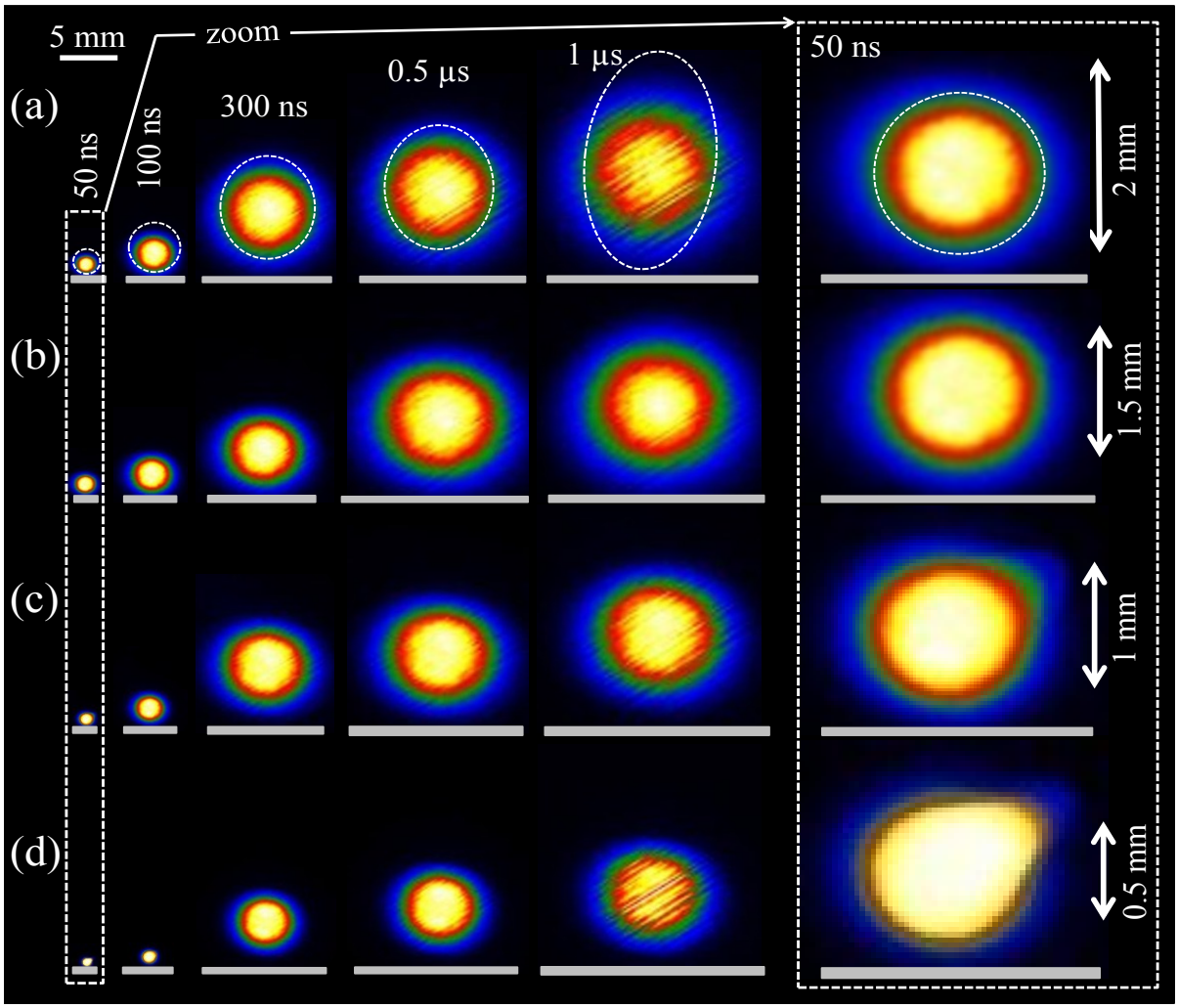

***Figure (A-11)**: iCCD images of the plasma plume in nitrogen ambient gas at a) 0.1 Torr, b) 1 Torr, c) 10 Torr and d) 100 Torr. A zoom of the plasma plume at 50 ns is shown at right of the figure. The white-dashed contours correspond to the plasma plume shape obtained in vacuum.*

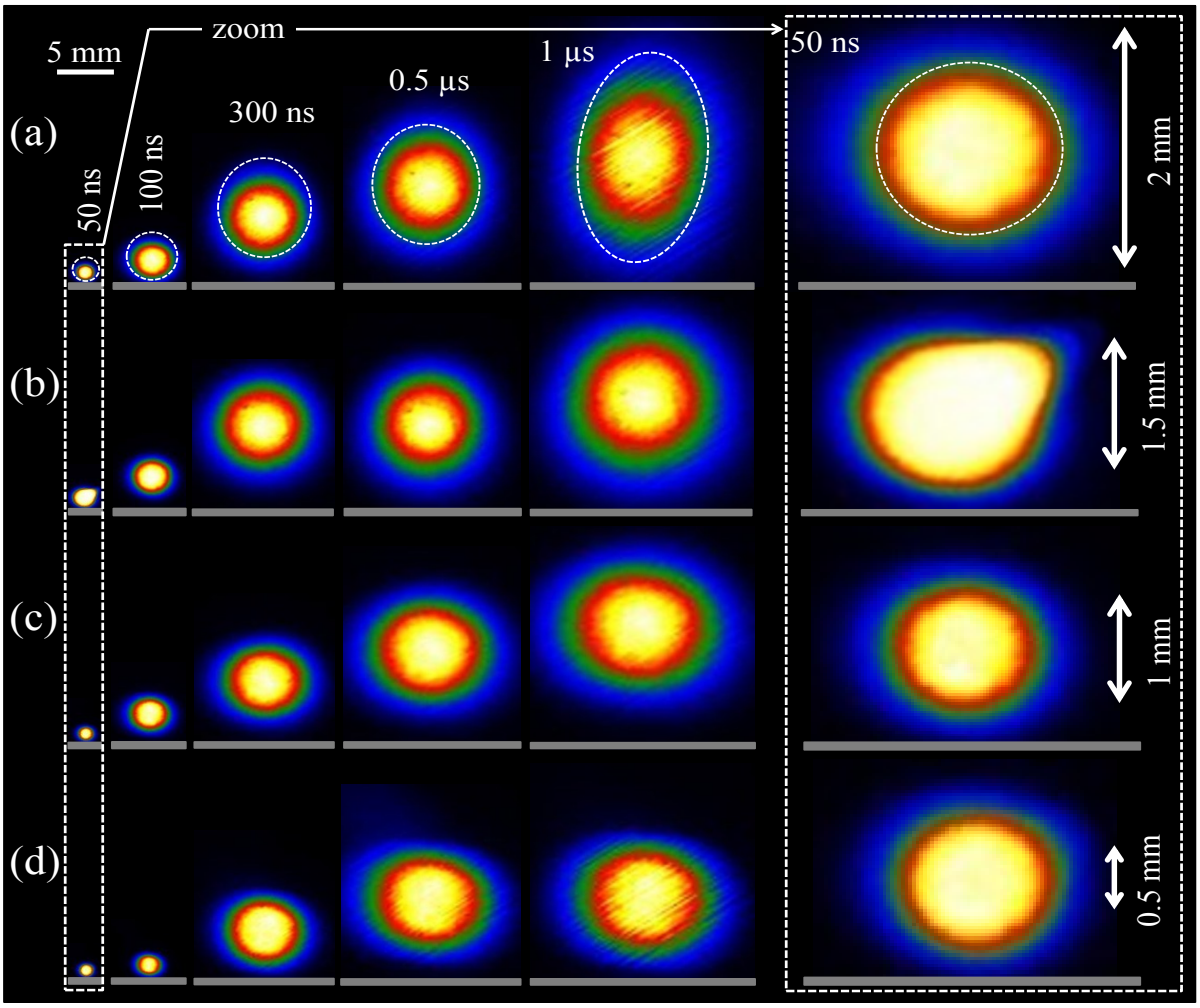

***Figure (A-12)**: iCCD images of the plasma plume in helium ambient gas at a) 0.1 Torr, b) 1 Torr, c) 10 Torr and d) 100 Torr. A zoom of the plasma plume at 50 ns is shown at right of the figure. The white-dashed contours correspond to the plasma plume shape obtained in vacuum.*

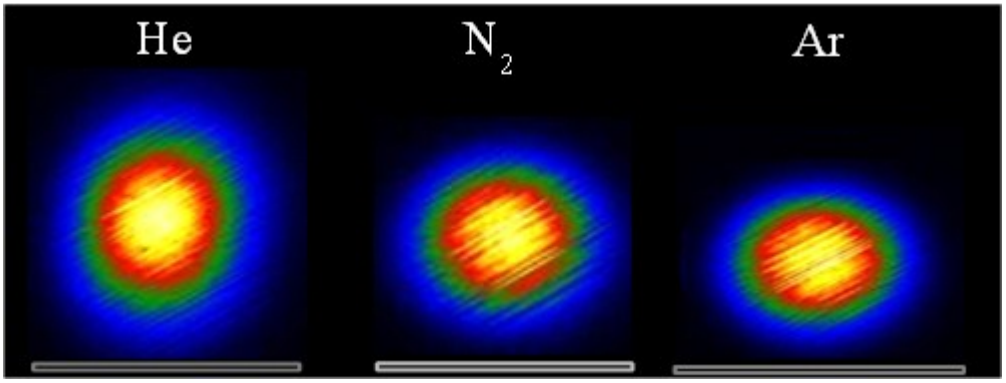

***Figure (A-13)**: Comparison between iCCD images of the plasma plume in helium, nitrogen and argon at 0.1 Torr after 1µs from laser pulse.*

Appendix IV: *Author contributions*

At the end of this thesis, I would like to clarify my scientific contributions for each article included.

Article 1

Effect of ambient gas pressure and nature on the temporal evaluation of aluminum laser induced plasmas.

M.S. Dawood and *J. Margot*, AIP Advances 4, 037111 (2014).

My contribution to this article is the development of diagnostics to determine the temporal behavior of plasma spectra, electron density and temperature in different ambient atmospheres. In addition, I performed the experimental measurements, analyzed the results and wrote the first version of the article.

Article 2

Axial- and radial- resolved electron density and excitation temperature of aluminum plasma induced by nanosecond laser: effect of the ambient gas composition and pressure.

Mahmoud S. Dawood, Ahmad Hamdan and Joelle Margot, submitted to Journal of Physics B: Atomic, Molecular and Optical Physics (2015).

My contribution to this article deals with the improvement of plasma diagnostics to determine the spatial behavior (axial and radial directions) of plasma spectra, electron density and temperature in different ambient atmosphere. Moreover, I carried out the experimental measurements, analyzed the results and wrote the first version of the article.

Article 3

Influence of gas, composition and pressure on the plasma plume dynamics of nanosecond laser-induced aluminum plasmas

Mahmoud S. Dawood, Ahmad Hamdan and Joelle Margot, submitted to Journal of Physics B: Atomic, Molecular and Optical Physics (2015).

My contribution to this article deals with the imaging of the plasma plume dynamics and with calculating the ionization front velocity in both space and time within different ambient atmospheres. Furthermore, I have compared the plume expansion velocity deduced from iCCD images and from TOF measurements and I wrote the first version of the article.